Basal Dynamics and Internal Structure of Ice Sheets

Michael J. Wolovick

Submitted in partial fulfillment of the
requirements for the degree of
Doctor of Philosophy
in the Graduate School of Arts and Sciences

Columbia University

2016

Abstract

Basal Dynamics and Internal Structure of Ice Sheets
Michael J. Wolovick

The internal structure of ice sheets reflects the history of flow and deformation experienced by the ice mass. Flow and deformation are controlled by processes occurring within the ice mass and at its boundaries, including surface accumulation or ablation, ice rheology, basal topography, basal sliding, and basal melting or freezing. The internal structure and basal environment of ice sheets is studied with ice-penetrating radar. Recently, radar observations in Greenland and Antarctica have imaged large englacial structures rising from near the bed that deform the overlying stratigraphy into anticlines, synclines, and overturned folds. The mechanisms that may produce these structures include basal freeze-on, travelling slippery patches at the ice base, and rheological contrasts within the ice column. In this thesis, I explore the setting and mechanisms that produce large basal stratigraphic structures inside ice sheets. First, I use radar data to map subglacial hydrologic networks that deliver meltwater uphill towards freeze-on structures in East Antarctica. Next, I use a thermomechanical flowline model to demonstrate that trains of alternating slippery and sticky patches can form underneath ice sheets and travel downstream over time. The disturbances to the ice flow field produced by these travelling patches produce stratigraphic folds resembling the observations. I then examine the overturned folds produced by a single travelling sticky patch using a kinematic flowline model. This model is used to interpret stratigraphic measurements in terms of the dynamic properties of basal slip. Finally, I use a simple local one-dimensional model to estimate the thickness of basal freeze-on that can be produced based on the supply of available meltwater, the thermal boundary conditions, ice sheet geometry, and the ice flow regime.

Contents

List of Figures

List of Tables

Acknowledgements

I thank my committee, Robin Bell, Roger Buck, and Tim Creyts, without whom this work would never have been completed. You were patient when I thought I knew everything and reassuring when I thought I knew nothing.

I thank the past and present members of the Polar Geophysics Group at Lamont. You provided me with a sense of common purpose, social interaction to break up the long hours in front of my computer, and cake.

I thank the other graduate students at Lamont. You provided me with camaraderie, good beer on Friday afternoons, and three excellent field trips.

I thank my parents, David Wolovick and Lisa Fischel-Wolovick, my grandparents, Maxine and Daniel Fischel, and the rest of my family. You were always supportive and always curious about my work, even if I wasn't always so good at explaining it.

I thank my old friends, Cid, Daniel, and Eric. You dragged me out of my shell when I needed it the most.

The first four years of my studies were supported by NSF award ANT-0632292. The last two and a half years were supported by NASA Earth and Space Science Fellowship 13-EARTH13F-246.

Chapter 1

Introduction

1.1 Motivation

Continental ice sheets are Earth's largest reservoir of fresh water. Greenland and Antarctica contain the equivalent of 7 and 58 meters of eustatic sea level rise, respectively (*Bamber et al.*, 2013a; *Fretwell et al.*, 2013). The former Laurentide, Cordilleran, and Fennoscandian ice sheets contained well over 100 meters (*Peltier*, 2004). The transfer of water between the solid ice sheets and the liquid ocean is governed by the mass balance of the ice sheets (*Cuffey and Paterson*, 2010). Ice sheets gain mass by the deposition of snow on their upper surfaces. They lose mass by surface melting at low elevations around their margins and by calving of icebergs into the sea. Internally, ice sheets exist in a state of constant motion, transporting material downhill from regions of net gain to regions of net loss (Figure 1.1). The dynamic flow of ice plays a crucial role in regulating the mass balance of ice sheets as a whole.

Fast ice flow is usually caused by slip over the bed and deformation of subglacial sediment (*Alley et al.*, 1986; *Bentley*, 1987; *Kamb*, 1987; *Engelhardt et al.*, 1990; *Cuffey and Paterson*, 2010). Ice sheet beds exert a strong control on both the dynamics and the thermodynamics of the overlying ice sheet (*Waddington*, 1987). The distribution and pressure of liquid water at the ice-bed interface control the rate of sliding and the drag that resists flow (*Clarke*, 2005; *Stokes et al.*, 2007). Subglacial water is generated by both surface and basal melting, and migrates under the influence of gravity and pressure (*Rothlisberger and Lang*, 1987). Water may accumulate in subglacial lakes (*Oswald and Robin*, 1973), may be removed from the system by basal freezing (*Bell et al.*, 2002; *Joughin et al.*, 2004a; *Christoffersen et al.*, 2010), or may be transported to the ice sheet margin where it emerges as proglacial or grounding line discharge (*Fricker et al.*, 2007; *Chu et al.*, 2009; *Le Brocq et al.*, 2009; *Smith et al.*, 2015). Subglacial water discharged at the grounding line generates buoyant turbulent plumes beneath ice shelves and at calving fronts that encourage heat transfer and melting (*Jenkins*, 2011). Subglacial melt and hydrologic processes are intimately connected with the erosion, transport, and entrainment of subglacial sediments and thus play a key role in the generation of the geomorphic signatures left behind by retreating ice sheets (*Hallet*, 1979, 1996; *Cohen et al.*, 2006; *Rempel*, 2008; *Clark*, 2010; *Christoffersen et al.*, 2010; *Creyts et al.*, 2013). My thesis focuses on the effect these subglacial processes have on the internal structure of ice sheets through melting, freezing, and variations in sliding.

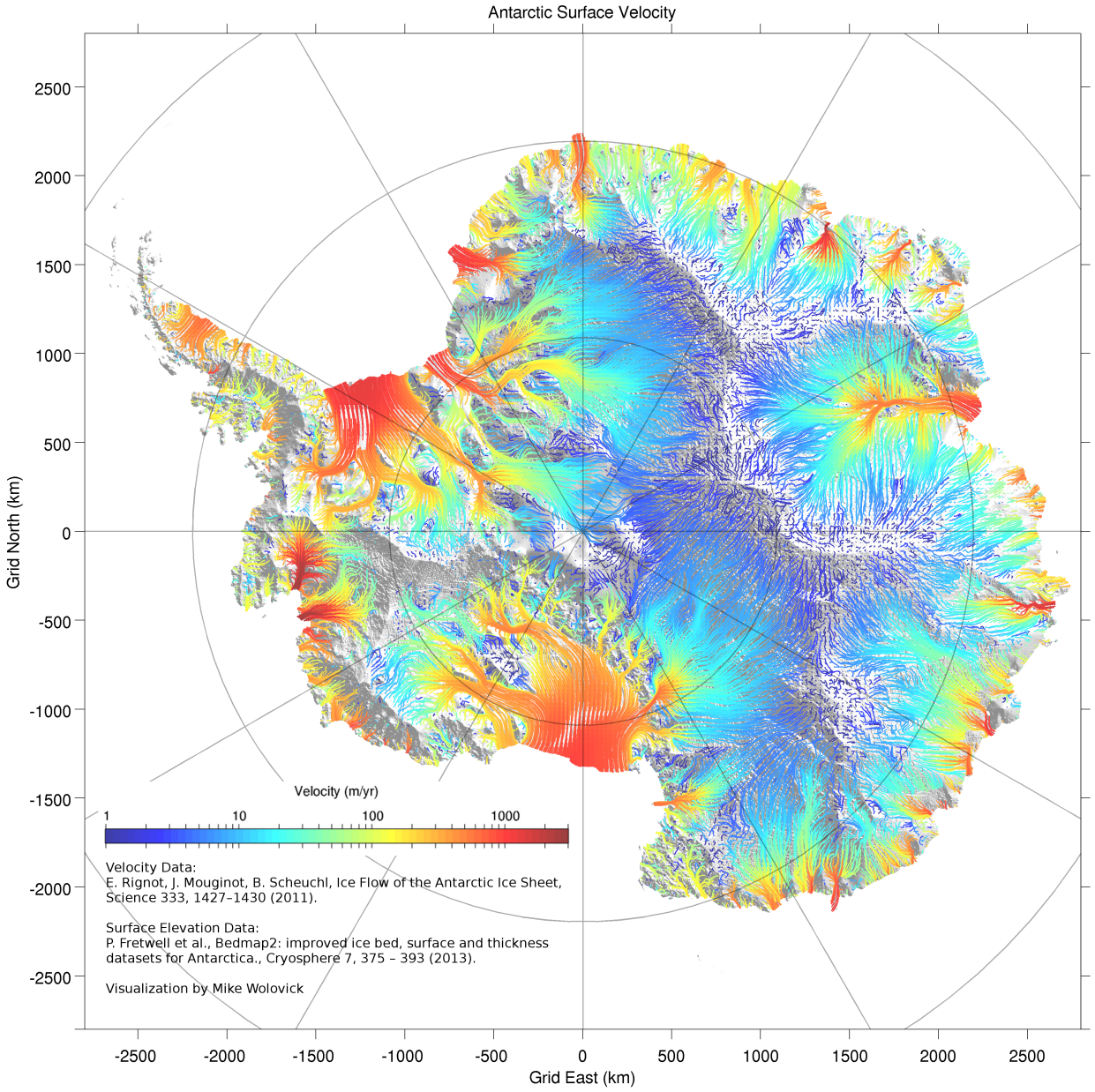

Figure 1.1: Antarctic surface velocity visualized as flow trajectories. Each line is 200 km long and colored by the average velocity magnitude along the trajectory. Trajectories are overlain on hillshaded surface elevation. Velocity data taken from *Rignot et al.* (2011) and surface elevation data taken from *Fretwell et al.* (2013). A high resolution (3856x3840) version of the visualization is available by request.

In particular, most of my thesis is centered around explaining the observation of large basal structures in ice-penetrating radar data from Antarctica (*Bell et al.*, 2011) and Greenland (*Bell et al.*, 2014; *MacGregor et al.*, 2015a). These folds are in the range of 5-20 km wide in the cross-flow direction, several 10's of km long in the along-flow direction, and can be up to a kilometer high (*Bell et al.*, 2011, 2014). The basal structures deform the surrounding stratigraphy into anticlines, synclines, and overturned folds. The recognition of the basal structures began when we analysed radar data collected during the Antarctica's Gamburtsev

Province (AGAP) survey in East Antarctica (*Bell et al.*, 2011). Our understanding of the basal structures expanded when we observed similar features in NASA's Operation IceBridge (OIB) data from Greenland (*Bell et al.*, 2014). Older radar data from Greenland also imaged these structures, but at the time they were misinterpreted as off-axis hills (*Legarsky et al.*, 1998). These structures reflect processes occurring either at or near the ice sheet bed. The three main explanations that have been put forward for these structures are basal freeze-on (*Bell et al.*, 2011), travelling slippery patches at the ice sheet base (*Wolovick et al.*, 2014)[1], and rheological contrasts within the ice column (*NEEM Community Members*, 2013). This thesis presents a detailed theoretical analysis of the stratigraphic structures that can be produced by travelling slippery patches, travelling sticky patches, and basal freeze-on, in addition to a detailed mapping of the water networks associated with the observed structures in East Antarctica.

1.2 History

In this section, I review some of the literature relevant to my thesis. First, I review the literature on ice-penetrating radar, with a special focus on subglacial water and internal layers. Next, I discuss some of the literature on basal sliding, followed by basal hydrology, and finally I give a brief overview of ice flow modelling.

1.2.1 Ice-Penetrating Radar

Ice-penetrating radar, also known as radio-echo sounding, uses measurements of reflected radio energy to generate an image of the subsurface structure of ice sheets. Deep ice radars generally transmit in the range of one megahertz to several hundred megahertz and may be mounted on either airborne or ground-based platforms (*Gogineni et al.*, 1998). Ice-penetrating radar is used to image the internal structure and basal topography of ice sheets (Figure 1.2). In rare cases, reflections from below the ice base have been imaged as well (e.g. *Gorman and Siegert*, 1999).

The basal reflection has generally received the most attention in ice-penetrating radar studies. The most important measurement derived from the basal return, ice thickness, has been made since the 1960's (e.g. *Bailey et al.*, 1964; *Evans and Robin*, 1966). Radar measurements of ice thickness are absolutely essential to our knowledge of the subglacial topography of Greenland and Antarctica (*Jankowski and Drewry*, 1981; *Shabtaie et al.*, 1987; *Hodge et al.*, 1990; *Letreguilly et al.*, 1991; *Lythe and Vaughan*, 2001; *Bamber et al.*, 2001, 2013a,b; *Fretwell et al.*, 2013; *Morlighem et al.*, 2014).

[1] Chapter 3.

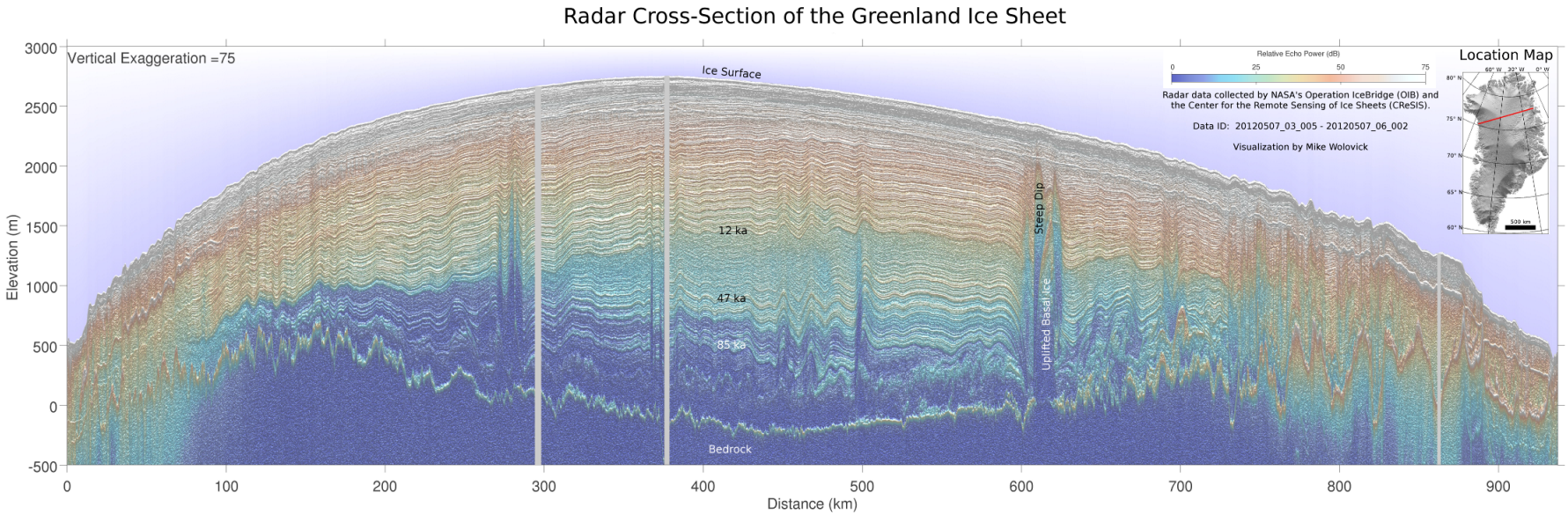

Figure 1.2: Radar cross-section of the Greenland Ice Sheet. The visualization emphasizes layered structure in the ice sheet. The radar data are displayed as though they are hillshaded topography illuminated from the top of the page. Several time horizons are labelled, as is a prominent large basal structure. Data come from Operation IceBridge (*Li et al.*, 2013). A high resolution (9000x3051) version of the visualization is available by request.

Other characteristics of the basal return have been used to make inferences about the presence of water at the ice sheet bed. The brightness, morphology, and specularity of the basal return have been used to locate subglacial lakes since the 1970's (*Oswald and Robin*, 1973). Deep and wide subglacial lakes were easily identified in ice-penetrating radar data because they are hydraulically flat, highly reflective, and specular. Beginning in the 1990's, a wide literature developed around radar-detected Antarctic subglacial lakes. *Siegert et al.* (1996) made an inventory of known subglacial lakes and revised it multiple times in response to new discoveries (*Siegert et al.*, 2005; *Wright and Siegert*, 2012). Studies were made of the dimensions, setting, and depth of subglacial lakes (*Dowdeswell and Siegert*, 1999; *Gorman and Siegert*, 1999; *Dowdeswell and Siegert*, 2003). New surveys were conducted and new criteria for locating lakes were developed (*Carter et al.*, 2007). *Popov and Masolov* (2007) introduced lakes that were originally detected by Soviet Antarctic surveys during the 1980's into the English-language literature. Lake Vostok, by far the largest subglacial lake (*Kapitsa et al.*, 1996), was the subject of a dedicated geophysical survey mission (*Studinger et al.*, 2003).

During the 2000's, a new population of "active lakes" was discovered through satellite observations of surface elevation changes (*Gray et al.*, 2005; *Wingham et al.*, 2006; *Fricker et al.*, 2007; *Smith et al.*, 2009; *Fricker and Scambos*, 2009; *Fricker et al.*, 2010). However, radar observations at the locations of the active lakes often failed to detect the flat, bright, and smooth signature of a classic subglacial lake (*Langley et al.*, 2011; *Siegert et al.*, 2014). Nonetheless, the active lakes were located in hydrologic minima that should trap water (*Langley et al.*, 2011; *Siegert et al.*, 2014). This discrepancy raises the question of how radar might be used to locate subglacial water that is not ponded in a classic (deep and wide) lake.

Ice-penetrating radar has been used to identify subglacial water outside of the classic deep lake settings in a number of ways. The simplest is to correct bed-returned power for an assumed attenuation rate in order to identify highly reflective areas (*Oswald and Gogineni*, 2008; *Jacobel et al.*, 2010). This method generally produces a distribution of bed reflectivity that can be represented by two overlapping bell curves, one for the dry bed reflectivity distribution and one for the wet bed reflectivity distribution. The presence of two normal distributions is evidence that water exists in the survey area, but unambiguously identifying specific regions of the bed as wet or dry is difficult if they fall within the overlapping range. In addition, englacial attenuation can complicate interpretations of basal reflectivity (*Matsuoka*, 2011). More advanced phase-based analysis can be used to attribute basal reflectivity to specular and diffuse components in order to infer basal roughness (*Peters et al.*, 2005). Combined with reflectivity analysis, these methods permit a more sophisticated classification of the basal interface according to material and morphology. Specularity analysis can even be used to distinguish distributed cavities from concentrated channels in the subglacial water system, or to constrain the orientation of bedforms if survey design permits the mapping of anisotropy (*Schroeder et al.*, 2013).

In addition to the basal return, the englacial returns have been a valuable source of information on ice sheet processes and boundary conditions. Englacial reflections occur at dielectric contrasts within the ice caused by variations in density, conductive impurities, and crystal orientation fabric (*Clough*, 1977; *Millar*, 1981; *Matsuoka et al.*, 2004). Internal layers within the meteoric ice are generally assumed to represent isochrones, or sedimentary hori-

zons of constant age (*Clough*, 1977). Internal reflections also occur at the meteoric-accreted ice boundary (the boundary between ice derived from surface snowfall and ice derived from basal freeze-on) (*Bell et al.*, 2002; *MacGregor et al.*, 2009a). The lower portion of the ice column has historically been referred to as the "echo-free zone" because of the lack of internal reflections detected there (*Drewry and Meldrum*, 1978; *Drews et al.*, 2009). However, as radar technology has improved, an increasingly rich and stratigraphically complex environment has been revealed in the supposedly "echo-free" region near the bed (*Bell et al.*, 2011).

The isochronous assumption has allowed internal layers to be used to study ice flow, boundary conditions, and rheology. One of the most common uses of internal layers is to infer surface accumulation rates. Internal layers have been used to solve for surface accumulation rate in one-dimensional (*Fahnestock et al.*, 2001), two-dimensional (*Waddington et al.*, 2007; *MacGregor et al.*, 2009b; *Ng and King*, 2011), or three-dimensional (*Leysinger Vieli et al.*, 2011) models. Some models assume steady-state forcing (e.g. *Ng and King*, 2011), while others leverage the information contained in multiple layers to make inferences about temporal changes in accumulation (*MacGregor et al.*, 2009b; *Leysinger Vieli et al.*, 2011). *Vaughan et al.* (1999) used internal layers to identify a relationship between surface slope and accumulation, a relationship later reinforced with additional layer data (*Arcone et al.*, 2012a,b; *Das et al.*, 2013). Shallow layers have been used to constrain modern accumulation rates (*Richardson et al.*, 1997), and internal layers have been used to make simultaneous inferences about changing accumulation and ice dynamics over time (*Neumann et al.*, 2008).

Internal layers have often been used to make inferences about ice dynamics and basal conditions. One of the earliest uses of internal layer data was to demonstrate that the Greenland Ice Sheet near Camp Century was approximately in steady state over the last millennium (*Robin et al.*, 1969). Internal layers have been used to identify relict signatures of fast ice flow in slowly flowing areas, and thus to make inferences about changes in ice dynamics over time (*Ng and Conway*, 2004; *Bingham et al.*, 2015). Buried crevasses with overlying internal layers were used to constrain the timing of the shutdown of Ice Stream C (*Retzlaff and Bentley*, 1993). A change in flow direction upstream of Ice Stream C was inferred based on fast-flow signatures in internal layers (*Conway et al.*, 2002). Internal layers have also been used to constrain the long-term ice flow field over Lake Vostok (*Tikku et al.*, 2004). Internal layers can be used to probe the ice sheet bed, both in terms of basal melting (*Fahnestock et al.*, 2001; *Dahl-Jensen et al.*, 2003; *Catania et al.*, 2006, 2010) and basal traction (*Weertman*, 1976; *Christianson et al.*, 2013; *Keisling et al.*, 2014). Internal layers have been used to map the thickness and depth of climatic units within ice sheets (*Karlsson et al.*, 2013; *MacGregor et al.*, 2015a). The reflected energy from internal layers has been used to constrain ice attenuation rate and therefore temperature (*MacGregor et al.*, 2015b). One of the most powerful ice dynamic uses of internal layers results from the stiffening of deep ice underneath a dome, known as the "Raymond effect" (*Raymond*, 1983). The Raymond effect has allowed internal layers to be used to constrain ice rheology, past thickness variations, dome migration, and grounding line history (*Conway et al.*, 1999; *Vaughan et al.*, 1999; *Hindmarsh et al.*, 2011; *Gillet-Chaulet et al.*, 2011; *Kingslake et al.*, 2014).

Internal layers have even proved useful on other planets. Internal layers detected using orbiting radars have been used to test for past flow of the Martian polar ice caps (*Koutnik et al.*, 2009; *Karlsson et al.*, 2011). Martian internal layers have also been used to identify

large deposits of carbon dioxide ice containing the equivalent of 80% of the mass of the Martian atmosphere (*Phillips et al.*, 2011).

1.2.2 Basal Sliding

Theoretical descriptions of basal sliding can be broadly divided into two categories: hard bed models and soft bed models (*Clarke*, 2005). Hard bed models describe basal sliding as the result of three processes: regelation (melting on the upstream side of obstacles and freezing on the downstream side), viscous creep of the ice around obstacles, and the formation of water-filled cavities in the lee of obstacles (*Weertman*, 1957; *Lliboutry*, 1968; *Clarke*, 2005; *Fowler*, 2010). All of these processes strengthen as basal temperature approaches the melting point. Cavitation depends on subglacial water pressure. All of these processes also depend on bed roughness, a quantity that is generally unknown and that tends to evolve over time in response to bedrock erosion and sediment transport (*Fowler*, 2010). Regelation and creep take the form of power-law relationships between sliding velocity and basal drag (*Weertman*, 1957), a quality that makes them appealing to ice-sheet modelers in need of a simple basal boundary condition (*Cuffey and Paterson*, 2010). However, cavitation produces a multi-valued sliding law and can also lead to a Coulomb-plastic description of drag, in which basal stress is proportional to the pressure difference between ice and water, unrelated to sliding velocity (*Lliboutry*, 1968; *Iken*, 1981; *Schoof*, 2005). A Coulomb-plastic description is conceptually simple but quite difficult to implement in an ice sheet model. With a Coulomb-plastic boundary condition, basal sliding cannot be determined locally and must be solved for across the entire domain simultaneously (*Cuffey and Paterson*, 2010).

Coulomb-plastic behavior is also the most plausible model of soft-bed sliding (*Tulaczyk et al.*, 2000a,b). For a long time, there was a dispute in glaciology between those who considered subglacial till to have a Coulomb-plastic rheology (e.g. *Kamb*, 1991) and those who considered it to have a viscous or quasi-viscous rheology (e.g. *Boulton and Hindmarsh*, 1987). The chief evidence for quasi-viscous behavior is the observation of deformation distributed with depth within till sequences. Perfect Coulomb behavior should lead to the generation of a localized shear band at the ice-till interface (*Fowler*, 2010). However, the material heterogeneity that is often present within till sequences where distributed deformation is observed (e.g. *Boulton and Hindmarsh*, 1987, Figure 2), together with vertically propagating waves of water pressure (*Iverson*, 1998; *Tulaczyk et al.*, 2000a), may be sufficient to explain these observations. In addition, glaciological theories about till rheology must be consistent with the larger body of scientific knowledge about the behavior of granular materials, which are known to have yield stresses (*Kamb*, 1991; *Clarke*, 2005). Laboratory experiments on actual till samples support the Coulomb-plastic description of till rheology (*Kamb*, 1991; *Iverson*, 1998; *Tulaczyk et al.*, 2000a).

1.2.3 Basal Hydrology

Subglacial water is crucial to both the hard-bed and the soft-bed descriptions of basal sliding. Subglacial water flow is controlled by the hydraulic potential, or the sum of gravitational potential and pressure potential (*Shreve*, 1972). The pressure potential of subglacial water is typically defined as the sum of the overburden pressure of the ice sheet and the effective

pressure (effective pressure being the difference between ice overburden and actual water pressure) (*Shreve*, 1972; *Rothlisberger and Lang*, 1987). This formulation is useful because most sliding laws are sensitively dependent on effective pressure and because overburden pressure is typically an order of magnitude greater than effective pressure for large ice sheets when surface melt is not available to drive the creation of an efficient drainage system (*Iken*, 1981; *Engelhardt et al.*, 1990; *Schoof*, 2010; *Hewitt*, 2013; *Meierbachtol et al.*, 2013; *Andrews et al.*, 2014).

Subglacial water can have a variety of forms in addition to the deep subglacial lakes discussed above. Large (meter-scale) subglacial pipes with roughly circular or semi-circular cross-sections are commonly observed discharging water at the toe of alpine glaciers during the summer melt season (*Rothlisberger and Lang*, 1987; *Cuffey and Paterson*, 2010). These channels are controlled by the balance between inwards creep closure driven by the ice overburden pressure and outwards melting of the ice walls driven by viscous dissipation within the flowing water (*Rothlisberger*, 1972; *Shreve*, 1972; *Nye*, 1976). Channelized water flow has the special property that the water pressure drops with increasing discharge, causing the water system to naturally coalesce into a system of tributaries feeding a central trunk (*Rothlisberger*, 1972; *Nye*, 1976). An efficient channelized drainage system is thus capable of transporting large volumes of water without flooding a large area of the bed, reducing sliding velocity (*Nye*, 1976; *Rothlisberger and Lang*, 1987). Channelized drainage systems adjust their capacity on timescales of days to weeks and are capable of both steady-state flow and outburst floods known as jokulhaups (*Nye*, 1976).

In contrast to concentrated channels, distributed subglacial cavities facilitate basal sliding (*Walder*, 1986; *Kamb*, 1987; *Schoof*, 2010). Distributed cavities, as discussed above, form in the lee of subglacial obstacles. Because distributed cavities cover a large fraction of the basal area, they greatly reduce basal drag and enhance basal sliding (*Cuffey and Paterson*, 2010). Distributed cavities are primarily opened by the formation of void space as ice slides over the lee of bedrock bumps (*Walder*, 1986), while channels are primarily opened by melting of the walls (*Nye*, 1976). There is a feedback in which faster sliding velocities promote the opening of cavities because the ice cannot flow quickly into the space behind the obstacles, and more cavities in turn promote faster sliding. This feedback is one of the mechanisms responsible for sudden glacier surges and gives rise to multi-valued sliding laws (*Kamb*, 1987; *Fowler*, 1987). A cavity system, unlike a channel system, has the property that increased flow rate tends to be associated with higher pressure, so that water tends to spread out rather than concentrate (*Walder*, 1986; *Kamb*, 1987; *Schoof*, 2010). Basal hydrologic systems can switch spontaneously between cavity and channel systems in response to variable melt input, producing simultaneous changes in basal drag and sliding velocity (*Schoof*, 2010).

Subglacial water can also exist in thin sheets at the ice-bed interface (*Weertman*, 1969; *Weertman and Birchfield*, 1983a,b; *Clarke*, 2005; *Creyts and Schoof*, 2009) or in the pore space of subglacial sediments (*Alley et al.*, 1986; *Blankenship et al.*, 1986; *Engelhardt et al.*, 1990; *Tulaczyk et al.*, 2000a; *Clarke*, 2005; *Christianson et al.*, 2014). Thin sheets cover small basal obstacles, partially lifting the ice off of its bed and concentrating drag at the remaining larger obstacles (*Creyts and Schoof*, 2009). Thin sheets are a logical extension of distributed cavities. Water-saturated subglacial sediments weaken the bed, facilitating basal sliding and reducing basal drag (*Alley et al.*, 1986). Water-saturated subglacial "swamps" are one of the forms of subglacial water described in radar observations in addition to classic

lakes (*Carter et al.*, 2007; *Langley et al.*, 2011; *Christianson et al.*, 2014).

1.2.4 Ice Flow Modeling

The fundamental equations used to determine the flow field in ice sheet models are the Stokes equations, which describe the conservation of mass and momentum in a continuous fluid moving by laminar flow (*Cuffey and Paterson*, 2010). The rheology of ice is typically described as a non-Newtonian fluid according to Glen's law (*Glen*, 1953). However, the Stokes equations are computationally intensive: in three dimensions, they have four unknowns and four equations per grid cell. The unknowns are the three components of velocity plus the pressure. The equations are the conservation of the three components of linear momentum plus the conservation of mass (*Gerya*, 2010). In the "Full Stokes" treatment, all of these unknowns, in every grid cell in the model, must be solved for simultaneously (*Gerya*, 2010). This simultaneous computation must be repeated in every timestep. As a result, glaciologists have long utilized a number of simplified approximations to the Stokes equations.

The oldest approximation is the Shallow Ice Approximation (SIA) (*Fowler and Larson*, 1978; *Hutter*, 1981). This approximation makes the simplifying assumption that, because the ice sheet is much thinner than it is wide, the only stress component that matters is vertical shear. Under this assumption, the flow equations for ice reduce to local 1D vertical integrations: shear stress is determined by integrating down from the surface, and then velocity is determined by integrating up from the bed. The vertical profile in every horizontal grid cell can be solved for independently, completely eliminating the necessity for a large coupled solution. SIA models produce accurate solutions where the ice is moving mostly by internal deformation (*MacAyeal*, 1989).

A complimentary approach to the SIA is the Shallow Shelf Approximation (SSA) (*MacAyeal*, 1989). This approximation also takes advantage of the fact that the ice sheet is much thinner than it is wide, but instead of considering local vertical flow columns, it only considers vertically averaged velocity and rheology. Under this approximation, the problem is still a system of coupled equations requiring a simultaneous solution of all grid cells, but the grid in question is only two-dimensional rather than three-dimensional. Longitudinal stresses and lateral shear are included in SSA models, but vertical shear is not. SSA models are valid where the ice flows rapidly via basal slip, such as ice streams and ice shelves (*MacAyeal*, 1989). Many ice sheet models use a hybrid approach between SIA and SSA flow equations, because SIA and SSA are valid in complementary regions of the ice sheet. In the hybrid approach, the velocity computed by the SSA model is either used as a sliding velocity for the SIA integration, or the two approximations are used in separate areas (*Bueler and Brown*, 2009; *Pollard and DeConto*, 2009; *Winkelmann et al.*, 2011).

The last approximation short of full Stokes is the "Higher Order" model (*Blatter*, 1995; *Pattyn*, 2002). In the higher order model, all three dimensional grid cells must still be solved for simultaneously, just as they are in full Stokes. However, two simplifying assumptions are made about the vertical dimension: it is assumed that hydrostatic pressure completely satisfies the vertical force balance, and vertical velocity is determined by mass balance after the horizontal velocity is computed. As a result, the number of unknowns per grid cell is reduced from four to two. Chapter 3 uses a higher order model in a two-dimensional flowline.

Flowline (or flowband) models are a convenient way to reduce a three dimensional problem into a two dimensional one (e.g. *Nye*, 1959; *Reeh*, 1988, 1989; *Dahl-Jensen*, 1989). Flowline models use a horizontal coordinate aligned in the flow direction in order to model a vertical plane through the ice sheet. The cross-flow dimension is either ignored or included via a variable flowband width derived from a known ice sheet geometry. Both Chapter 3 and Chapter 4 use a flowline model. Chapter 4 simplifies the problem further by using a kinematic flowline model.

Kinematic models derive the velocity field from mass conservation forced by surface and basal mass balance. The effects of momentum conservation, variable rheology, and variable basal slip are represented by varying distributions of ice flow with depth (*Waddington et al.*, 2007). Kinematic models, whether in flowband or 3D, are extremely common in ice stratigraphy modeling because they capture all of the major influences on layer geometry in a computationally efficient manner (*Waddington et al.*, 2001; *Jacobson and Waddington*, 2004, 2005; *Parrenin et al.*, 2006; *Parrenin and Hindmarsh*, 2007; *Waddington et al.*, 2007; *Leysinger Vieli et al.*, 2007; *Hindmarsh et al.*, 2009; *MacGregor et al.*, 2009b; *Leysinger Vieli et al.*, 2011).

As discussed above, stratigraphy models have been used in conjunction with stratigraphic data to infer flow, accumulation, melt, and rheology (Section 1.2.1). Stratigraphy models have been used to extend isotopic data away from core sites (*Clarke et al.*, 2005), and predict temperature and attenuation within the ice column (*MacGregor et al.*, 2012). Stratigraphy models have also been used in idealized domains to learn more about ice stratigraphy itself and clarify the relationships between stratigraphy and boundary conditions (*Waddington et al.*, 2001; *Jacobson and Waddington*, 2004, 2005; *Hindmarsh et al.*, 2006; *Parrenin et al.*, 2006; *Leysinger Vieli et al.*, 2007; *Parrenin and Hindmarsh*, 2007). All stratigraphy models are one of two basic types: either the model solves the age equation on a fixed Eulerian grid (e.g. *Clarke et al.*, 2005), or the model tracks the age of Lagrangian tracers that it advects through the velocity field (e.g. *Jacobson and Waddington*, 2005). Eulerian models have the advantage of being easily added to existing model grids, but the disadvantage that fine structure in the stratigraphic geometry and local folds tend to be smoothed out by the artificial diffusion inherent in numerical advection schemes (*Clarke et al.*, 2005). Lagrangian models have the advantage of representing fine structure and contorted folds without artificial diffusion, but the disadvantage of requiring a large amount of numerical "bookkeeping" in order to keep track of all the tracers. The stratigraphic models I used in Chapters 3 and 4 are both Lagrangian models in order to resolve the structure of overturned basal folds observed in the radar data.

1.3 Chapters

The overall flow of the chapters moves from freeze-on, to traveling patches, and back to freeze-on. The thesis begins with an observational look at the water networks supplying basal freeze-on in Chapter 2, then moves to the development of the traveling patches model as an alternate explanation for the observed basal structures in Chapters 3 and 4, and then returns to freeze-on from a simple modeling perspective in Chapter 5.

Chapter 2 identifies the water networks that feed freeze-on units in East Antarctica. The

networks are composed of numerous small subglacial lakes organized along bedrock valleys. Some of the networks terminate under the large basal units observed in radar (*Bell et al.*, 2011), suggesting water transport towards freezing regions. Chapter 2 was published in the Journal of Geophysical Research: Earth Surface in 2013 (*Wolovick et al.*, 2013).

Chapter 3 proposes an alternate model for the production of large basal structures in continental ice sheets, particularly the structures observed in subdued basal topography in the interior of northern Greenland (*Bell et al.*, 2014). I found that thermally controlled slippery patches at the ice sheet base can migrate downstream over time. Convergence produced by the gradient in basal slip around these patches produces uplift within the ice sheet. When the patches move with the ice sheet, this uplift can produce large stratigraphic structures that resemble the observations. This new feedback stresses the importance of time-variable basal slip and enlarges our understanding of the relationship between slip and stratigraphy. Chapter 3 was published in Geophysical Research Letters in 2014 (*Wolovick et al.*, 2014).

Chapter 4 generalizes the connection between basal slip and internal stratigraphy found in Chapter 3. Here I used a kinematic model in a moving reference frame to identify overturning vortices that form in the lower portion of the ice column above a moving sticky patch. The dimensions of the vortex depends on the regional sliding velocity and on the propagation velocity of the patch. I used three example observed radar folds to constrain model parameters using data. This chapter has been submitted to the Journal of Geophysical Research: Earth Surface.

Chapter 5 returns to basal freeze-on by exploring the conditions necessary to produce large basal freeze-on structures inside ice sheets. I explore the dominant factors controlling both conductive cooling and supercooling, as well as the ice flow conditions that encourage the formation of large basal structures from refrozen ice. I conclude with a discussion of the water supply and glaciological settings that promote basal freeze-on, as well as the settings where large basal structures are better explained by traveling patches. Chapter 5 is in preparation for publication.

Chapter 2

Identification and control of subglacial water networks under Dome A, Antarctica

Michael J. Wolovick, Robin E. Bell, Timothy T. Creyts, and Nicholas Frearson.
Published in Journal of Geophysical Research: Earth Surface, Vol. 118, 1-15, 2013

2.1 Abstract

Subglacial water in continental Antarctica forms by melting of basal ice due to geothermal or frictional heating. Subglacial networks transport the water from melting areas and can facilitate sliding by the ice sheet over its bed. Water flows underneath an ice sheet mainly down gradients in ice overburden pressure and bed elevation. We identify small (median 850 m) water bodies within the Gamburtsev Subglacial Mountains in East Antarctica organized into long (20-103 km) coherent drainage networks using a dense (5 km) grid of airborne radar data. The individual water bodies are smaller on average than the water bodies contained in existing inventories of Antarctic subglacial water and most are smaller than the mean ice thickness of 2.5 km, reflecting a focusing of basal water by rugged topography. The water system in the Gamburtsev Subglacial Mountains reoccupies a system of alpine overdeepenings created by valley glaciers in the early growth phase of the East Antarctic Ice Sheet. The networks follow valley floors either uphill or downhill depending on the gradient of the ice sheet surface. In cases where the networks follow valley floors uphill they terminate in or near plumes of freeze-on ice, indicating source to sink transport within the basal hydrologic system. Because the ice surface determines drainage direction within the bed-constrained network, the system is bed-routed but surface-directed. Along-flow variability in the structure of the freeze-on plumes suggests variability in the networks on long (10's of ka) timescales, possibly indicating changes in the basal thermal state.

2.2 Introduction

Subglacial water networks transport mass and energy underneath continental ice sheets.

Their presence influences ice sheet thermal structure, rheology, and basal lubrication. Changes in basal lubrication are responsible for a wide range of dynamic ice sheet behavior, including streaming and surging (e.g. *Cuffey and Paterson*, 2010). Networks with widths greater than several times the ice thickness have been traced using the characteristic signature they leave in ice surface curvature (*Remy and Legresy*, 2004). Other water networks are active over timescales from months to years and have been traced by correlating the filling and draining cycles of active lakes identified using repeat-track analysis of satellite altimetry data (*Gray et al.*, 2005; *Fricker et al.*, 2007, 2010; *Smith et al.*, 2009). Satellite altimetry has also been used to identify active linkages between individual subglacial lakes (*Wingham et al.*, 2006) identified previously using Radio-Echo Sounding (RES) data (*Siegert et al.*, 2005). Networks identified using satellite remote sensing tend to have lengths on the order of 10-100 km, while the most abundant individual water bodies identified using RES are on the order of a few km wide (*Dowdeswell and Siegert*, 1999, 2003). Other authors have located individual subglacial water bodies using RES measurements of reflectivity, morphology, hydraulic gradient, or basal roughness (e.g. *Peters et al.*, 2005; *Carter et al.*, 2007; *Oswald and Gogineni*, 2008). In this paper, we use a dense grid of RES data to identify hydrologic networks within the Gamburtsev Subglacial Mountains (hereafter, Gamburtsevs) in East Antarctica.

The Gamburtsevs are a mountain range completely covered by ice and are located underneath Dome A, the highest point of the East Antarctic Ice Sheet (EAIS) (Figure 2.1 a and b). They were created by the rejuvenation of a Proterozoic orogenic crustal root during Permian and Cretaceous rifting (*Ferraccioli et al.*, 2011). The morphology of the mountains is dominated by a dendritic valley network created by a pre-glacial fluvial system overprinted by alpine-style glacial features during the early growth of the EAIS (*Bo et al.*, 2009). Erosion has been negligible since the EAIS was well established at 14-34 ma (*Cox et al.*, 2010; *Jamieson et al.*, 2010). The mountains have been shielded from subglacial erosion by low ice velocities (*Rignot et al.*, 2011), the presence of cold-based ice (*Pattyn*, 2010), and by the widespread presence of basal freeze-on ("accretion") that shielded the mountain peaks from contact with subglacial water (*Creyts et al.*, 2014)[1]. Accretion processes appear to be active, producing what have been described as "valley head" and "valley wall" accretion ice reflectors (*Bell et al.*, 2011). The valley head reflectors form organized plumes of accreted ice that are imaged up to 100 km from their source regions in the direction of ice flow. Five of the nine networks we identify terminate at or near the source regions of valley head accretion reflectors identified by *Bell et al.* (2011), indicating source to sink transport within the basal hydrologic system.

[1]This reference has been changed from the published version, because *Creyts et al.* (2014) was in review when this chapter was originally published.

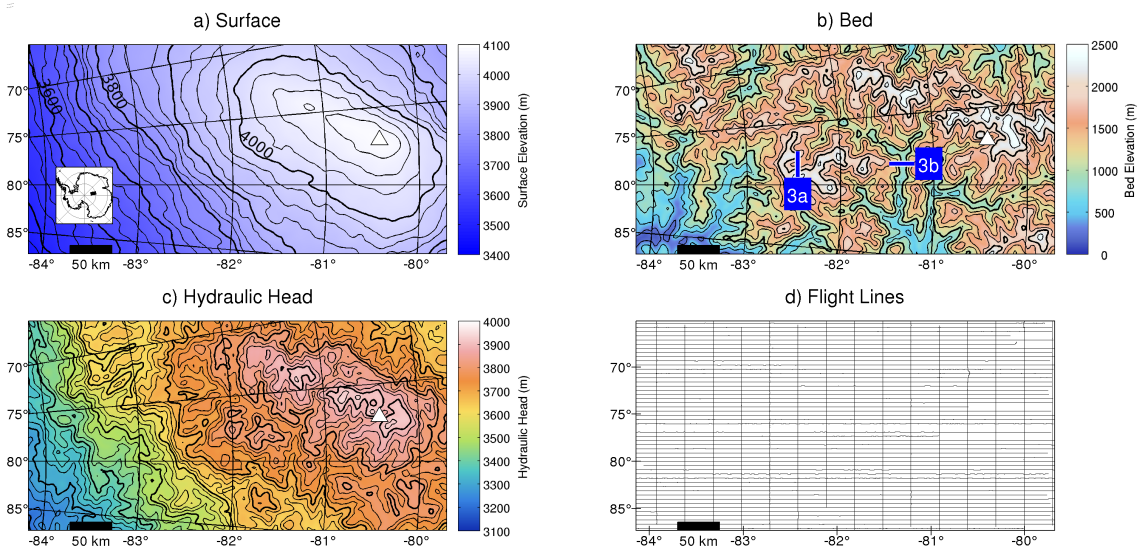

Figure 2.1: Geographic setting: (a) surface elevation relative to WGS84 from *Bamber et al.* (2009), smoothed at a 5 km wavelength, with thin contours at 25 m and thick contours at 100 m, (b) bed elevation, gridded with a minimum curvature algorithm and smoothed at a 5 km wavelength, with thin contours at 250 m and thick contours at 1000 m. Blue lines show the locations of the radar echograms in Figure 3, (c) hydraulic head, calculated from (a) and (b), with thin contours at 25 m and thick contours at 100 m, and (d) distribution of the flight lines that were used for this study. Inset map shows survey area in relation to the Antarctic grounding line.

2.3 Methods

2.3.1 Survey

The data presented in this paper were collected in December 2008 and January 2009 by the AGAP (Antarctic's GAmburtsev Province) expedition as part of the International Polar Year 2007-2009. The main grid lines of this survey are spaced 5 km apart and oriented roughly parallel to local north, while the tie lines are spaced 33 km apart and oriented roughly parallel to local east (Figure 2.1d). The survey was conducted with two Twin Otter aircraft equipped with ice-penetrating radars, laser ranging systems, gravimeters, and magnetometers. The two planes were based at separate camps (AGAP-S and AGAP-N) that surveyed the southern and northern halves of the grid, respectively. The area surveyed from AGAP-S was located over the summit and southern flank of Dome A, while the area surveyed from AGAP-N included the transition from the northern flank of Dome A into the fast flowing Lambert Glacier. To avoid complications associated with interpreting data from different radar systems and glaciological regimes we simply report on data collected from AGAP-S in this paper.

2.3.2 Radar System and Processing

The Lamont-Doherty Earth Observatory radar system, based on designs from the Center for the Remote Sensing of Ice Sheets (*Gogineni et al.*, 2001; *Jezek et al.*, 2006), has a center

frequency of 150 MHz, a bandwidth of 10 MHz, and a transmit power of 800 W. The system transmits a low-gain 3 μs and a high-gain 10 μs pulse that are combined in post-processing. Before decimation, the average along-track trace spacing is 1.3 m and the range bin sample size is 0.7 m in ice. The data are pulse compressed and then migrated with a 1D Synthetic Aperture Radar algorithm assuming point scattering targets following *Heliere et al.* (2007). The time resolution of the pulse compression algorithm is 10^{-7} s, or 8.4 m of range in ice. We scale the matched filter of the migration algorithm to eliminate the effect of aperture size on echo power by dividing the filter by the number of bins over which it is applied. The along-track resolution of the SAR algorithm (reciprocal of the Doppler bandwidth) is depth-dependent but is 20 m for ice depths typical of the Gamburtsevs. The data are decimated by a factor of 10, resulting in a final resolution of 13 m in the horizontal and 7 m in the vertical. The bed echo is picked with a hybrid manual-automatic system using the steepest vertical gradient or the rising edge of the signal to represent the bed depth. The bed returned power is the brightest pixel within 50 m of the bed depth. We low-pass filter the output of the picking algorithm along track at 60 m. The ice thickness measurements have an RMS crossover error of 69 m and the bed returned power measurements, corrected for geometric spreading, have an RMS crossover error of 6.0 dB. Of the 6.0 dB errors in bed returned power, 3.7 dB can be attributed to variability in transmitted power and system characteristics, as measured by the standard deviation of the direct arrival. Ice thickness is gridded using a minimum curvature algorithm and then smoothed using a Gaussian filter with a standard deviation of 2.5 km, corresponding to a nominal cutoff wavelength equal to the line spacing of 5 km. Ice thickness is converted to bed elevation using the surface Digital Elevation Model (DEM) from *Bamber et al.* (2009) smoothed in the same manner as the ice thickness grid.

2.3.3 Water Identification

We use the intersection of two methods to identify subglacial water bodies: reflectivity analysis and manual digitization. In the reflectivity analysis we correct observed bed echo power for englacial attenuation to map reflectivity anomalies. We use high reflectivity anomalies to discriminate potential water bodies. In the manual digitization analysis an operator examines the radar echograms and selects reflectors as potential water bodies on the basis of their morphological fit to specified criteria (Section 2.3.5). The output of the first method is a set of individual points exceeding the reflectivity threshold, and the output of the second method is a set of line segments corresponding to discrete reflectors that meet the criteria. We combine the outputs from both methods by taking those picked candidates that contain bright reflectivity anomalies within their horizontal extent to produce our highest confidence identification of water bodies.

2.3.4 Reflectivity Anomalies

To convert the observed echo power to basal reflectivity anomalies, we correct for geometric spreading assuming spreading scales with the inverse squared power of the range. The observed echo power has a range of 119 dB. While the absolute magnitude of the geometric correction is large (mean=64.7 dB) the variability is small (range=9.2 dB, standard devi-

ation=1.38 dB). Most of the observed variability in echo power comes from sources other than geometric spreading. The radar equation we use, following the notation of *Matsuoka et al.* (2010), is

$$[P]_{dB} = [K]_{dB} - 2[L]_{dB} - [G]_{dB} + [R]_{dB}, \tag{2.1}$$

where square brackets represent quantities in the decibel scale ($[X]_{dB} = 10log_{10}(X)$), P is the observed echo power, K is a constant term including transmitted power, system gain, processing gain, birefringence and surface transmission, L represents one-way attenuation losses, G represents geometric spreading losses, and R represents basal reflectivity, the desired signal. We assume losses from birefringence and surface transmission to be constant. Correcting the received signal for geometric spreading losses produces geometrically corrected power P^c, which is

$$[P^c]_{dB} = [P]_{dB} + [G]_{dB} \tag{2.2}$$

where geometric spreading losses are $[G]_{dB} = 2[H + D/n]_{dB}$, H is the height of the aircraft above the ice surface, D is the ice depth, and $n = \epsilon^{1/2} = 1.78$ is the index of refraction of ice.

Anomalies in $[P^c]_{dB}$ are caused by either changes in basal reflectivity $[R]_{dB}$ or changes in attenuation $[L]_{dB}$. In order to remove the effects of attenuation, we perform a regional attenuation correction based on a linear best-fit to a plot of $[P^c]_{dB}$ vs D (*Jacobel et al.*, 2010). The regional attenuation correction is applied over the survey area seen in Figure 2.1 (250 km x 500 km). For comparison, the *Jacobel et al.* (2010) correction applied to a single traverse line 1700 km long. The AGAP regional attenuation correction has a one-way slope of 11.7 dB/km and a correlation coefficient of -0.83 (Figure 2.2). This correction represents the mean dependence of total attenuation from all sources on ice thickness between separate sites, not the depth-averaged attenuation rate at any one site. Total attenuation is the integral of local attenuation rate over the ice thickness. Local attenuation rate depends weakly on the concentration of chemical impurities and strongly on ice column temperature (*MacGregor et al.*, 2007) with temperature in turn depending on ice thickness and thermal boundary conditions (geothermal flux, accumulation rate, and surface temperature). The regional attenuation correction simply represents an empirical measure of the first-order dependence of geometrically corrected returned power on ice thickness (Figure 2.2) without considering the nonlinear dependence of attenuation rate on ice thickness. We address the robustness of our interpreted water networks to changes in attenuation rate in more detail in the discussion (Section 2.5.1). The residual to the best-fit correction is the reflectivity anomaly $\Delta[R]_{dB}$.

We correct for horizontal deviations from the regional average attenuation rate by removing a long-wavelength signal from $\Delta[R]_{dB}$. Horizontal deviations in attenuation rate are expected based on variations in temperature caused by changing boundary conditions and ice thickness (*Matsuoka*, 2011). However, horizontal advection from ice flow acts to smooth out small scale changes in boundary conditions. On the one hand, consider the characteristic diffusive equilibration time t of an ice sheet with the average ice thickness in our survey area D=2.5 km: $t = D^2/\kappa$ 150 ka, with diffusivity $\kappa = 1.3\text{x}10^{-6} m^2 s^{-1}$. Equating horizontal advective timescales with vertical diffusive timescales, and assuming ice moves at a rate of

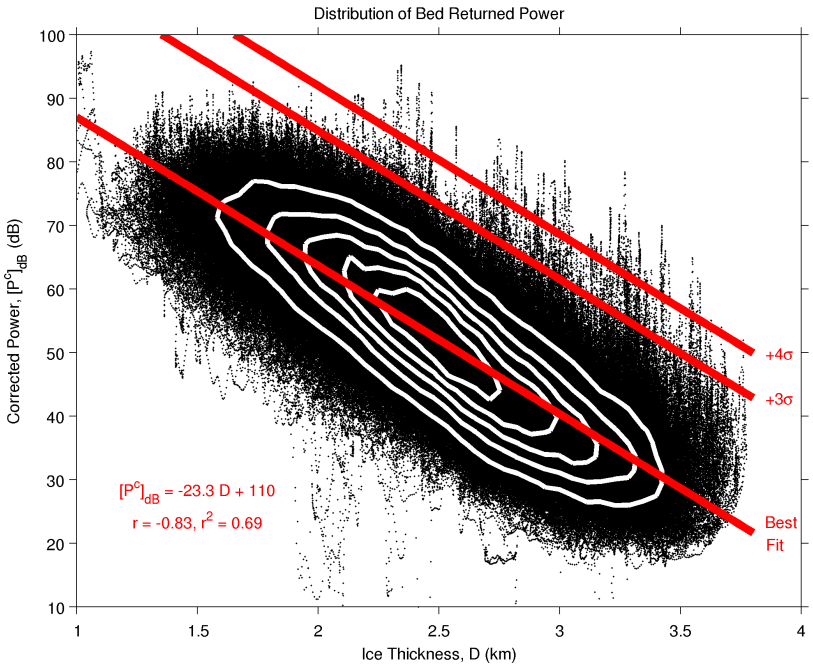

Figure 2.2: Distribution of geometrically corrected bed returned power with respect to ice thickness. White contours represent the probability density function of the data. Red lines represent the best fit regional attenuation cutoffs and 3σ, 4σ thresholds for comparison. In practice the thresholds are defined and applied after the long-wavelength signal from Figure 2.4a is removed.

$1ma^{-1}$ ($1.7ma^{-1}$ measured at AGAP-S, (*Bell et al.*, 2011)), this corresponds to a flowline averaging length of 150 km. On the other hand, horizontal velocity should be slower near the bed and near the dome, suggesting a smaller averaging length may be appropriate. We use an averaging window of 50 km with a Gaussian filter (standard deviation= 25 km), while acknowledging that the full solution to this problem would involve a 3D thermo-mechanical model of the ice sheet around Dome A. The reflectivity anomaly with the long-wavelength signal (Section 2.4.1) removed is called the short-wavelength reflectivity anomaly $\Delta[R^{sw}]_{dB}$. To preserve our ability to detect small water bodies we do not attempt to use a griding algorithm on $\Delta[R^{sw}]_{dB}$. Instead, we identify points with values of $\Delta[R^{sw}]_{dB}$ exceeding one of two thresholds, discussed below.

We aim to create a conservative list of reflectors we are confident are water bodies, rather than to make an exhaustive list of all possible water in the Gamburtsevs. Our goal in threshold selection is to minimize false positives at the expense of allowing false negatives. We use thresholds based on the statistics of the $\Delta[R^{sw}]_{dB}$ dataset, 3 and 4 standard deviations (+19.4 dB and +25.9 dB, corresponding to probabilities of $p < 0.13\%$ and $p < 0.0032\%$ for an ideal normal distribution) to distinguish potential water bodies. We discuss how the number of points identified as potential water bodies changes with each threshold below (Sections 2.4.1, 2.4.3). Others authors have used a range of thresholds to delineate basal water. The expected reflectivity contrast between wet and dry beds is 10-15 dB (*Peters et al.*, 2005) although this value is sensitive to basal roughness and the salinity of the water. *MacGregor et al.* (2012) and *Matsuoka* (2011) described 10 dB as the "nominal" threshold

for distinguishing wet and dry beds. *Dowdeswell and Siegert* (2003), used the range of 10-20 dB. *Jacobel et al.* (2010) identified two overlapping normally distributed populations (wet and dry) with a mean difference of 7 dB. *Oswald and Gogineni* (2008) found two overlapping normal distributions with means separated by 10 dB. *Peters et al.* (2005) used a gradation of bed reflectivity spanning 24 dB to distinguish basal conditions with varying degrees of water coverage and saturation. *Carter et al.* (2007) used a threshold of 2 dB, relative to a water body's immediate surroundings, as one of several criteria to define "definite lakes". Our 19.4 dB and 25.9 dB thresholds are more conservative than previous studies to minimize the identification of dry bed as wet (false positives) at the expense of allowing some wet bed to go undetected (false negatives).

2.3.5 Manual Digitization

Visual inspection of radar echograms has been used extensively to identify subglacial water bodies (*Oswald and Robin*, 1973; *Siegert et al.*, 1996, 2005). To minimize subjectivity, we established the picking criteria before digitization began. Our criteria are (1) brightness relative to surroundings at a similar depth, (2) location at or near a topographic minimum, (3) echo abruptness (vertical thinness), and (4) hydraulic flatness. Visible drawdown of the ice sheet stratigraphy indicates highly localized melt rates and can be supporting evidence for identifying basal water. Because basal water can flow away from melt sources and because melt rates must be large relative to horizontal ice velocity for drawdown to be visible, we have not used drawdown as a primary criterion for identifying water. We use the criterion of echo abruptness as a proxy for specularity, or basal smoothness (*Oswald and Robin*, 1973). A rough bed will reflect energy back towards the aircraft from a wider range of angles than a smooth bed, that appear at a greater range in an echogram than the nadir echo. We classify reflectors that unambiguously meet all of the criteria as "clear picks" and reflectors for which some of the criteria are absent or ambiguous "unclear picks" (Figure 2.3). Both types of picks are considered water "candidates".

During digitization, candidates are picked by an operator examining the radar data on a computer monitor and selecting endpoints of linear reflectors that meet the criteria. The operator has to make a subjective decision based on the criteria that a given reflector represents a contiguous morphological feature. The distance between the endpoints represents the length of the candidate. To prevent differences in picking "style" from introducing a bias into the data, the same operator picked the entire dataset. The operator has to be able to see enough detail in the echogram to judge that the criteria have been met before selecting a candidate. In practice it is difficult for an operator to assess whether the criteria have been met for candidates less than two to three hundred meters long ($\sim$ 20 pixels). To ensure we only pick candidates that are hydraulically flat, we discard candidates with a range in hydraulic head greater than the uncertainty in hydraulic head, described below.

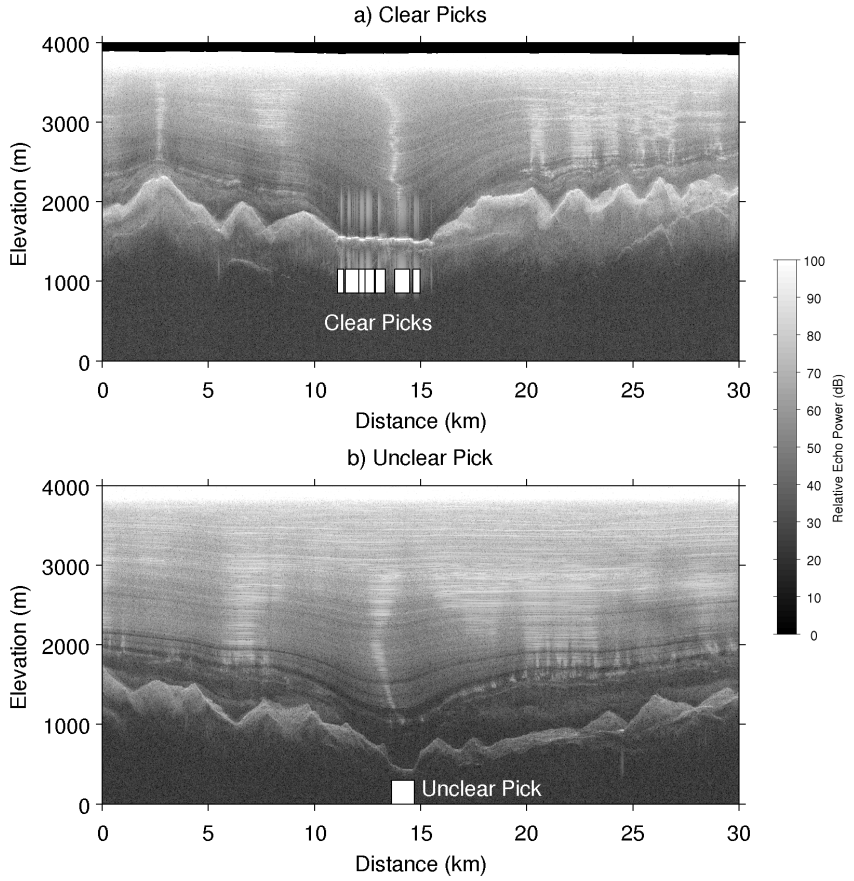

Figure 2.3: Examples of clear and unclear picks encountered in the manual digitization process (both radar echograms have been elevation-adjusted and returns above the surface have been blanked out; the color scale has a range of 100 dB): (a) examples of clear manual picks and (b) an example of an unclear manual pick. The clear picks in (a) are not only brighter than the other valleys in the image, they are brighter than the peaks as well, even though valleys should experience more attenuation than peaks. There are small apparent vertical offsets between the clear picks in (a) but individual water bodies are both flat and vertically thin. In addition, drawdown of the ice sheet stratigraphy indicates basal melt here. The unclear pick in (b) is flat in its right half and vertically thin throughout, but there are no nearby reflectors at comparable depth to compare against. The bright reflector near 25 km in (b) is a clear pick with a length of 0.37 km, near the limit of the resolution of manual digitization.

2.3.6 Hydraulic Head

Subglacial water flows down the gradient of hydraulic head, a quantity calculated from both the ice surface and the bed elevation, although surface gradients are weighted roughly 11 times more than bed gradients in driving water flow (*Shreve*, 1972; *Clarke*, 2005). Assuming water pressure is equal to ice overburden pressure, hydraulic head (h), is calculated from surface elevation (S), bed elevation (B), and ice thickness (D=S-B), via

$$h = (\rho_i/\rho_w)D + B, \tag{2.3}$$
$$h = (\rho_i/\rho_w)S + (1 - \rho_i/\rho_w)B, \tag{2.4}$$

with ice density $\rho_i = 917 kgm^{-3}$, and water density $\rho_w = 1000 kgm^{-3}$ (*Shreve*, 1972; *Clarke*, 2005). Hydraulic head is calculated both along flight lines and for the gridded DEM. To determine the uncertainty in hydraulic head along flight lines we propagate the crossover errors in bed elevation and the error in the surface DEM (mean value of 2.6 m within our survey area (*Bamber et al.*, 2009)) through equation 2.4, assuming that the crossover error in ice thickness represents the error in bed elevation. The root-mean-square uncertainty in hydraulic head is 8.2 m. To determine drainage routes and catchment area, we apply a routing algorithm to the gridded hydraulic head after first filling closed basins. We use a multiple slope routing algorithm (*Quinn et al.*, 1991). Hillslope routing algorithms have been used extensively to delineate subglacial flow paths beneath both glaciers and ice sheets (e.g. *Flowers and Clarke*, 1999; *Le Brocq et al.*, 2009; *Pattyn*, 2010). Basins are filled by iteratively raising each grid cell a small spillover amount above its sill level. Less than 5% of the grid cells require basin fill, with a mean fill level of 4 m. The maximum basin fill required for any single grid cell is 24 m.

2.4 Results

2.4.1 Reflectivity Anomalies

The long-wavelength reflectivity anomalies are characterized by an east-west gradient in the north of the survey grid, with the highest values occurring in the northeast corner (Figure 2.4 a). In the south of the survey grid, the long-wavelength reflectivity anomalies are characterized by a central high flanked by lows on the east and west edges. If the long-wavelength reflectivity anomalies represent thermal structure, the lows correspond to warm regions and the highs correspond to cold regions. Long-wavelength patterns in the thermal boundary conditions- geothermal flux, accumulation rate, and surface temperature- can produce a signal in thermal structure, as can long-wavelength patterns in ice thickness or strain heating. However, long-wavelength patterns in the impurity content of the ice or water distribution at the bed can also produce a signal in long-wavelength reflectivity (*MacGregor et al.*, 2012). Further interpretation of the long-wavelength reflectivity signal will require studies of the ice sheet thermal structure, local climate history, and subglacial geology.

The short-wavelength reflectivity anomalies contain 9073 points (0.44% of the total) at the 3σ level and 2682 points (0.13%) at the 4σ level. These percentages are 3 times and 40 times as large, respectively, as would be expected for an ideal normal distribution. Previous studies (*Oswald and Gogineni*, 2008; *Jacobel et al.*, 2010) show that basal reflectivity is well fit by two overlapping normal distributions (wet bed and dry bed). These results give us confidence that we are sampling a small wet bed distribution rather than the tail of the dry bed distribution. Both sets of points are generally located in local topographic minima, and several valleys contain distinct clusters of 4σ anomalies (Figure 2.4 b). The minimum ice thicknesses containing 3σ and 4σ anomalies are 1645 m and 1971 m, respectively. The raw

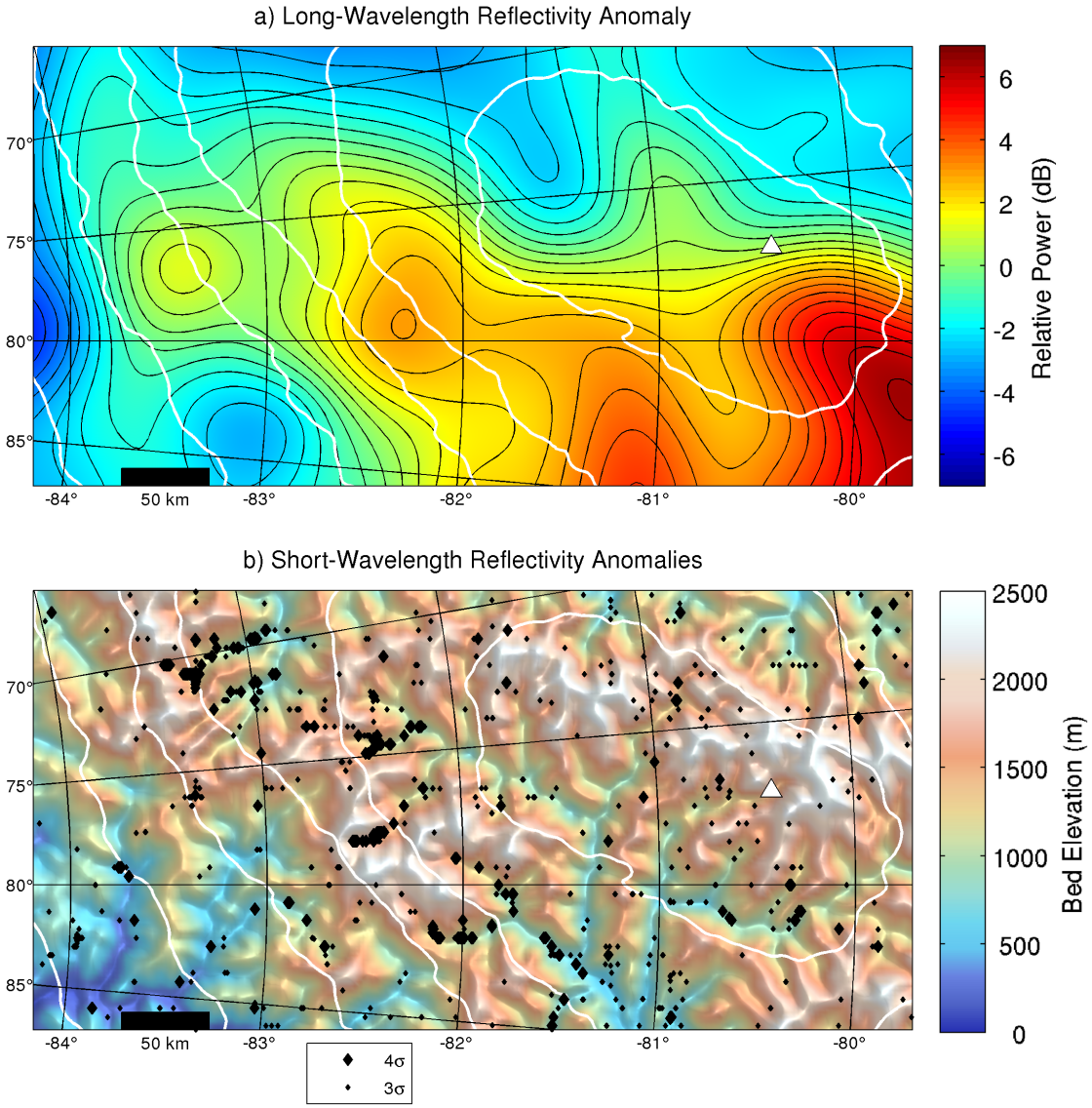

Figure 2.4: Reflectivity anomalies: (a) long-wavelength (50 km) reflectivity anomaly and (b) short-wavelength reflectivity anomalies that passed the 3σ and 4σ thresholds overlain on bed elevation. Hill shading for bed elevation is from two perpendicular light sources, one at the top of the page and one to the right of the page, both at an elevation of 75° above the horizon. Large diamonds represent 4σ points and small diamonds represent 3σ points. White lines are 100 m surface elevation contours.

distributions of ice thickness for both sets of points show broad maxima between 2500 and 3500 m (Figure 2.5 a and b). When the distributions are normalized by the distribution of the overall ice thickness dataset they show a strong increase in the fraction of the basal area containing reflectivity anomalies with increasing ice thickness (Figure 2.5 c and d). However, even at large ice thicknesses the reflectivity anomalies are a small percentage of the total basal area. No single ice thickness contains more than 5% of 3σ reflectivity anomalies or 1% of 4σ reflectivity anomalies. Overall, these results are consistent with subglacial water that is generated by melting in deep valleys.

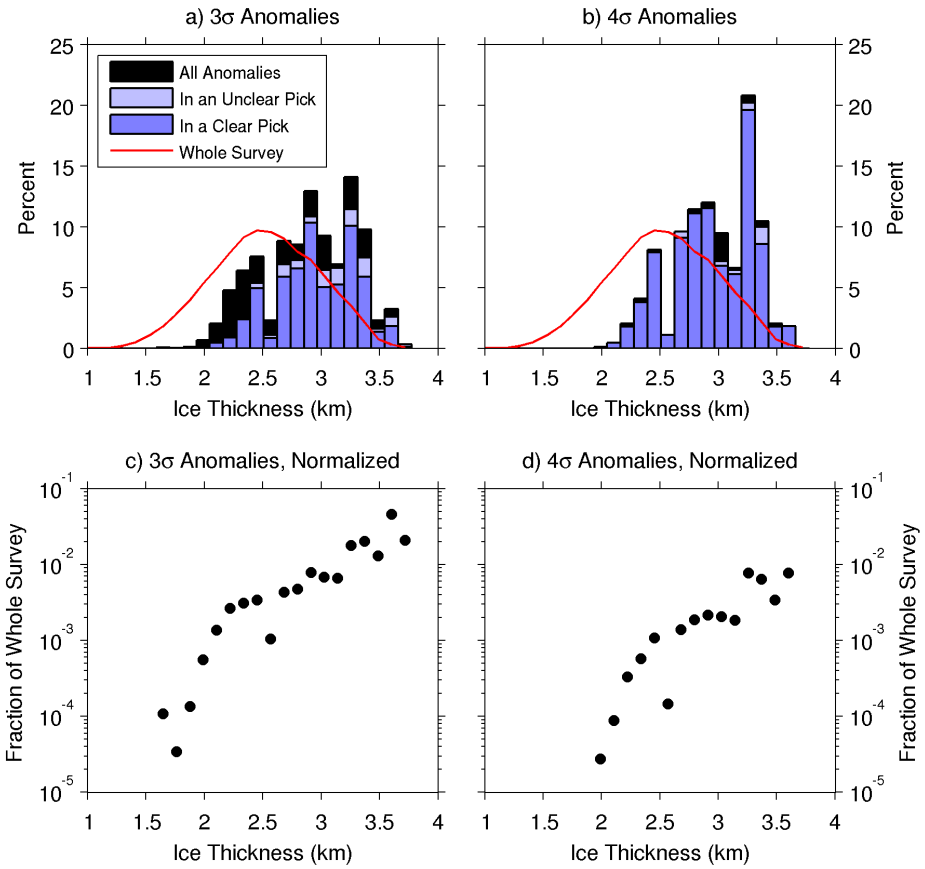

Figure 2.5: Distribution of ice thickness for the reflectivity anomalies: (a) distribution of ice thickness for 3σ reflectivity anomalies. Black bars represent all anomalies, light blue bars represent anomalies contained within unclear picks, dark blue bars represent anomalies contained within clear picks, and the red line represents the distribution of ice thickness for the entire dataset, (b) same as (a), but for 4σ anomalies, (c) distribution of ice thickness for 3σ anomalies, normalized by the distribution of ice thickness for the overall dataset and plotted on semilogarithmic axes, and (d) same as (c), but for 4σ anomalies.

2.4.2 Manual Digitization

Digitized candidates are found throughout the valley networks of the Gamburtsevs but often cluster in the valleys that also have clusters of reflectivity anomalies (Figure 2.6 a, cf. Figure 2.4 b). There are 172 clear picks and 300 unclear picks, of which 161 and 254 (94% and 85%) passed the hydraulic flatness criterion. These include 0.59% and 0.69% of all data points, respectively. Clear picks are rare in the southeast corner (lower left on all map figures) of the grid, where the thickest ice is located, although scattered candidates are present in valleys throughout the survey area (Figure 2.6 a). The absence of water in the southeastern portion of the study area may be because downhill flow limits ponding and prevents us from detecting basal water as discussed later (Section 2.4.4). It could also be because thermal boundary conditions are different and meltwater is not generated here. As with the reflectivity anomalies, the raw distributions of ice thickness within the candidates display broad maxima between 2500 and 3500 m (Figure 2.7 a and b), while the normalized

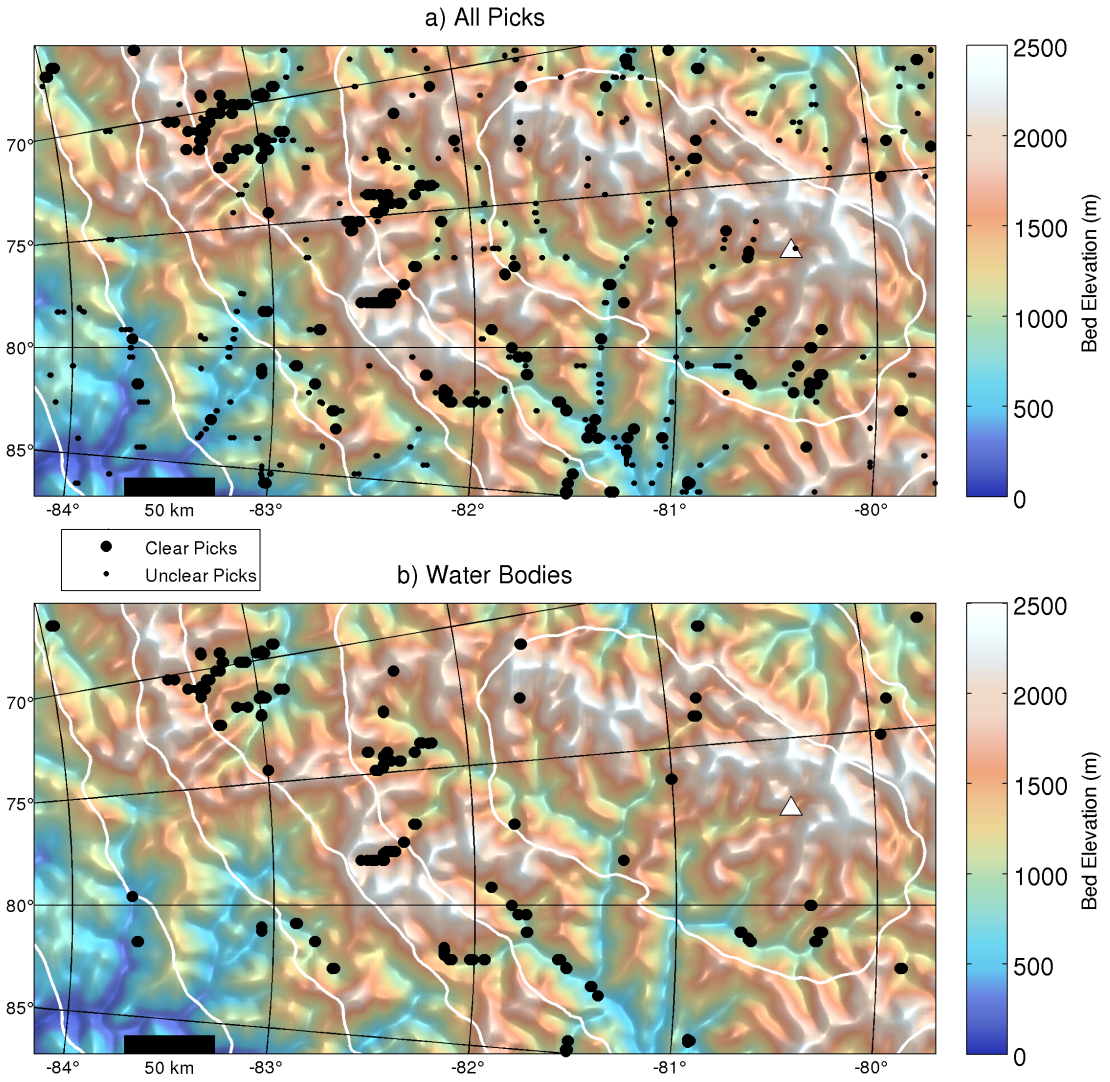

Figure 2.6: Manually digitized candidates: (a) all manually picked candidates overlain on bed elevation. Hill shading is identical to Figure 2.4b. Large black circles represent clear picks and small black circles represent unclear picks. White lines represent 100m surface elevation contours and (b) the subset of clear picks that also contain 4σ reflectivity anomalies. This intersection set represents the candidates we are most confident actually represent water bodies.

distributions show a strong increase in the fraction of the bed contained by candidates with increasing ice thickness (Figure 2.7 c and d). Manual digitization identifies a larger fraction of the deep ice as containing water than the reflectivity analysis does, at 23% for the unclear picks and 14% for the clear picks (Figure 2.7 c and d, cf Figure 2.5 c and d).

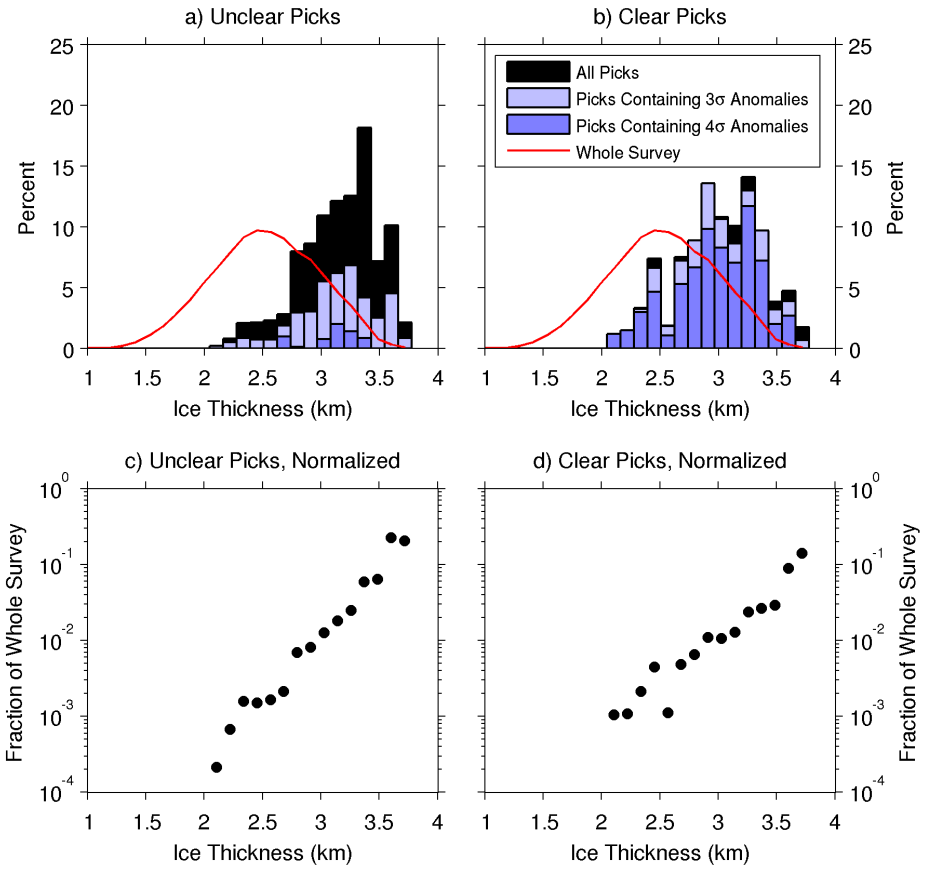

Figure 2.7: Distribution of ice thickness for points within manually digitized water bodies: (a) distribution of ice thickness for unclear picks. Black bars represent the ice thickness of all unclear picks, light blue bars represent unclear picks containing 3σ reflectivity anomalies, dark blue bars represent unclear picks containing 4σ anomalies, and the red line represents the distribution of ice thickness for the entire dataset, (b) same as (a), but for clear picks, (c) distribution of ice thickness for points within unclear picks, normalized by the distribution of ice thickness for the overall dataset and plotted on semilogarithmic axes, and (d) same as (c), but for clear picks.

2.4.3 Overlap of Methods

The candidates most likely to represent water bodies are those that are both clear picks and contain 4σ reflectivity anomalies, the intersection set (Table 2.1). A majority, 65%, of the clear picks fall into this category. In contrast, only 4% of the unclear picks contain 4σ reflectivity anomalies. The set of 4σ anomalies is nearly as exclusive as the intersection set, with 91% of its members contained within a clear pick as opposed to 62% for the set of 3σ anomalies.

The lengths of water bodies we find in the intersection set are shorter than most of the subglacial lakes that have been found by previous studies (Figure 2.8). We compare the water bodies we find with those described by *Carter et al.* (2007) and *Siegert et al.* (2005) using kernel density estimation to approximate the underlying continuous distribution from our discrete sample of it (*Bowman and Azzalini*, 1997). The median value of our distribution

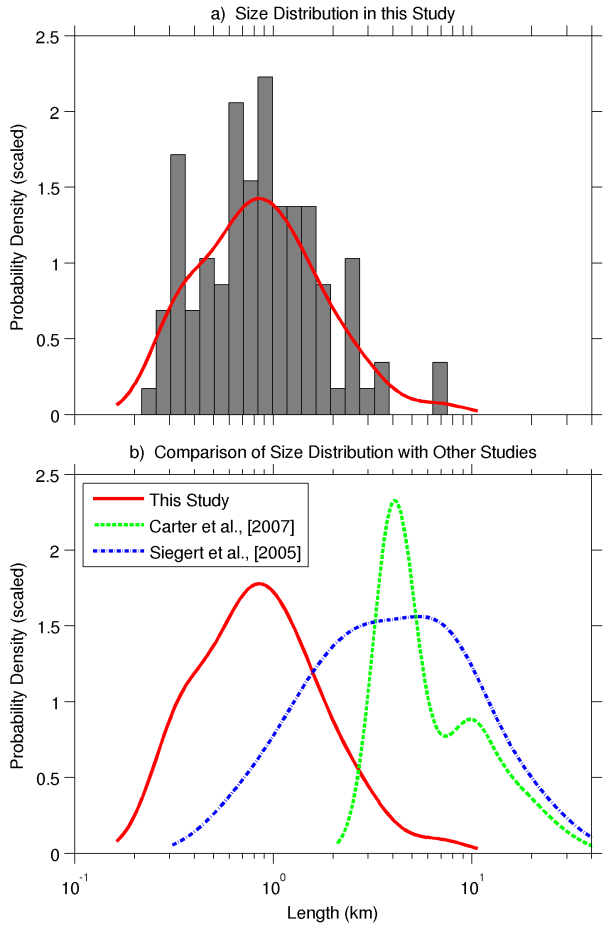

Figure 2.8: Size distribution of water bodies: (a) distribution of the logarithm of water body length for the intersection set (clear picks containing 4σ reflectivity anomalies). Gray bars represent the histogram and the red line represents a kernel density estimate of the underlying probability density function using a Gaussian kernel and (b) comparison of the probability density function in (a) with similar functions derived from published subglacial lake inventories.

is 850 m, substantially smaller than most previously discovered subglacial lakes. The *Carter et al.* (2007) inventory has a bimodal distribution with peaks at 4 km and 10 km, and the *Siegert et al.* (2005) inventory has a single broad peak with a maximum near 6 km. Our distribution may be skewed towards smaller water bodies because of the closer line spacing in the AGAP survey. The flight line spacing in the AGAP survey is 5 km, the *Carter et al.* (2007) inventory was drawn from three surveys with line spacings between 5-10 km, and the *Siegert et al.* (2005) inventory was drawn from many surveys with line spacings in the range of 5-50 km. However, while dense line spacing can explain why we do observe more small water bodies than previous surveys, it cannot explain why we do not observe any large water bodies. A more likely explanation is that rugged topography within the Gamburtsevs concentrates water within small bedrock depressions. The Gamburtsevs are considered to be among the roughest subglacial topography in Antarctica (*Ferraccioli et al.*, 2011). Elsewhere

Table 2.1: List of Water Bodies in the Intersection Set, Clear Picks Which Also Contain 4σ Reflectivity Anomalies.

Number	Lat	Lon	Length (km)	Ice Thickness (m)	Network	Number	Lat	Lon	Length (km)	Ice Thickness (m)	Network
1	-79.705	71.957	0.74	3014	-	54	-80.330	80.000	1.07	3209	G
2	-83.940	66.754	1.78	3088	-	55	-81.746	80.312	0.79	3332	E
3	-80.789	71.284	1.17	3349	-	56	-81.784	80.314	0.68	3312	E
4	-82.889	69.453	1.25	3328	A	57	-82.888	80.721	1.09	3275	I
5	-81.673	70.990	0.64	2487	-	58	-81.740	80.935	0.79	3307	E
6	-83.155	69.424	0.61	2919	A	59	-80.677	80.830	0.94	3582	G
7	-82.949	69.735	3.05	3248	A	60	-80.280	80.796	1.82	3424	G
8	-82.973	69.700	0.63	3208	A	61	-83.674	81.623	0.61	3340	-
9	-83.149	69.818	0.81	2960	A	62	-82.795	81.427	0.57	3151	I
10	-83.041	69.976	1.55	3141	A	63	-80.628	81.100	0.31	3547	G
11	-83.062	69.944	1.13	3096	A	64	-80.302	81.065	1.31	3423	G
12	-83.180	70.154	2.57	2927	A	65	-82.150	81.641	0.40	2787	E
13	-82.318	71.251	0.33	2720	-	66	-82.123	81.960	0.78	2861	E
14	-83.415	70.198	3.67	2461	A	67	-82.114	81.957	0.86	2842	E
15	-83.235	70.458	2.13	2871	A	68	-81.950	81.919	0.92	3130	E
16	-83.310	70.746	7.50	2699	A	69	-82.006	81.933	0.67	3021	E
17	-83.259	70.818	0.71	2740	A	70	-82.018	81.936	1.04	2990	E
18	-82.882	71.296	2.71	3287	B	71	-81.574	81.835	0.61	3434	F
19	-82.991	71.536	1.21	3192	B	72	-81.584	81.837	0.30	3425	F
20	-82.971	71.554	1.55	3225	B	73	-82.697	82.470	1.42	2891	I
21	-81.715	72.828	0.23	2934	-	74	-81.541	82.136	0.54	3447	F
22	-80.845	73.505	0.35	3143	H	75	-79.877	81.786	1.25	2999	-
23	-79.904	74.108	0.35	3207	-	76	-81.414	82.703	0.92	3546	F
24	-83.087	71.792	6.36	3065	B	77	-81.378	82.993	0.43	3536	F
25	-83.000	72.263	0.28	3156	B	78	-81.512	84.560	0.40	3356	F
26	-80.861	74.063	1.94	3272	H	79	-80.911	84.259	0.91	3577	-
27	-83.210	72.410	1.59	2881	B	80	-81.516	84.867	0.98	3321	F
28	-79.948	75.114	0.39	2995	-	81	-83.248	69.327	1.01	2848	A
29	-82.228	74.025	1.30	3297	C	82	-83.277	70.746	1.63	2739	A
30	-82.183	74.063	1.91	3279	C	83	-83.282	71.039	2.39	2767	A
31	-82.399	74.234	0.61	2906	C	84	-82.949	69.703	1.24	3261	A
32	-82.495	74.161	0.76	2776	C	85	-82.985	71.468	0.52	3176	B
33	-82.263	74.334	0.36	3150	C	86	-82.998	72.233	0.91	3161	B
34	-82.396	74.576	2.64	2914	C	87	-83.060	80.972	2.38	3316	I
35	-82.339	74.615	1.17	3038	C	88	-82.396	72.716	0.84	2962	-
36	-82.997	74.484	0.32	2806	-	89	-82.421	74.389	0.66	2932	C
37	-82.465	74.869	0.85	2793	C	90	-82.425	74.718	1.27	2899	C
38	-82.450	74.879	0.67	2821	C	91	-82.426	74.775	0.32	2873	C
39	-81.002	75.986	0.43	3080	-	92	-82.453	78.236	0.72	2343	D
40	-82.288	76.994	1.45	2974	D	93	-82.453	78.281	0.34	2373	D
41	-81.795	77.174	0.64	3058	-	94	-82.453	78.164	0.50	2332	D
42	-82.347	77.644	0.51	2795	D	95	-82.453	78.132	0.49	2329	D
43	-82.425	77.963	2.41	2421	D	96	-82.452	78.107	0.29	2339	D
44	-82.412	77.966	1.33	2457	D	97	-82.452	78.074	0.65	2325	D
45	-82.398	77.969	1.78	2564	D	98	-82.452	78.038	0.29	2310	D
46	-82.549	78.273	3.64	2164	D	99	-82.152	81.559	0.89	2765	E
47	-82.507	78.282	0.98	2267	D	100	-82.151	81.633	0.31	2799	E
48	-82.492	78.285	0.87	2327	D	101	-82.150	81.783	0.93	2779	E
49	-82.453	78.295	1.07	2359	D	102	-81.543	82.122	0.55	3431	F
50	-81.258	78.526	0.37	3030	-	103	-81.519	84.892	1.50	3324	F
51	-81.918	79.362	0.44	3038	E	104	-80.919	84.273	1.55	3548	-
52	-83.703	79.595	0.45	3375	-	105	-80.639	81.022	0.79	3542	G
53	-81.818	79.999	0.31	3244	E						

Lat and Lon represent the location of the pick center, ice thickness represents the mean value of all points within the pick, and a pick is counted as within a network if one of its endpoints is within 5 km of any of the network paths. Length denotes along track length.

in Antarctica, broad subglacial basins trap large subglacial lakes, but the Gamburtsevs are dominated by prominent peaks dissected by deep valleys that only allow water to collect in small bedrock depressions.

2.4.4 Water Networks

Most of the water bodies in the intersection set are clustered into 9 distinct networks that we label alphabetically A-I (Figure 2.9). Seven of the nine networks (all except G and I)

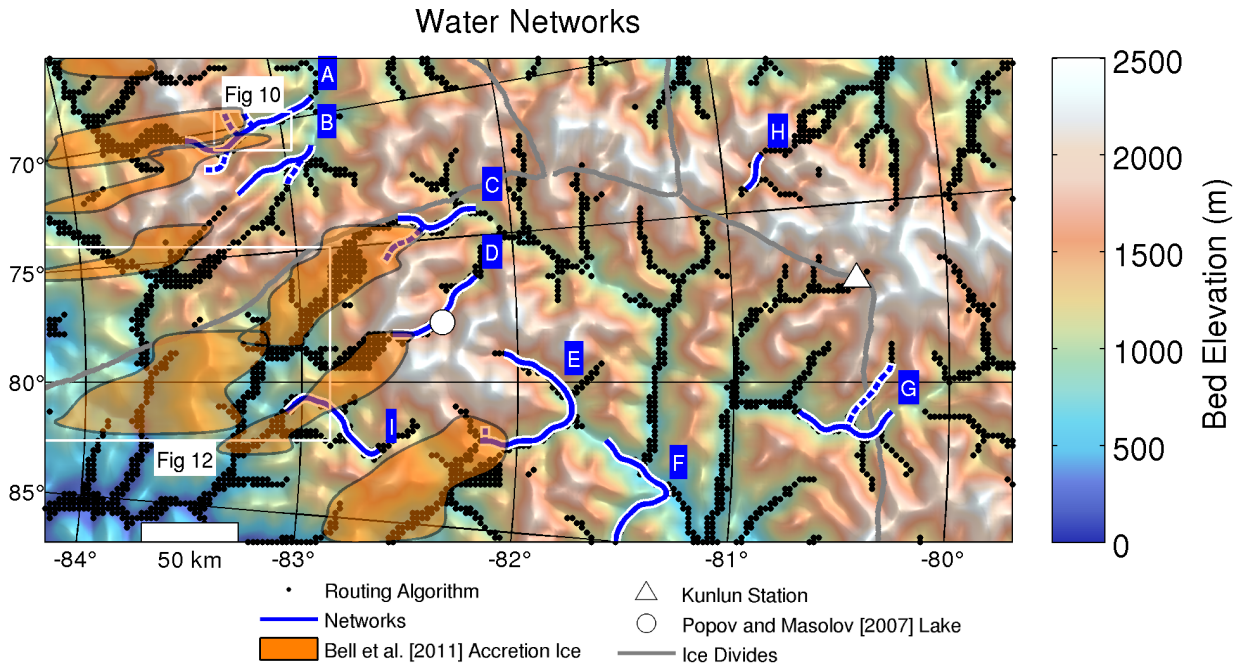

Figure 2.9: Routing algorithm and interpreted networks (A-I) overlain on bed elevation with hillshading identical to Figure 2.4b. Black dots from the routing algorithm represent all grid cells with catchment area greater than 250 km^2. Solid blue lines represent the main path of each network and dashed blue lines represent tributaries or distributaries. The orange patches represent the "valley head" accretion plumes identified by *Bell et al.* (2011). Note that the accreted ice bodies form at their upstream ends (upper right in this figure) and are subsequently advected downstream by the ice flow. Some of the water networks terminate at the start of the accretion plumes. The lake identified by *Popov and Masolov* (2007) in Russian RES data taken in the late 1980s is lake 94 in the compilation by *Siegert et al.* (2005).

flow uphill towards shallower ice with conditions that favor conductive cooling of the bed. All 9 networks fall along parts of drainage pathways determined by the hydraulic routing algorithm, and all are located within bedrock valleys (Figure 2.9). The networks we observe have lengths ranging from 20 to 103 km and catchment areas ranging from 1700 to 8700 km^2 (Table 2.2). Average hydraulic gradients in the networks are on the order of $10^{-4} - 10^{-3}$, while average ice thickness gradients are on the order of $10^{-3} - 10^{-2}$. Four of the networks that flow uphill terminate in the source regions for the valley head accretion ice imaged by *Bell et al.* (2011) (Figure 2.9). The networks may be terminated by loss of water through freeze-on to the overlaying ice sheet, or some of the water may pass through the freeze-on region and continue undetected (e.g. as narrow channels, thin films, or groundwater flow). One of the networks that does not terminate in a plume of valley head accretion ice, network B, terminates 20 km short of a valley head accretion plume. The separation between the end of the network and the start of the accretion plume suggests either episodic fluctuations in the network extent and accretion process, or that the water is undetected. One of the other networks that does not terminate in a plume of valley head accretion ice, network H, terminates near a plume of valley wall accretion ice. Network F flows out of the eastern edge of the survey grid. The remaining two networks, G and I, terminate within our survey grid without producing accretion plumes and are also the only two networks to flow downhill.

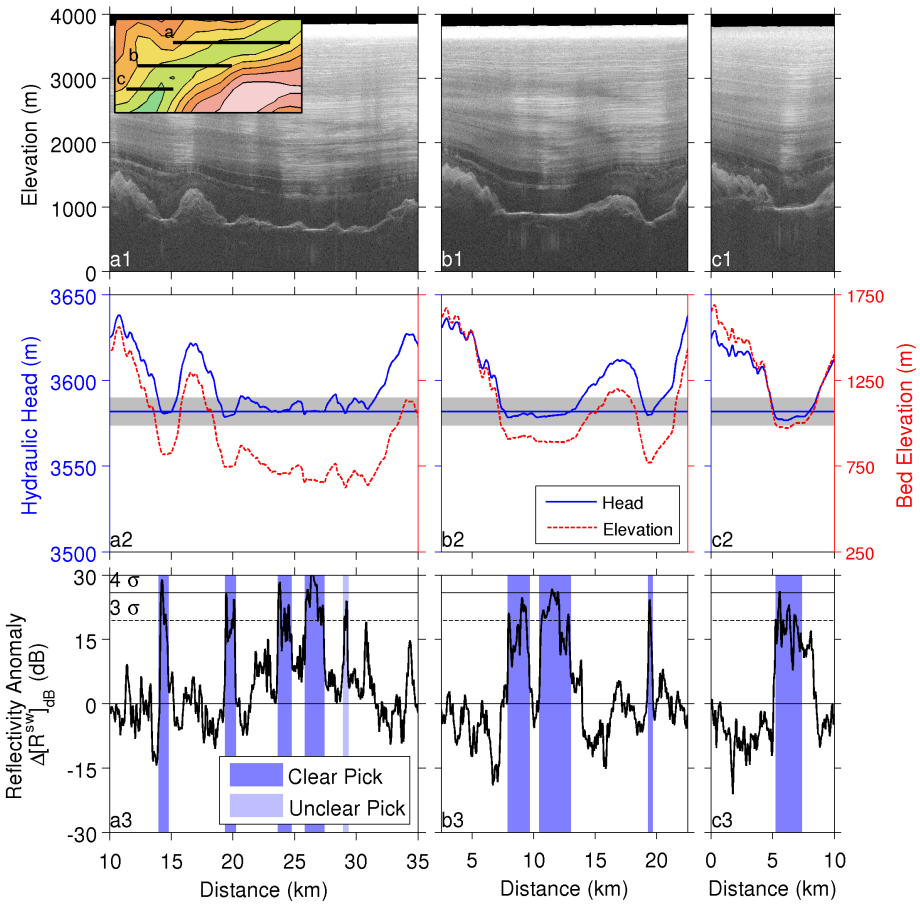

Figure 2.10: Network A: detail of 3 sequential flight lines. The first row (a1, b1, c1) shows the echograms in the same color scale as Figure 2.3. The second row (a2, b2, c2) shows bed elevation and hydraulic head. Note scale change of elevation in second row relative to first row, and of head relative to elevation. The horizontal line shows the hydraulic head in the first picked water body in a2 extrapolated to the rest of the network, and the shading represents the uncertainty in hydraulic head. The third row (a3, b3, c3) shows short-wavelength reflectivity anomalies. The dark (light) blue regions show clear (unclear) manual picks, and the solid (dashed) horizontal lines show the 4 (3) σ cutoff. 40 x 20 km inset map shows hydraulic head with 10 m contours. Location of inset map given in Figure 2.9.

Our method is optimized for identifying ponded water rather than other morphologies, and downhill flow may be associated with higher hydraulic gradients (Table 2.2) that inhibit ponding of basal water and prevent us from detecting the full extent of these networks. As a result, the water networks we observe may be biased towards uphill flow. The difficulty in imaging downhill flowing networks may explain why we observe little water in the southeast corner of the survey grid (Figure 2.4, 2.6, 2.9) despite thick ice there. It is also possible that thermal boundary conditions are different and the bed is cold here. Overall, the networks are confined within bedrock valleys, and a majority flow uphill and terminate near the source regions of basal freeze-on ice.

All of the water networks are composed of discrete individual water bodies with irregular shapes. In some cases the flight lines intersect multiple water bodies, in some cases they intersect only a single water body, and in a few cases no water bodies are observed despite

the presence of water bodies in adjacent flight lines crossing the same valley. Examples of this variable arrangement are shown in Figure 2.10. Where network A is subparallel to a flight line (Figure 2.10 a) we observe one unclear and four clear picks, three of which contain 4σ anomalies. Where network A is subperpendicular to a flight line (Figure 2.10 c) we only observed a single clear pick containing 4σ anomalies. Yet despite the variability in valley scale arrangement that we observe, all of the water bodies in this figure are within error margin of the same hydraulic head (Figure 2.10, row 2), suggesting that they are hydraulically connected to one another.

As a whole, the networks are either hydraulically flat or sloping downwards in the direction predicted by applying a routing algorithm to the gridded hydraulic head (Figure 2.11, cf. Figure 2.9). We determine the gradient of hydraulic head (Figure 2.11, Table 2.2) and ice thickness (Table 2.2 only) for each network by taking a best-fit line to the values for the individual water bodies within that network. Networks B, C, D, and H are flat and do not have statistically significant hydraulic gradients. We assign drainage direction for those networks based on the presence of freeze-on ice near one endpoint and the direction determined by the routing algorithm. It is possible that on short timescales water can flow either uphill or downhill within these networks in response to minor changes in the ice surface or effective pressure (*Wright et al.*, 2008). However, the large-scale structure of the hydraulic head is determined by the overall ice surface geometry of Dome A (Figure 2.1a,c). Over long timescales ($<\sim$ 100 ka) the water must flow uphill and feed the freeze-on ice identified by *Bell et al.* (2011), assuming that Dome A has remained stable.

Table 2.2: List of Water Networks.

Network	Length (km)	Hydraulic Gradient (m/km)	Hydraulic Gradient Uncertainty (m/km)	Ice Thickness Gradient (m/km)	Ice Thickness Gradient Uncertainty (m/km)	Catchment Area (km^2)	Number Water Bodies	Termination Style
A	75	-0.27	0.13	-13.0	1.2	4686	24	freeze-on
B	47	-0.28	0.34	-10.2	2.6	2501	9	short of freeze-on
C	44	-0.06	0.22	-13.8	2.1	3168	15	freeze-on
D	56	-0.21	0.25	-22.6	2.5	8656	16	freeze-on
E	103	-0.92	0.12	-5.3	2.1	3969	19	freeze-on
F	87	-0.53	0.12	-1.1	1.8	8367	9	exit survey area
G	58	-0.40	0.15	3.0	1.4	4097	6	unknown
H	20	-0.24	0.81	-12.9	6.9	1762	2	freeze-on
I	64	-1.50	0.22	7.9	3.4	2322	4	unknown

Length represents the length of the main path only, and both hydraulic head gradient and ice thickness gradient represent best-fit slopes to the values at individual water bodies along the main path. Note that some networks contain side-paths in addition to the main path. Catchment area represents the maximum upstream area as computed by the multiple slope algorithm for any grid cell within any of the paths. The number of water bodies represents the members of Table 2.1 within 5 km of any of the network paths.

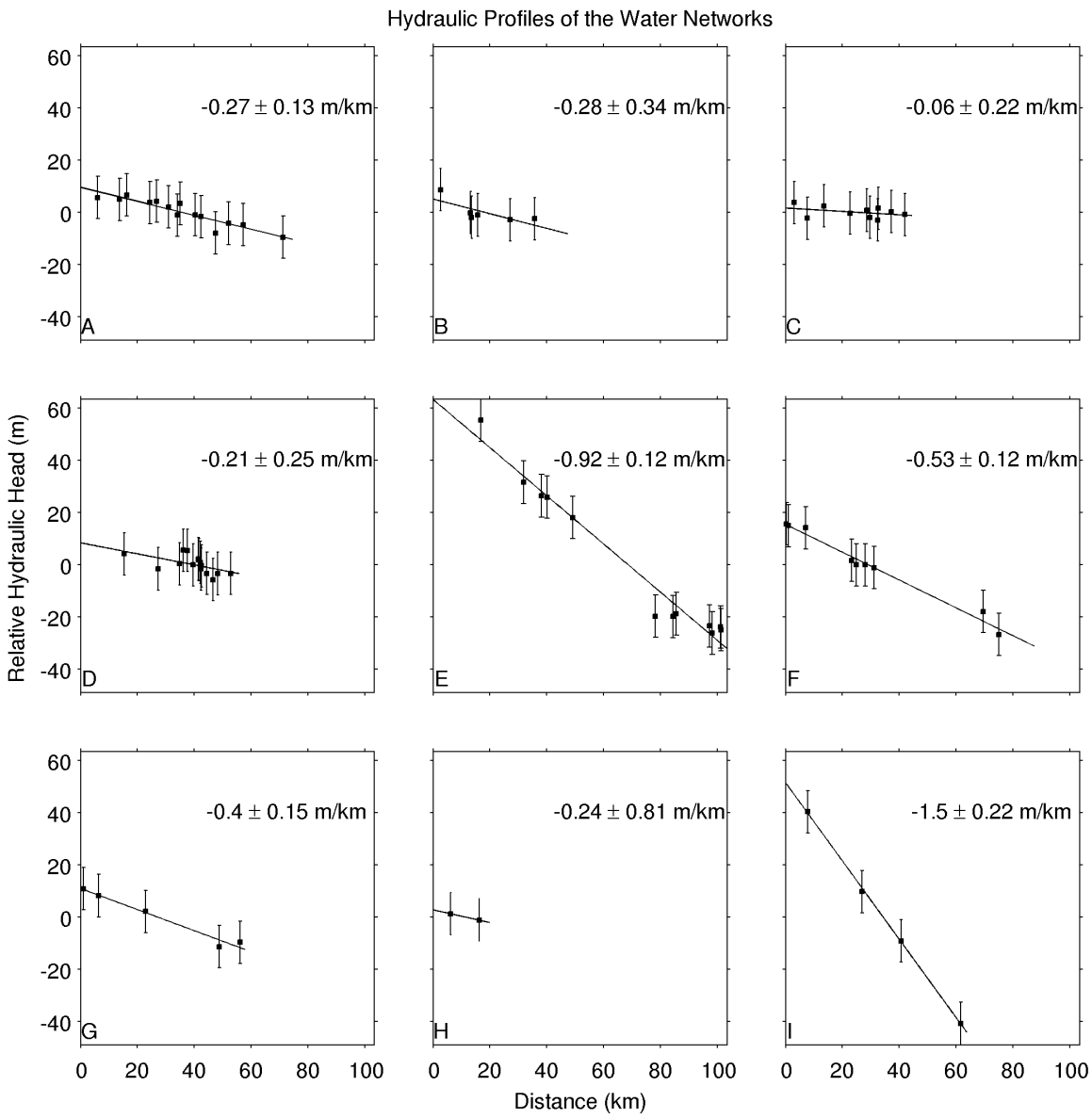

Figure 2.11: Hydraulic head of water bodies along the main paths (solid blue lines in Figure 2.9) of each network. Hydraulic head is plotted relative to the mean value within each network so that all networks can be plotted on the same scale. Only water bodies within the intersection set (clear picks containing 4σ reflectivity anomalies) are shown.

2.5 Discussion

2.5.1 Attenuation Rate

We image subglacial hydrologic networks in the Gamburtsevs using RES. Because our results partially depend on using a linear best-fit to bed returned power as a function of ice thickness ($[P^c]_{dB}$ vs D) to estimate an attenuation correction, it is important to examine the weaknesses

of this method. A single regional attenuation correction can be inaccurate if basal reflectivity depends systematically on ice thickness. *Matsuoka* (2011) has demonstrated that when bed reflectivity depends on ice thickness a linear best-fit can underestimate the attenuation correction. If basal reflectivity has a systematic dependence on ice thickness that dependence will contaminate the best-fit slope, and the regional attenuation correction will remove part of the targeted reflectivity signal in addition to the attenuation signal. Basal reflectivity can depend systematically on ice thickness if there is a specific depth below which water is found and above which the bed is frozen.

A single regional attenuation correction is, however, appropriate for the Gamburtsevs because ponded water occupies an extremely small fraction ($< 1\%$) of the total basal area. Thus, the area-averaged basal reflectivity is primarily that of a rock-ice interface and is effectively independent of ice thickness. To test this, we have tried recomputing the best-fit without all potential water bodies (3σ, 4σ, unclear picks, clear picks). The best-fit one way attenuation rate only changes by 0.31 dB/km, corresponding to maximum reflectivity anomaly errors of 0.9 dB, substantially less than the crossover errors of 6.0 dB.

Our interpreted networks are also robust against larger changes in attenuation rate. *MacGregor et al.* (2012) modeled englacial thermal structure and attenuation rate along the Vostok flowline, a glaciologically similar setting to Dome A. The depth-averaged attenuation rates in their model ranged between 5.8 and 11.8 dB/km, with the latter value being close to our best-fit regional attenuation correction. We calculate reflectivity anomalies using attenuation rates of 5.8 dB/km (near MacGregor et al.'s lowest value) and 17.4 dB/km (triple MacGregor et al.'s lowest value and 50% larger than our value). All of our interpreted networks retain 3σ (+19.4 dB) reflectivity anomalies under both extremely high and extremely low attenuation rates, and six of the nine (all the networks except B, F, and H) retain 4σ (+25.9 dB) reflectivity anomalies as well.

2.5.2 Valley-Scale Configuration

The networks are formed from many kilometer-scale water bodies with a variable small-scale morphology. The vast majority of individual water bodies have along-track widths less than the mean ice thickness of 2.5 km. As a whole, the population of Gamburtsev water bodies is smaller than previously published populations, reflecting both a tight grid spacing that allows us to observe small water bodies and rugged basal topography that prevents the formation of large water bodies. The water networks occur within subsections of the dendritic valley networks that dominate the Gamburtsevs, and are between 20 and 103 km long.

The water networks in the Gamburtsevs reoccupy a system of alpine overdeepenings formed by valley glaciers in the early growth phase of the EAIS. The overdeepenings form a series of bedrock depressions along valley floors where water generated by subglacial melt collects. This "string of beads" morphology (*Benn and Evans*, 1998) explains why flight lines that happened to be parallel to the water networks detected a large number of water bodies, whereas flight lines that were oblique to the networks detected few or none at all. We do not observe all the connections between these water bodies, but simple flow-routing algorithms and hydraulic head values between adjacent water bodies (Figures 2.9, 2.10, and 2.11) suggest they exist. In addition, we observe relatively little water in the upper reaches of the main trunk valleys and in the southeast corner of the grid (Figures 2.4, 2.6, and 2.9)

despite thick ice in these regions. The lack of water in these regions may be because downhill flow encourages rapid evacuation and discourages ponding, or because the bed is cold here, and meltwater is not present. A cold bed could be caused by changes in geothermal flux or accumulation rate.

The Gamburtsev water networks transport mass and energy along the bedrock valleys. Where water is generated by basal melt, both mass and latent heat are transferred from the ice sheet to the basal hydrologic system. The mass and heat are transported by the hydrologic networks to freeze-on locations and returned to the ice sheet, though some water may pass through the freeze-on locations. We do not observe water bodies downstream of the freeze-on locations, but because our methods are conservative we cannot preclude the possibility that water passes through the freeze-on locations. The Gamburtsev water networks form an alternate pathway for rapidly transporting mass and energy between widely spaced parts of the ice sheet.

2.5.3 Drainage Pathways

Drainage pathways in the Gamburtsevs are controlled by bed topography, but drainage direction is controlled by the ice sheet surface. The water networks in the Gamburtsevs fall largely on the bed-dominated side of the bed-dominated to surface-dominated continuum of subglacial water networks because they are confined to pre-existing bedrock depressions. However, the valley walls that confine the water to the pre-existing networks are steeper than the valley floors that determine drainage direction within those networks. Valley floor slopes are low enough that drainage direction within the bed-confined networks is determined by the ice sheet surface. The modern subglacial water system occupies the same set of morphological features as the pre-EAIS alpine glacial lake system, but it is free to move water either uphill or downhill through that system.

We term drainage within the Gamburtsevs "bed routed, surface directed", meaning that the flow is confined to pre-existing bedrock valleys but can move either uphill or downhill within those valleys depending on the ice surface slope. This style of subglacial drainage will occur wherever the ice sheet bed contains troughs unrelated to ice flow. The basal topography must be organized into valleys with wall slopes steeper than 11 times the ice surface and floor slopes shallower than 11 times the ice surface. This situation could arise in other areas of East Antarctica with rugged basal topography such as the Recovery Highlands, Ridge B or Dome C, but it could also arise in an area of relatively flat basal topography with valleys, such as interior Greenland (e.g. upstream of Petermann Glacier (*Bamber et al.*, 2013b)[2]) or the beds of the former Laurentide and Fennoscandian ice sheets (*Benn and Evans*, 1998). This situation will not arise in places like the West Antarctic ice streams, where bed troughs are shallow enough that changes in the ice surface can cause water to jump between adjacent troughs resulting in lateral piracy by adjacent ice streams (*Alley et al.*, 1994).

[2]This reference has been changed from the published version. The original reference was to an AGU presentation of our preliminary work on the basal bodies in the Petermann catchment. That presentation included a map of basal topography showing the "Petermann canyon". However, in the time since then a paper has been published specifically on that canyon, so I have modified the reference accordingly.

2.5.4 Possible Temporal Variability

There is indirect evidence for long-term (10's of ka) variability in the Gamburtsev water networks from the along-flow structure of the accretion plumes. The apparent separation (∼20 km) between the end of network B and a nearby accretion plume implies accretion has been inactive there for 20 ka, assuming a characteristic ice velocity of 1 ma^{-1}, although other factors may explain the apparent separation (Section 2.4.4). In addition, the plume produced by network C displays substantial along-flow variability. Morphologically distinct reflectors within this plume can be traced coherently for ∼30 km over multiple flight lines before abruptly disappearing (Figure 2.12), implying a persistence timescale of ∼30 ka. Long term variability in the networks could be produced by surface climate changes propagating to the bed and causing changes in basal thermal state, or by internal dynamics of the ice sheet and hydrologic system.

Short-term variability in the water networks may be caused by changes in drainage morphology. Water networks elsewhere in Antarctica with similar hydraulic gradients to the Gamburtsev networks episodically drain. *Wingham et al.* (2006) discovered active drainage connecting subglacial lakes separated by over 290 km near Dome C in East Antarctica along a hydraulic head gradient of $5.1\text{x}10^{-4}$, in the mid-range of the gradients along the Gamburtsev networks (Table 2.2), and attributed that drainage to sudden discharge through subglacial tunnels. *Fricker et al.* (2007) found episodic drainage between active subglacial lakes underneath Whillans Ice Stream along a hydraulic head gradient of $3 - 6\text{x}10^{-4}$, also in the mid-range of the gradients along the Gamburtsev networks. *Fricker et al.* (2010) found episodic drainage between subglacial lakes underneath MacAyeal Ice Stream along a hydraulic head gradient of $1.7\text{x}10^{-3}$, on the high end of the gradients along the Gamburtsev networks. On the other hand, *Smith et al.* (2009) made a comprehensive inventory of actively filling and draining lakes throughout Antarctica using repeat-track satellite laser altimetry and did not discover any near Dome A. However, the smallest lakes they could detect were 5 km long (*Smith et al.*, 2009, Figure 5), and all but two of the Gamburtsev water bodies are smaller than this. Based on the similar hydraulic gradients of episodically connected networks elsewhere in Antarctica to the Gamburtsev networks, we speculate that the individual water bodies within the Gamburtsev networks are also connected by episodic discharge. A rigorous investigation of the time dependence of the connections within the Gamburtsev water networks will require repeat radar surveys in the future.

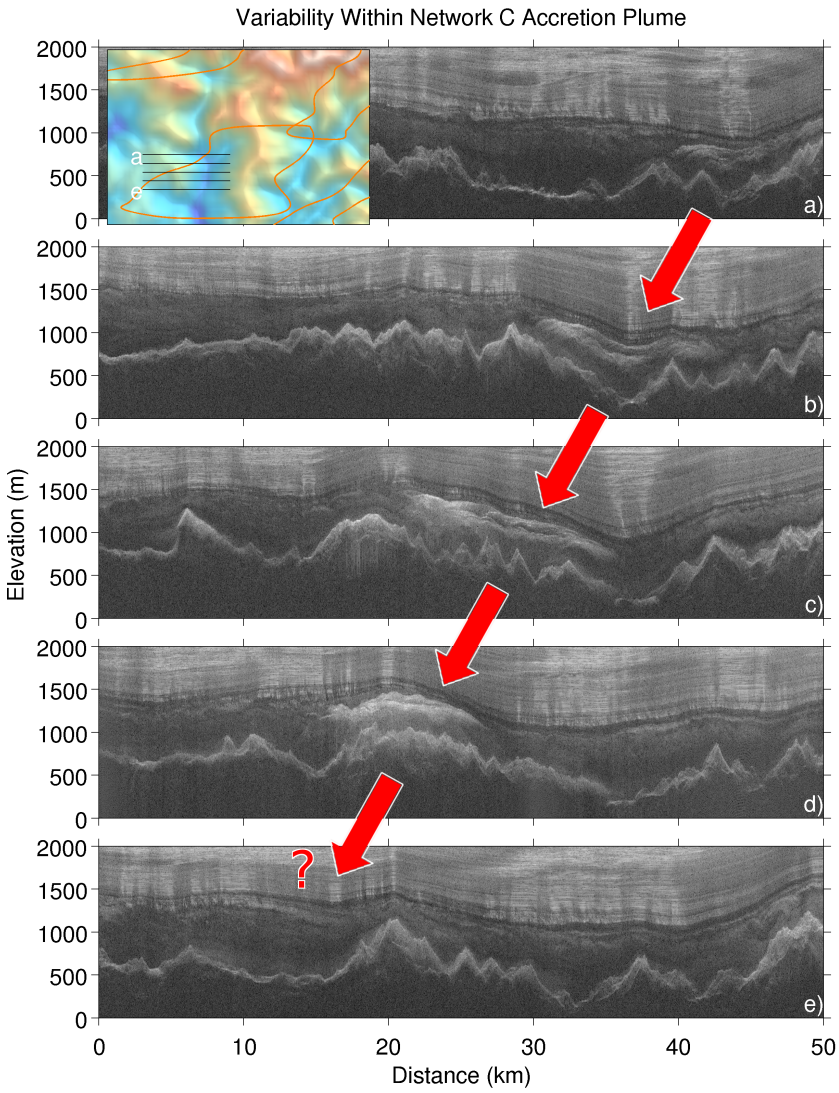

Figure 2.12: Sequential echograms crossing the accretion plume produced by network C. Color scale is the same as Figure 2.3. Red arrows indicate the advection by ice flow of a morphologically distinct accretion unit in first panel through the rest of the figure. This unit can be recognized by having distinct upper and lower surfaces with a radar-transparent layer in the middle. Upstream of this figure the accretion plume has a different morphology, but can still be traced coherently (not shown). Question mark in fifth panel indicates that the accretion unit terminated abruptly somewhere between fourth and fifth panels. Because this is the downflow end of the accretion plume, the termination could represent the time when the accretion process activated in the past. Spacing between flight lines is 5 km. Inset map represents bed elevation with identical color scale and hill shading as Figure 2.4b. Orange lines represent outline of *Bell et al.* (2011) accretion units represented in Figure 2.9. Location of inset map given in Figure 2.9.

2.6 Conclusion

We have identified subglacial water networks with lengths from 20 to 103 km within the Gamburtsev Subglacial Mountains using two methods to analyze radio-echo sounding data. Using both manual digitization and quantitative reflectivity anomaly analysis we have been

able to track the change of the network configuration with distance downflow. These networks are characterized by a complex configuration containing a multitude of kilometer-scale water bodies in a manner similar to subaerial alpine lakes. The individual water bodies are smaller on average than water bodies that have been discovered by previous surveys (*Siegert et al.*, 2005; *Carter et al.*, 2007), reflecting both a tighter line spacing and rugged basal topography that prevents the formation of large water bodies. Based on this result we emphasize the importance of high-resolution surveys for understanding subglacial hydrology. We cannot constrain the timing of the water flow between the individual water bodies in each network, but similarities in hydraulic gradient to other Antarctic water systems suggest drainage may be episodic. In addition, analysis of variability in the accretion plumes produced by some of the networks suggests that the extent of the networks may reflect changes in the basal thermal state caused by either changes in the internal dynamics of the ice sheet and hydrologic system or changes in surface temperature and accumulation.

The water bodies form in depressions created by alpine glaciers during the early growth phase of the East Antarctic Ice Sheet. These depressions are able to trap subglacial water at the present day because of the high bedrock relief in the Gamburtsevs compared to the surface relief. However, bedrock slopes along valley floors are lower than bedrock slopes down valley walls, allowing the ice surface to dictate the direction, but not the route, of subglacial water drainage. Subglacial water within the Gamburtsevs can flow either uphill or downhill along valley floors depending on the gradient of the ice surface. When the networks flow uphill, they feed organized plumes of accretion ice, indicating source to sink transport within the basal hydrologic system. The mountain valleys of the Gamburtsevs are pathways for the transport of mass and energy between widely separated parts of the ice sheet.

We propose that subglacial water exists across a continuum of scales, from tens of kilometer giants like Lake Vostok through sub-meter scale linked cavities. There is no sharp physical threshold separating classic "subglacial lakes" from other forms of subglacial water, only a limit in detectability. In the Gamburtsev water networks, long distance (up to 103 km) transport of mass and energy is accomplished through strings of small ($\sim$850 m) discontinuous individual water bodies. The individual water bodies represent a step by observational glaciology towards bridging the gap between small channels or cavities and large subglacial lakes.

Chapter 3

Traveling slippery patches produce thickness-scale folds in ice sheets

Michael J. Wolovick, Timothy T. Creyts, W. Roger Buck, Robin E. Bell
Published in Geophysical Research Letters, Vol. 41, 2014

3.1 Abstract

Large, complex stratigraphic folds that rise as high as 60% of the local ice thickness have been observed in ice sheets on Antarctica and Greenland. Here we show that ice deformation caused by heterogeneous and time-variable basal sliding can produce the observed structures. We do this using a thermomechanical ice sheet model in which sliding occurs when the base approaches the melting point and slippery patches develop. These slippery patches emerge and travel downstream because of a feedback between ice deformation, vertical flow, and temperature. Our model produces the largest overturned structures, comparable to observations, when the patches move at about the ice column velocity. We conclude that the history of basal slip conditions is recorded in the ice sheet strata. These basal conditions appear to be dynamic and heterogeneous even in the slow-flowing interior regions of large ice sheets.

3.2 Introduction

Ice penetrating radar transects collected over several decades show nearly horizontal reflections in the upper part of the ice sheet indicating layered strata of meteoric ice formed from snowfall (e.g. *Bailey et al.*, 1964). In recent years, the collection of closely spaced transects of high quality aerogeophysical data (*Li et al.*, 2013) has allowed the identification of widespread irregular reflectors in the lower part of the ice sheet (*Bell et al.*, 2011, 2014; *NEEM Community Members*, 2013). These reflectors form structures that do not conform to the bed or surface and that disturb the overlying stratigraphy into anticlines, synclines, and overturned folds (Figure 3.1). These folds normally have older, reflective ice surrounding a core of featureless ice. In some cases reflectors emerge from near the bed. The folds can

be quite large, with thicknesses up to ∼1000 m in ice that is about 2000 m thick, widths of ∼10-20 km, and lengths on the order of 10-100 km (*Bell et al.*, 2014).

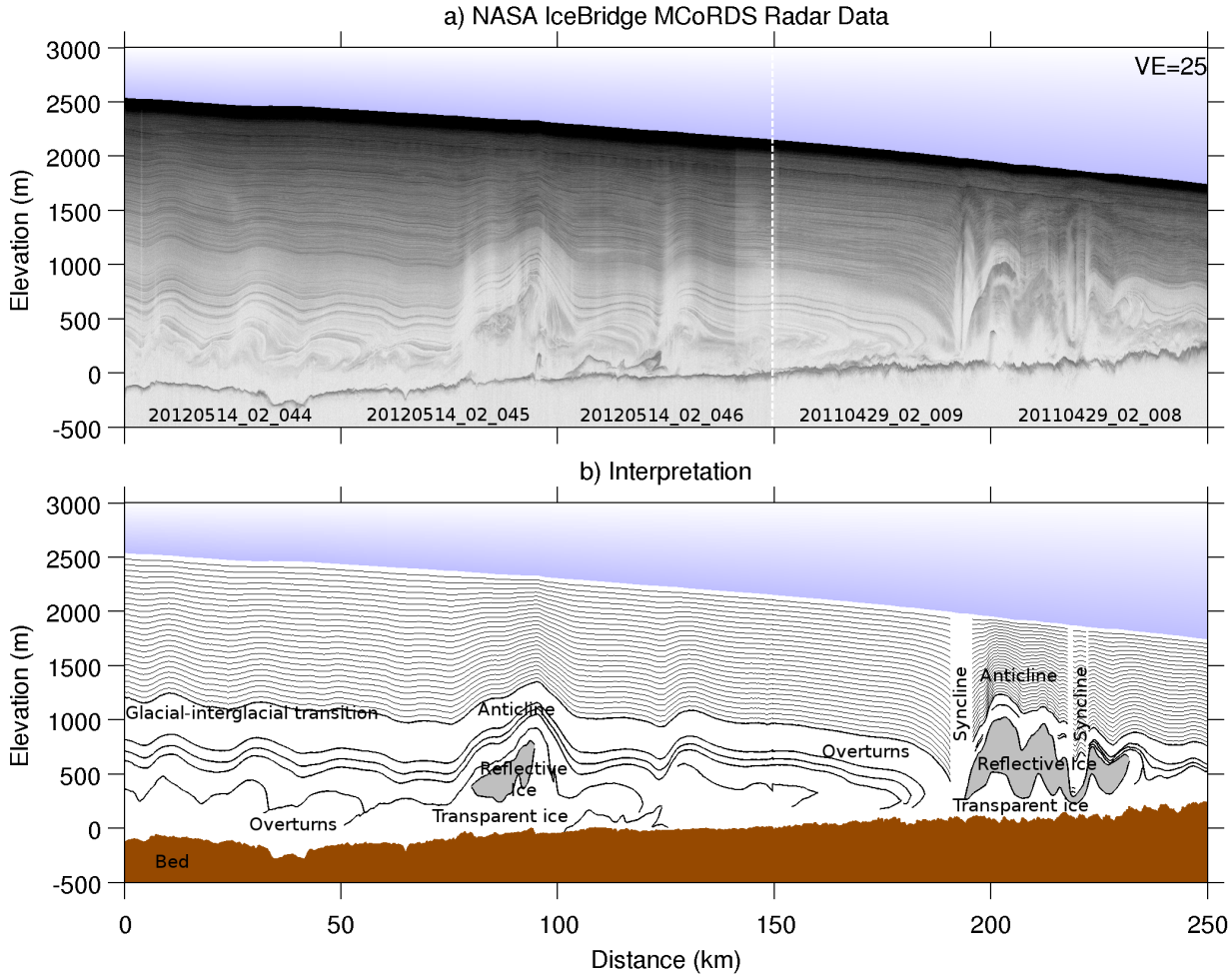

Figure 3.1: Radar image from northern Greenland depicting basal units and associated deformation. Image comes from two separate flight lines stitched together near 150 km. Data are located at ftp://data.cresis.ku.edu/data/rds/, and the identification numbers in Figure 3.1 (top) can be used to locate the data in question. (top) The radar data and (bottom) our interpretation of the data. Vertical exaggeration is 25. Flight line is slightly oblique to flow.

Several hypotheses exist for the formation of these folds. In Antarctica, these features are closely associated with topographically confined water networks (*Wolovick et al.*, 2013), and resemble the refrozen ice sampled and imaged over Lake Vostok (*Jouzel et al.*, 1999; *MacGregor et al.*, 2009a). In the interior of Greenland large-scale folds do not have a clear relationship to basal water networks, although the folds may originate near a warm to cold bedded transition (*Aschwanden et al.*, 2012). Alternately, rheological contrasts within the ice column may create these folded features through a shear instability in the flowing ice (*NEEM Community Members*, 2013). Here we consider the possibility that this folded stratigraphy results from changing basal slip. We show how warm slippery patches at the ice sheet base travel downstream, and that the stratigraphic structures created by traveling slippery

patches can explain many of the radar observations.

Stratigraphy deflects vertically where ice flow crosses areas with different basal slip rates (*Weertman*, 1976). Such gradients in slip rate cause either divergence or convergence of the horizontal flow field near the bed, depending on whether the bed becomes more or less slippery along flow, respectively. To maintain mass balance in the lower part of the ice sheet, there is a vertical flow component that lifts up or draws down the stratigraphy. In some cases, the vertical flow causes vertical motion of the surface (*Sergienko et al.*, 2007). In other cases, deformation with one sign in the lower part of the ice sheet is compensated for by deformation with the opposite sign in the upper portion of the ice sheet, and the surface maintains a steady state (*Hindmarsh et al.*, 2006). The latter case has been observed where ice flowing over Lake Vostok experiences thickening near the bed and thinning near the surface when it regrounds (*Bell et al.*, 2002). However, stationary contrasts in slip rate produce small layer deflections compared with bed topography or surface accumulation, and basal slip rate has been considered a secondary factor in the analysis of ice sheet stratigraphy (*Hindmarsh et al.*, 2006; *Leysinger Vieli et al.*, 2007; *Parrenin and Hindmarsh*, 2007). Here, we consider slippery patches that travel downstream over time and produce a larger integrated deflection of the overlying stratigraphy.

Basal slip rate can change in space or time because of a variety of factors, including basal temperature (*Cuffey et al.*, 2000; *Clarke*, 2005; *Stokes et al.*, 2007), till coverage (*Tulaczyk et al.*, 2000b; *Clarke*, 2005; *Stokes et al.*, 2007), subglacial water pressure (*Creyts and Schoof*, 2009; *Hewitt*, 2013), and till drainage (*Tulaczyk et al.*, 2000b; *Clarke*, 2005; *Stokes et al.*, 2007). While all these factors are capable of moving over time, for simplicity we focus on slip variations caused by basal temperature. We use a thermomechanical model described below to show that basal slippery patches are capable of migrating downstream, and that the resulting dynamic contrasts in slip rate create large and intricate stratigraphic structures.

3.3 Methods

We simulate ice flow using a higher order two-dimensional thermomechanical flowline approach (*Blatter*, 1995; *Pattyn*, 2002; *Cuffey and Paterson*, 2010). Particle tracking allows us to follow englacial stratigraphy and model isochronous layers. A key feature of our model is that it allows for both water flow and longitudinally variable basal boundary conditions while conserving mass and energy at the ice sheet base. Basal temperature is coupled to water flow along the base as follows: temperature is held at the melting point where water is present while a geothermal gradient is prescribed elsewhere. The model can contain multiple warm-based patches, each with an internal mass balance between melting and freezing. Basal slip rate falls off exponentially as basal temperature drops below the melting point (*Fowler*, 1986), consistent with field observations that suggest limited but non-zero basal slip at cold temperatures (*Cuffey et al.*, 2000). Sub-freezing basal slip is due to a combination of pre-melt films at the ice-rock contact (*Cuffey et al.*, 2000) and unresolved thermal heterogeneity at the bed (*Fowler*, 1986); for our purposes it is not necessary to distinguish these mechanisms. The boundary conditions and model setup are shown schematically in Supplementary Figure 5.2 and a more detailed description is given in the supplement. The steady state initial condition is obtained by allowing the model to run unperturbed for 100 ka. We

performed resolution tests on the model and found that the error is inversely proportional to the number of grid cells (Supplemental Figure 3.7).

Our model domain simulates a thick interior region with a warm base that transitions downstream into a thinner, cold-based region (Supplementary Figure 5.2). This setting was chosen to mimic conditions that may exist upstream of Petermann Glacier and in the flanks of the Northeast Greenland Ice Stream (*Aschwanden et al.*, 2012), where many large folds are observed (*Bell et al.*, 2014). Water flows along the smooth base from the warm interior region toward the cold downstream area.

3.4 Results

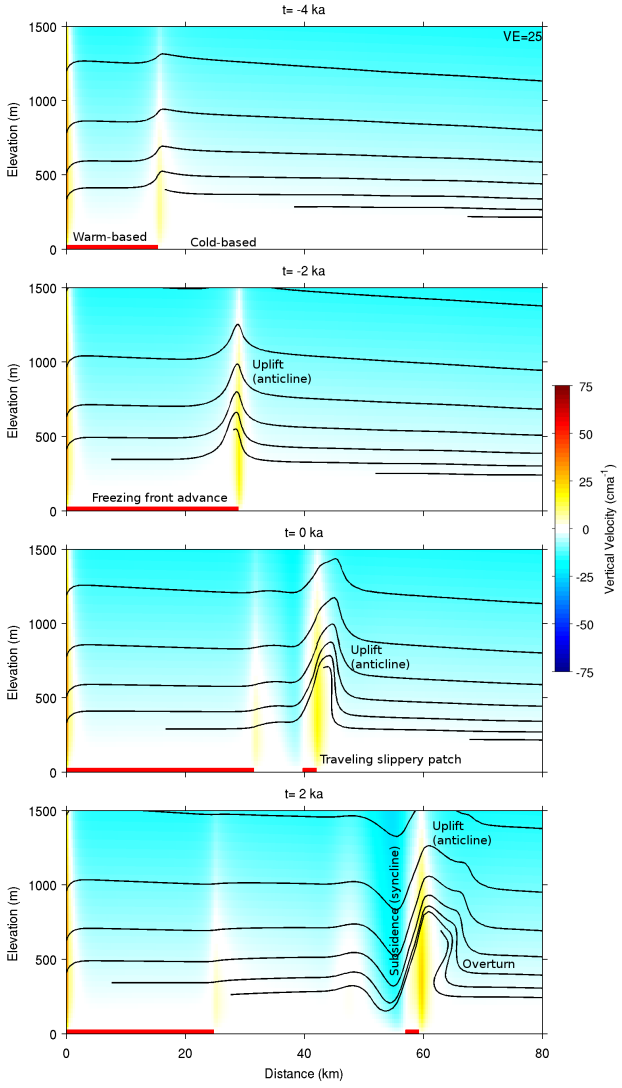

Figure 3.2: Close-up of the initial triggering of a traveling slippery patch. Plots represent four snapshots of model output, taken 2ka apart. Time is measured relative to the peak in the water influx perturbation. Color represents vertical velocity, lines represent stratigraphy. Red bars on the bottom of the plots represent areas where the bed is at the melting point.

When we perturb the upstream water flux, a warm slippery patch forms and travels downstream. At the leading edge of the slippery patch, a freezing front marks the boundary between an upstream, warm-based, water-rich, rapidly sliding patch and a downstream, frozen, slowly sliding region. We find that the perturbation must be sufficient to cause the freezing front to move downstream at approximately the column-average ice velocity in order to trigger a traveling slippery patch. The perturbation we used is equivalent to an increase in melt rate of only 0.05 mm/yr over the course of about 5000 years, assuming a cross-flow width of 10 km and an upstream catchment of 10^4 km^2. This increase is small compared to geothermal melt rates, that are about 1 mm/yr.

The position of the freezing front is determined by a balance between the water flux and the freezing rate. As the upstream water flux increases, the freezing front advances downstream as latent heat is released. Near the freezing front, basal slip rate drops and produces ice convergence that results in englacial uplift (Figure 3.2a,b). This uplift moves warm ice higher into the ice sheet, reducing the local temperature gradient. Eventually the conductive heat flux out of the basal interface does not match the geothermal heating and frictional heating from sliding, creating a local melt source just upstream of the freezing front. Once the uplift at the freezing front allows local melt, the slippery patch is no longer limited by the mass balance of the upstream water system. The patch detaches from the upstream water system and travels downstream without further forcing (Figure 3.2c,d).

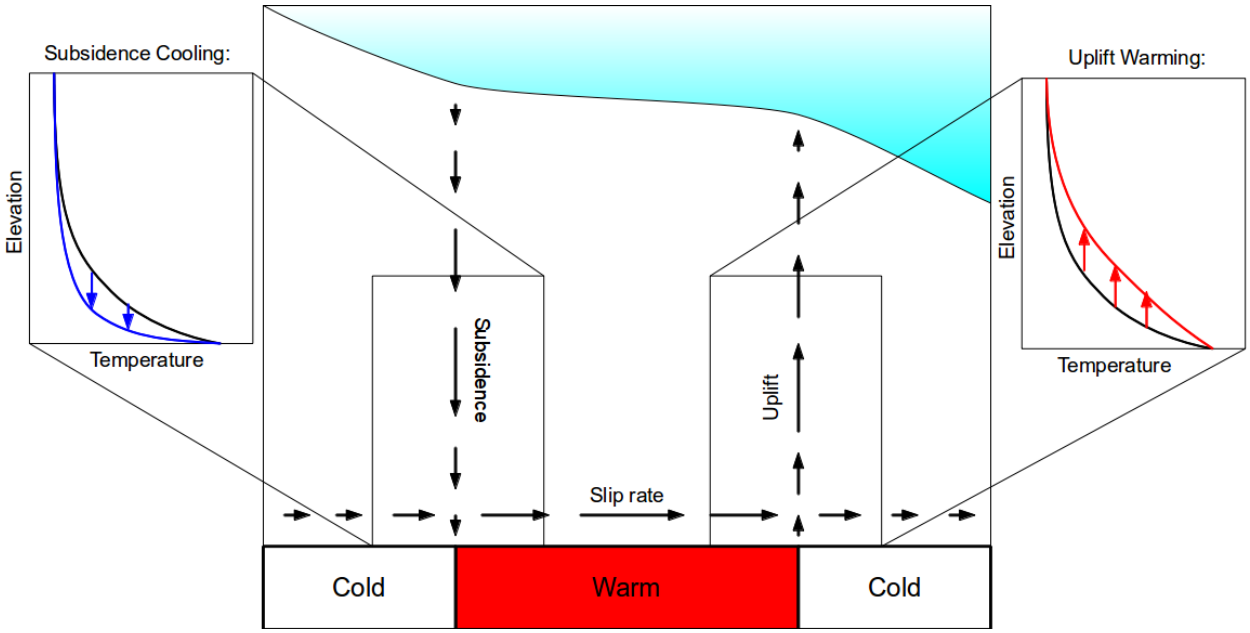

Figure 3.3: Schematic representation of the thermal feedback that causes slippery patches to move downstream. Englacial uplift at the front (downstream) edge of the patch produces advective warming of the ice column, while subsidence at the back (upstream) edge of the patch produces advective cooling. Inset temperature profiles are meant to be representative of the changes that take place at the margins of the slippery patch. Black lines in the inset represent background temperature profiles, red and blue lines represent changes due to uplift or subsidence, respectively.

The main part of a slippery patch is composed of a broad melting region that supplies water to a narrow but intense freezing region near the front (Supplementary Figure 3.6).

Water is assumed to flow downstream throughout the patch due to the gradient in ice overburden pressure. Lower temperatures behind (upstream of) the slippery patch reduce basal slip rate, leading to divergence in the bottom of the ice sheet. This divergence pulls cold ice downward, increasing the conductive heat loss across the basal interface and cooling

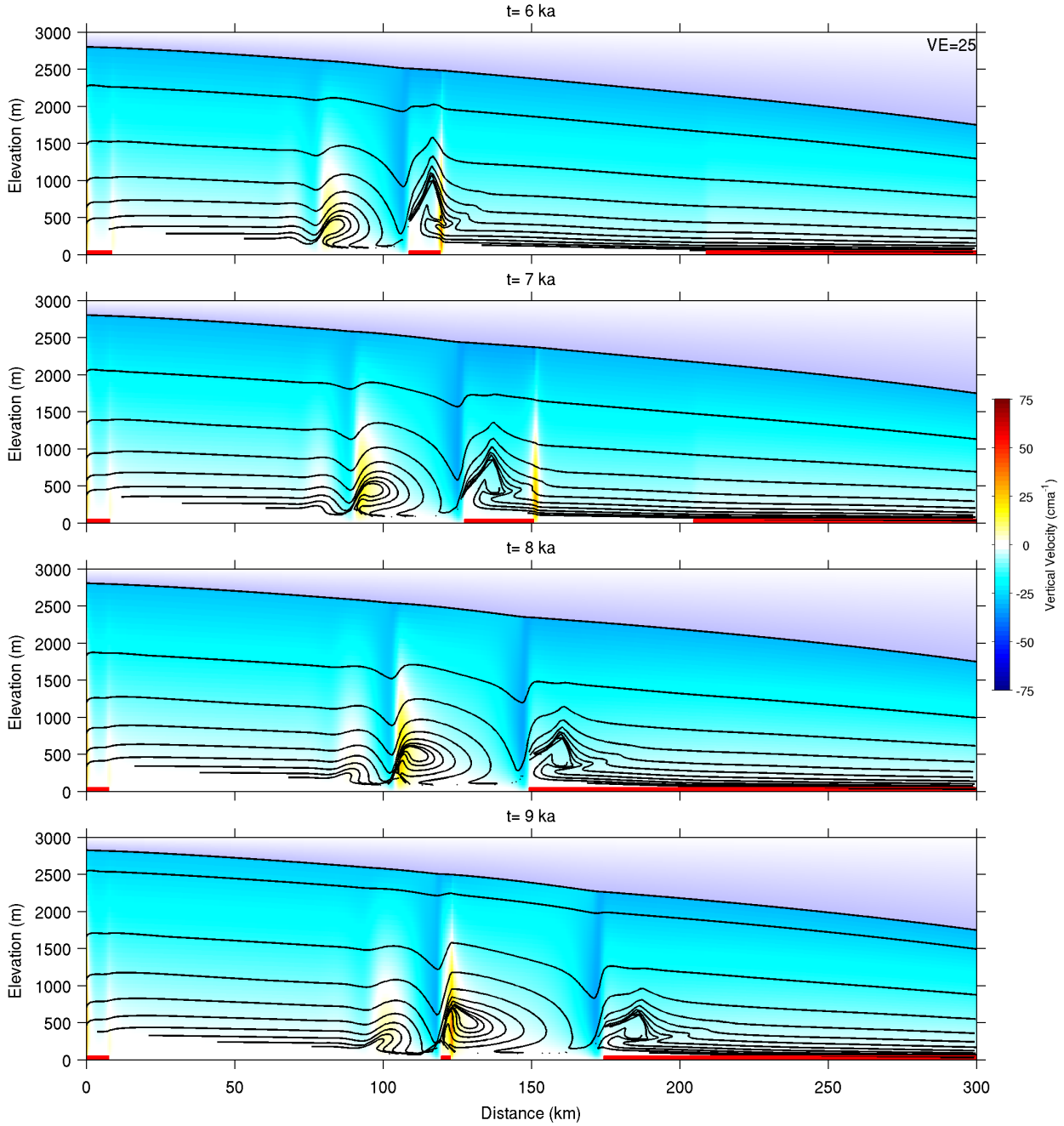

Figure 3.4: Snapshots of the entire model domain showing the development of a mature train of traveling slippery patches. Four snapshots are separated by 1ka each. Time is measured relative to the peak in the water influx perturbation. Color represents vertical velocity, lines represent stratigraphy. Red bars on the bottom of the plots represent areas where the bed is at the melting point.

it below the melting point. Because water is driven downstream, freeze-on does not occur at the back of the patch. The combination of cooling at the back (upstream) and warming at the front (downstream) causes the entire slippery patch to propagate downstream (Figure 3.3). Previous work has shown that perturbations to basal slip modify ice sheet thermal structure (*Sergienko and Hulbe*, 2011). Our model shows that closing the feedback loop from thermal structure back to slip can cause the slip perturbation to move. The front of a slippery patch propagates faster than the back because latent heat carried forward by basal water is transported faster than the ice flows. The difference in propagation speed causes the patch to grow over time.

A secondary patch can be generated as a consequence of the subsidence and cooling behind an initial slippery patch. Subsidence immediately behind the slippery patch causes cooling relative to the temperature far upstream. This subsidence produces a basal slip rate contrast upstream of the initial slippery patch, leading to convergence and uplift there. Eventually the upstream convergence warms to the melting point, creating a new, trailing slippery patch (Figure 3.4d). Over time this sequence repeats, creating a train of patches and deformation.

Patches in a train can combine when the fast-moving front of one patch overtakes the slow-moving back of the next one. Basal temperatures in the intervening cold region rise to the melting point. As temperatures rise, drag drops, and the entire ice sheet domain responds with faster flow and surface lowering. The speed-ups can produce 20-50% increases in ice flux with an overall duration on the order of 1000 a. These flux increases can have rapid onsets ($\sim$100 a) when the slippery patches merge.

3.5 Discussion

Our results show that traveling slippery patches can produce both significant uplift and subsidence within ice sheets. The model produces folds (Figure 3.4) that are similar to the deformed and overturned ice stratigraphy observed in Greenland (*NEEM Community Members*, 2013; *Bell et al.*, 2014) and Antarctica (*Bell et al.*, 2011). The largest observed structures rise to over half the ice thickness. The model produces both anticlines and synclines, mimicking the structures observed in the radar data (Figure 3.4, cf. Figure 3.1). The model structures are much larger than equivalent ones produced by stationary patches (Supplemental Figures 3.8, 3.9). The model predicts overturning within the cores of the uplifted folds, whereas radar data show no reflections within the cores (*Bell et al.*, 2014). The lack of observed features in the cores may be because of data limitations, such as difficulty in imaging contorted layers, or because of processes not included in the model, such as dynamic recrystallization (*Cuffey and Paterson*, 2010). Additional work is required to understand how traveling slippery patches will behave in a complex 3D environment, and how the patches might be modified by bed topography and heterogeneous subglacial geology.

Other proposed mechanisms that can contribute to the deformed and overturned ice stratigraphy include basal freeze-on (*Bell et al.*, 2011) and rheological contrasts within the ice column (*NEEM Community Members*, 2013). A combination of mechanisms likely operates to produce the observed basal structures. For example, our modeled traveling slippery patches contain a small amount (10's of meters) of freeze-on ice. Melting and freezing in

our model is limited to low volumes because of latent heat constraints and our choice of boundary conditions. Nevertheless, traveling slippery patches amplify the size of englacial structures beyond the volume of the freeze-on ice alone. Our model includes only variations in ice rheology caused by temperature, but other variations, such as crystal size and fabric (*Cuffey and Paterson*, 2010; *NEEM Community Members*, 2013), could be compatible with our proposed mechanism.

Our model produces substantial variations in ice column temperature, and thus, rheology. Vertical flow pushes warm ice upwards at the front of the traveling slippery patches and pulls cold ice downwards at the back of the patches. This advection modifies the ice column temperature, creating a heterogeneous distribution of warm, soft areas and cold, stiff areas (Supplementary Figure 3.6).

Vertical motion associated with traveling slippery patches can uplift basal ice to about 50% of the ice thickness. The process moves basal debris and deep ice upwards. Uplift of debris from ice near the bed (*Lawson et al.*, 1998; *Rempel*, 2008) could delay debris melt-out, including melt-out after iceberg calving. This would aid in the transportation of ice-rafted debris long distances during Heinrich Events (*Hemming*, 2004). Additionally, recovery of old ice normally found near the bed (*Fischer et al.*, 2013) may be easier when that ice is uplifted. However, repeated sections and age inversions may complicate ice core interpretation (*NEEM Community Members*, 2013). Such complications could have produced the overturned and repeated sections observed in the NEEM core (*NEEM Community Members*, 2013) and potentially played a role in creating the difference between the GISP2 and GRIP cores near Summit, Greenland (*Grootes et al.*, 1993).

Our model makes several predictions about the relationship between the structures in radar echograms and observations that could be made in boreholes. We predict that the majority of the large basal units will have the gas content and geochemical signature of meteoric ice, rather than that of refrozen ice (*Souchez et al.*, 2003), and will be highly deformed, with age inversions and repeated sections. If the structures are active, we also predict that synclines mark boundaries in basal thermal conditions, with cold beds upstream and warm beds downstream. This prediction contrasts with the typical assumption that layer drawdown marks the location of concentrated basal melt driven by extreme geothermal heat fluxes (*Fahnestock et al.*, 2001). However, once the structures become inactive and are passively advected with the flowing ice, they no longer represent variations in basal conditions.

According to our model, stratigraphy responds strongly to moving variations in basal slip. Inversions of basal slip (*MacAyeal*, 1993) from remote observations of surface velocity and ice sheet geometry show heterogeneity in both Greenland (*Sergienko et al.*, 2014) and Antarctica (*Sergienko and Hindmarsh*, 2013), but the temporal variability is poorly constrained. Critical factors for basal slip, such as water availability, sediment coverage and strength, and basal temperature, are difficult to observe directly, but radar stratigraphy can be observed relatively easily. Ice sheet interiors likely have heterogeneous and time-varying basal conditions that leave a record in the ice sheet stratigraphy. Thus, the history of subglacial slip may be estimated from analysis of englacial structures.

This history can include perturbations to basal water flux that trigger the traveling slippery patches. Basal water flux perturbations can be caused by changes in the basal thermal regime or changes in subglacial water routing. Either of these can be related to

rapid changes in surface temperature and accumulation rate, or ice thickness changes that propagate inland from the margins. These are often related to rapid climate change. We speculate that some of the features observed today in Greenland could have been triggered by sudden climate changes that occurred during deglaciation following the Last Glacial Maximum.

3.6 Conclusion

Moving patches of subglacial slip create large stratigraphic folds within polar ice sheets as shown in the thermomechanical model used here. These folds create large disturbances to ice sheet thermal structure that feed back to basal temperature and cause the slip patch to migrate. Traveling slippery patches can explain some of the dramatic recent observations of large basal units in Greenland and Antarctica. Our results show that massive thickness-scale folds in ice sheets can be explained with only small amounts of freeze-on. Borehole measurements of ice provenance within the basal units could be used to confirm or disprove our hypothesis. Englacial structures created by traveling slip patches record basal processes and can be used to infer a time-variable history of basal slip. The wide variety of behaviors in ice sheet interiors, including traveling slip patches, suggest that ice sheet interiors can play a critical role expanding our knowledge of ice dynamics and discharge to the margins.

3.7 Supplemental Material

This text was published in the supporting online material for chapter 2, and can be accessed along with the main text at:

http://onlinelibrary.wiley.com/doi/10.1002/2014GL062248/abstract

A supplemental animation showing 30 ka of model output can also be viewed at that site.

3.7.1 Thermomechanical Flowline Model with Basal Hydrology

We consider a two-dimensional flowline with coordinates x, positive along flow, and z, positive upwards. The velocity components are u and w, with the same sign convention. Stresses in the vertical dimension are assumed to be hydrostatic. The equations for the conservation of mass, energy, and the horizontal linear momentum are (*Blatter*, 1995; *Pattyn*, 2002; *Cuffey and Paterson*, 2010), respectively,

$$\frac{\partial u}{\partial x} + \frac{\partial w}{\partial z} = 0, \tag{3.1}$$

$$\rho_i c_p \left(\frac{\partial T}{\partial t} + u\frac{\partial T}{\partial x} + w\frac{\partial T}{\partial z} \right) = k\nabla^2 T + \dot{\epsilon} \cdot \sigma, \text{and} \tag{3.2}$$

$$\frac{\partial \sigma_{xx}}{\partial x} + \frac{\partial \sigma_{xz}}{\partial z} = -\rho_i g \frac{\partial S}{\partial x}, \tag{3.3}$$

where ρ_i is the density of ice, c_p is the specific heat at constant pressure of ice, T is temperature, k is thermal conductivity, $\dot{\epsilon}$ is the strain rate tensor, σ is the deviatoric stress tensor,

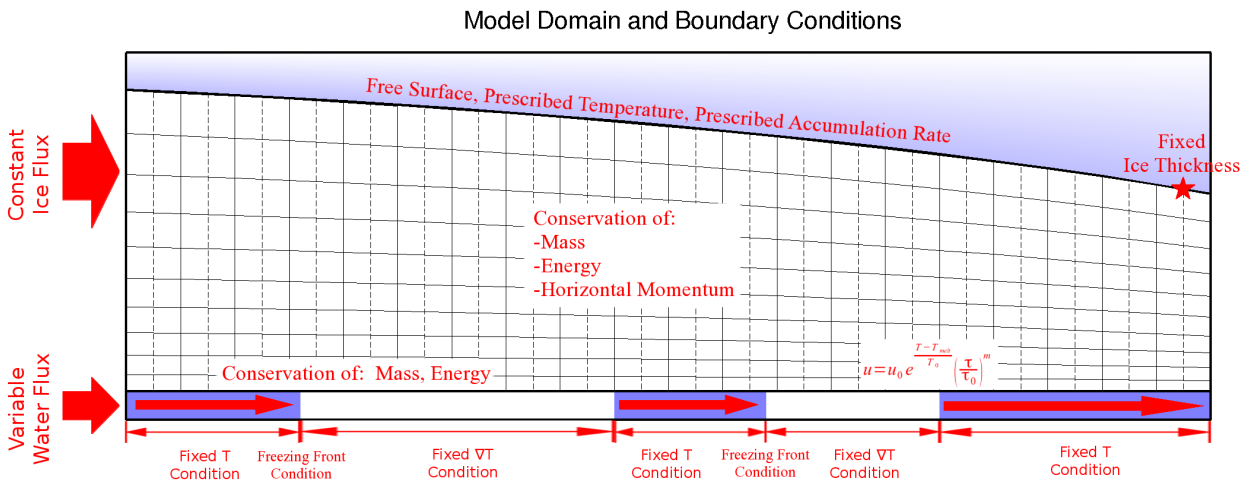

Figure 3.5: Diagram depicting model domain, grid, and boundary conditions. Solid lines represent mass and energy conservation grid cells, dashed lines represent momentum conservation grid cells.

g is the acceleration due to gravity, and S is surface elevation. Ice is assumed to deform with a Glen-type flow law with index n=3 (*Glen*, 1953; *Cuffey and Paterson*, 2010) and a temperature-dependent rate factor,

$$\sigma_{ij} = 2\mu\dot{\epsilon}_{ij}, \tag{3.4}$$

$$\mu = 0.5A^{-1/n}\dot{\epsilon}^{(1-n)/n}, \text{and} \tag{3.5}$$

$$A = A_0 exp\left[\frac{-Q}{R}\left(\frac{1}{T} - \frac{1}{T_0}\right)\right], \tag{3.6}$$

where μ is the effective viscosity, A is the rate factor, A_0 is the value of the rate factor at the reference temperature T_0, Q is the activation energy, and R is the universal gas constant. The value of the activation energy for creep increases with a step function above $T_0 = -10°C$ (*Cuffey and Paterson*, 2010). All temperatures in the above equation are corrected for the pressure dependence of the melting point (*Pattyn*, 2002). Vertical velocity is obtained by integrating equation 3.1 upwards from the bed, starting with a boundary condition given by the basal melt rate. The above equations are solved using a finite-difference approximation on a transformed coordinate system that follows the surface and the bed (*Blatter*, 1995; *Pattyn*, 2002). The momentum conservation equation is solved on a staggered grid relative to the mass and energy conservation equations (Figure 5.2) (*Gerya*, 2010).

The mass conservation boundary conditions are an imposed influx ($10^4\ m^2/yr$, equivalent to a column-average velocity of about 3 m/yr) on the upstream margin of the domain, a variable melt/freeze rate on the base of the domain, a constant accumulation rate (30 cm/yr) at the top of the domain, and fixed ice thickness (1750 m) on the downstream margin of the domain. The boundary conditions for energy conservation are steady-state one-dimensional temperature profiles on the lateral margins of the domain, and an elevation-dependent surface temperature (between -25 $°C$ and about -32 $°C$, with a lapse rate of 7 $°C$/km) on the top of the domain. At the base, temperature gradient is imposed in areas where water is not

present (geothermal flux = 50 mW/m^2), and temperature is held at the pressure-melting point in areas where water is present. The boundary conditions for momentum conservation are free surface on the top of the domain and a temperature dependent power-law sliding rule on the base of the domain. At the lateral margins the momentum boundary conditions are chosen so as to be consistent with the mass boundary conditions. At the upstream boundary the same imposed inflow profile is used as was used for mass conservation, while at the downstream boundary a fixed ice thickness is maintained by a prescribed vertical strain rate profile that compensates surface accumulation and basal melting. We write the temperature dependent sliding rule,

$$u_b = u_0 exp\left(\frac{T_b - T_m}{T_s}\right)\left(\frac{\tau_b}{\tau_0}\right)^r, \tag{3.7}$$

where u_b is sliding velocity, u_0 is a reference velocity, T_b is basal temperature, T_m is the pressure-dependent melting temperature, T_0 is the temperature dependence of sliding, τ_b is the basal shear stress, τ_0 is a reference stress, and r is the sliding index.

We choose a treatment of basal hydrology that is computationally efficient and thus suitable for long model integrations. We assume the hydrologic system is in steady state with the thermal forcing imposed by the ice sheet during any given time step, based on the assumption that the basal hydrologic system operates on much faster timescales than the overlaying ice sheet. Water is assumed to flow down potential within the flowline, so that the equations of mass and energy conservation within the water layer are, respectively,

$$\frac{\partial W}{\partial x} = \frac{\rho_i}{\rho_w} m, \text{and} \tag{3.8}$$

$$G - \rho_i L m + k\frac{\partial T}{\partial z} + u_b \tau_b + W\left(\rho_w c_p \beta \frac{\partial P}{\partial x} - \frac{\partial \Phi}{\partial x}\right) = 0, \tag{3.9}$$

where W is water flux, ρ_w is the density of water, m is the melt rate expressed in terms of ice, G is the geothermal flux, L is the latent heat of fusion, c_p is the specific heat at constant pressure of water, β is the pressure dependence of the melting point, P is pressure, and Φ is hydraulic potential. Equation 3.9 includes the effects of geothermal flux, latent heat, conductive cooling into the ice, shear heating, sensible heat flux associated with a change in the pressure melting point, and viscous dissipation within the water layer. Hydrostatic pressure and hydraulic potential are given by, respectively:

$$P = \rho_i g D, \text{and} \tag{3.10}$$

$$\Phi = \rho_i g D + \rho_w g B, \tag{3.11}$$

where D is ice thickness and B is bedrock elevation. Water flux is obtained by integrating the melt rate from the upstream margin of the domain to the downstream margin, with the additional constraint that water flux must always be positive. The water flux at the upstream boundary is constant (10 m^2/yr) during the spin-up period, then a Gaussian perturbation is added to the water flux at the beginning of the experimental period (amplitude = 50 m^2/yr, standard deviation = 2.5 kyr). The solution procedure is to integrate downstream through

the basal grid cells. Within any given grid cell, two possible melt rates are calculated, one limited by the basal energy budget and one limited by the basal water budget. The larger (more positive) of these melt rates is used to integrate the water flux into the next grid cell. The more positive value is chosen because the basal water budget can only be the limiting factor if there is insufficient water supply to allow for the energy-limited freezing rate. If the water flux is not completely used up by freezing, the basal temperature is set to the pressure-melting point. If all the water flux is used up, the basal temperature is set to a value that closes the energy budget by balancing the conductive heat flux against the other terms in equation 3.9. This allows both mass and energy to be conserved in the basal hydrologic system, even at freezing fronts, but at the price of violating the condition that liquid water cannot exist below the pressure-melting point. In the model, the leading grid cell (farthest downstream) in a freezing front contains both water and freeze-on despite the fact that its temperature is below the melting point. However, the "front condition" is only one grid cell wide, so it vanishes in the limit that the grid size approaches zero. Generalizing this solution procedure to a three-dimensional ice sheet model with a two dimensional bed would require integrating water flux downhill in the hydraulic potential in a similar manner to balance flux calculations that integrate downhill in the ice surface (*Budd and Warner*, 1996).

3.7.2 Additional Model Output

The attached movie shows the output of the model starting 10 ka before the peak of the Gaussian hydrologic forcing and ending 20 ka afterwards. The model spin-up begins 90 ka before the start of the movie and is not shown. The movie advances at 25 year increments. Top panel shows englacial stratigraphy overlain on vertical ice velocity. Bottom panel shows basal temperature as a green line, sliding ratio as a black line, and melt/freeze rate as red/blue patches. The movie is available under the "Supporting Information" tab at:

http://onlinelibrary.wiley.com/doi/10.1002/2014GL062248/abstract

Figure 3.6 shows a variety of model output fields at a single snapshot in time corresponding to Figure 3.4b in the main text.

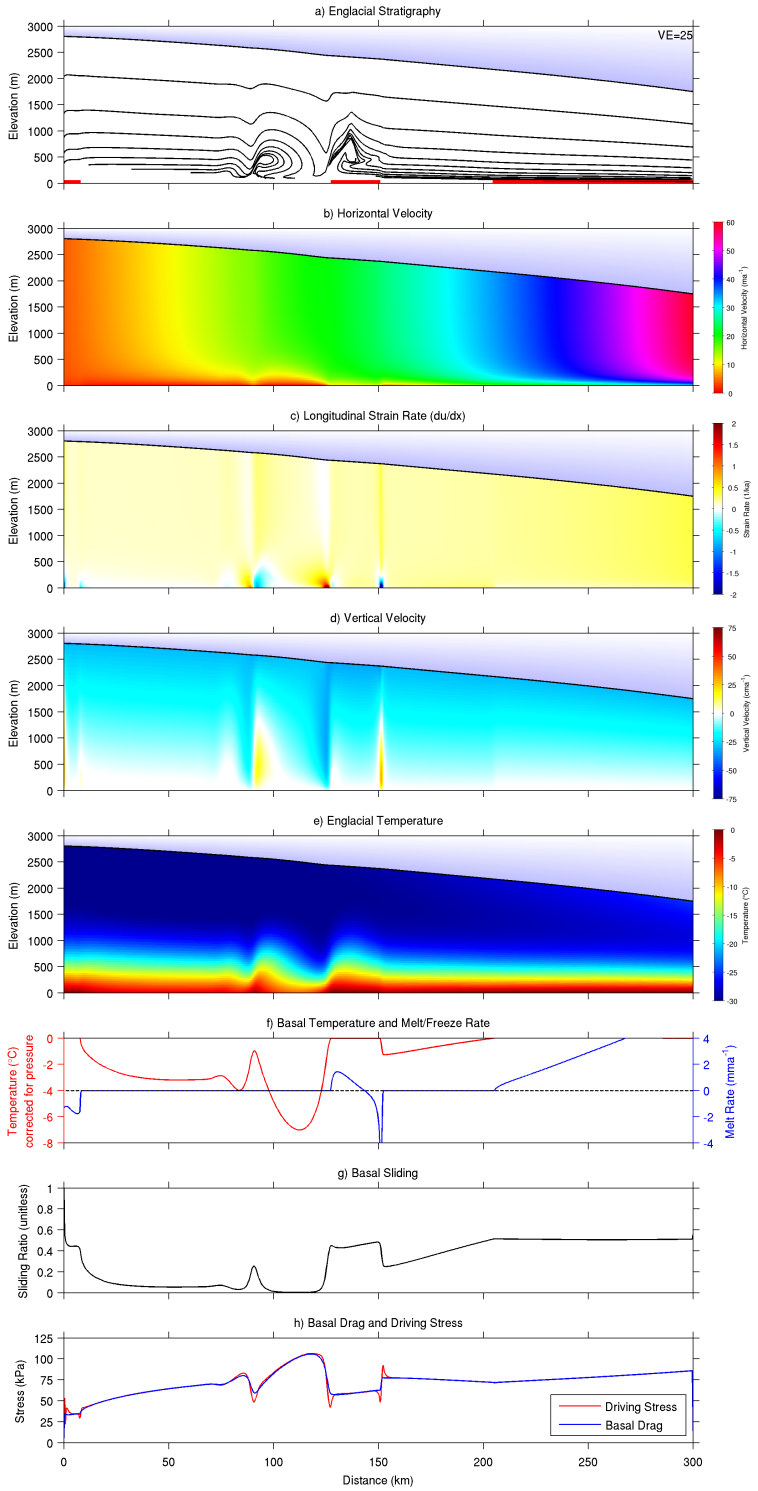

Figure 3.6: Snapshot of key model fields at 7ka (Figure 3.4b in the main text). From top: stratigraphy, with red bars denoting warm-based conditions; horizontal velocity; longitudinal strain rate (positive for divergence, negative for convergence); vertical velocity; englacial temperature (corrected for the pressure dependence of the melting point); basal temperature and melt rate (temperature in red, melt rate in blue); basal sliding ratio, defined as the ratio of sliding velocity to column-average velocity; and finally basal drag and surface driving stress.

3.7.3 Model Tests

We performed two tests of the accuracy of our numerical model relative to known analytic solutions. The first test considered the steady-state temperature solution for constant vertical strain rate. The second test examined the stratigraphic amplitude as a function of depth for a stationary slip contrast. In addition, we repeated the stratigraphic test for the case of a moving slip contrast to demonstrate that moving contrasts are capable of producing larger stratigraphic structures than the steady-state limit.

The temperature test uses the error function temperature solution that applies in steady state to an ice sheet with constant vertical strain rate (*Clarke et al.*, 1977). Assuming steady state, constant vertical strain rate, negligible horizontal gradients, and basal temperature below the melting point, the ice sheet temperature can be written as,

$$T = T_{surf} + \frac{GD}{k} \int_{\hat{z}}^{1} exp(-0.5 P_e \hat{z}^2) d\hat{z}, \tag{3.12}$$

where the over-hat on z indicates elevation normalized by the ice thickness, T_{surf} is the surface temperature, P_e is the Peclet number, defined by $P_e = aD/\kappa$, where a is the surface accumulation rate and κ is the thermal diffusivity, defined by $\kappa = k/\rho_i c_p$. We set up the test by prescribing a plug-flow horizontal velocity field to ensure a constant vertical strain rate and constant ice thickness of 2000 m. The horizontal velocity increased linearly to compensate the surface accumulation rate. We then allowed the thermal model to evolve for 100 ka to approximate a steady state and evaluated the temperature field at x=250 km to compare with the analytic solution. We chose this point to get away from the influence of horizontal advection from the upstream boundary without entering the conductive boundary layer near the downstream boundary.

The numerical approximation tracks the analytical solution very closely (Figure 3.7a). The root-mean-square (RMS) error is $0.044°C$ at the vertical resolution used in this paper. There is a systematic pattern in the error with lower temperatures near the bed and higher temperatures in the middle of the ice sheet (Figure 3.7b). This pattern persists when we varied the vertical resolution. We varied the vertical resolution by a factor of 4 above and below the value used in the paper, and found that the error is inversely proportional to the number of vertical grid cells (Figure 3.7c).

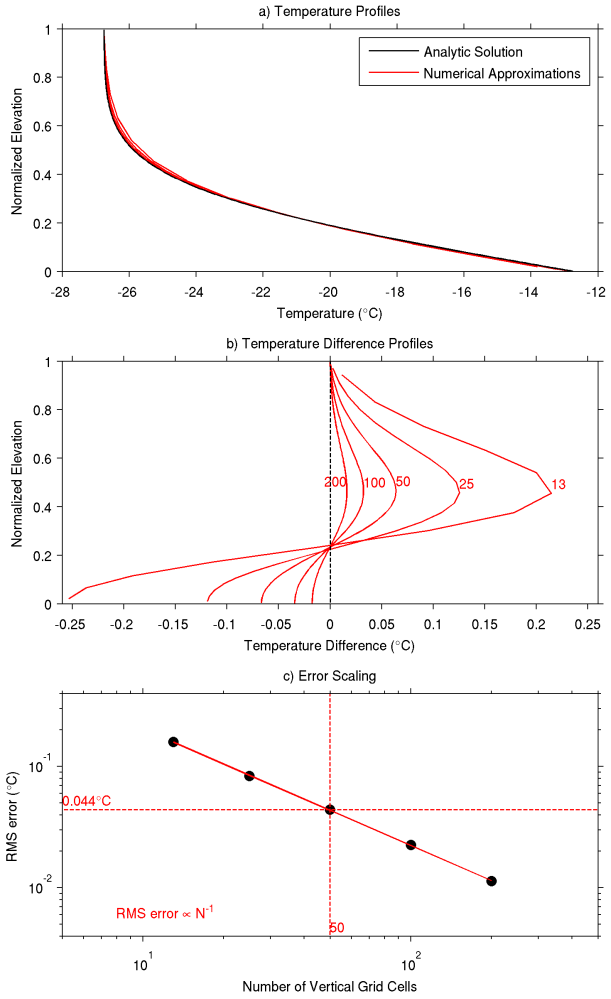

Figure 3.7: Thermal test. We tested the model against the steady-state solution for simplified conditions at a variety of grid sizes. Top plot shows all temperature profiles overlain on the analytic solution. Middle plot shows the difference between the modeled profiles and the analytic profile. Numbers next to each curve indicate the number of vertical grid cells in that model run. Bottom plot shows how the error scales with the number of grid cells. Solid diagonal line indicates best-fit power-law and dashed lines indicate resolution and error at which the model presented in the main body of the paper was run.

We tested the stratigraphy tracking aspect of our model using an analytic solution for a stationary slip contrast, then against a prescribed traveling contrast. The traveling contrast produced much larger stratigraphic structures than the steady-state limit for a stationary contrast. Our model stratigraphy roughly tracked the analytic solution for the stationary contrast, although there are complications related to the finite amplitude displacement of tracers through a variable velocity field and the inclusion of surface accumulation[1].

[1]To clarify: the analytic approximation is obtained by assuming that the vertical velocity is constant over the trajectory of the tracer and by assuming that surface accumulation is zero. However, vertical velocity varies with elevation within the ice column. Tracers in the upper two-thirds of the ice sheet are advected upwards into a weaker velocity field, producing a stratigraphic amplitude less than the analytic approximation in the upper two-thirds of Figure 3.9a. Tracers in the lower third of the ice column are advected upwards into a stronger velocity field, producing a stratigraphic amplitude higher than the analytic approximation.

For a stationary contrast in basal slip, we can specify a closed-form expression for the vertical velocity within the ice sheet (*Leysinger Vieli et al.*, 2007). We parameterize ice sheet flow in terms of a sliding fraction, $F = u_b/\bar{u}$, that defines the ratio of sliding velocity to the column-average velocity. Assuming an isothermal ice sheet, the horizontal velocity can be specified as the linear sum of plug flow and internal deformation, with the sliding fraction giving the relative weighting of these two components. Under these assumptions, and neglecting surface accumulation, the dimensionless vertical velocity can be written as,

$$\hat{w} = -\frac{\partial F}{\partial \hat{x}} \frac{1}{n+1} \left(1 - \hat{z} - (1-\hat{z})^{n+2}\right), \tag{3.13}$$

where the over-hat on w indicates velocity normalized by the column-average horizontal velocity and the over-hat on x indicates distance normalized by the ice thickness. If we assume that F drops linearly from 1 to 0 over a finite distance, and that both components of velocity do not change as a layer travels through the slip transition, then the vertical displacement can be written as,

$$\hat{d} = \frac{1}{n+1} \left(1 - \hat{z} - (1-\hat{z})^{n+2}\right), \tag{3.14}$$

where d represents vertical layer displacement and the over-hat represents displacement normalized by the ice thickness. Equation 3.14 represents a first approximation to a solution for layer displacement as a function of depth for a stationary slip contrast.

To test our stratigraphy model, we set up a run with a flat ice surface at 2000 m and column-average velocity that increases in balance with surface accumulation. We specified the vertical distribution of velocity via a shape function, with plug flow in an upstream sliding region and deformation flow (n=3) in a downstream sticky region. The transition between the two was a linear ramp fixed at x=50 km and 2 km wide (ie, one ice thickness). We allowed the model to run for 10 ka and then recorded the layers between 10 ka and 15 ka. We then repeated the test specifing that the transition would travel downstream at 25 m/yr beginning at 10 ka. As the transition travels downstream at a constant rate it passes through an ice sheet whose column-average velocity is continuously increasing in balance with surface accumulation, allowing us to sample a range of parameter space in normalized velocity (transition velocity divided by column-average velocity).

The steady state stratigraphy for a stationary slip contrast roughly follows the analytic approximation. Layer geometry is a simple linear step-up (Figure 3.8a). The profile of layer amplitude as a function of elevation is mostly bounded by the analytic approximation (Figure 3.9a). However, the analytic approximation assumes that neither velocity component changes over the trajectory of the layer. This assumption breaks down when layer displacement is large relative to the gradient in vertical velocity. Layers near the bed are advected upwards towards higher vertical velocities, resulting in numeric amplitudes larger than the analytic approximation near the bed (Figure 3.9a); conversely, layers near the surface are advected upwards towards lower vertical velocities, resulting in lower amplitude than the analytic approximation (Figure 3.9a). When the transition travels downstream, the stratigraphic amplitude is much larger than the steady-state solution (Figure 3.9b). The exact amplitude

Finally, the maximum amplitude is less than the analytic maximum because non-zero surface accumulation produces vertical thinning within the ice column.

and shape is influenced by inherited structures produced as the transition travels (Figure 3.8b-d), but in general stratigraphic amplitude peaks when the transition moves at the column-average ice velocity (Figure 3.9b).

3.7.4 Symbols Used

3.7.5 Detail of Large Basal Structure

The large basal structure near the downstream margin of Figure 3.1 has an amplitude much larger than the steady-state maximum (Figure 3.9). Figure 3.10 shows a close-up view of the downstream basal structure, informally referred to as "Darth Vadar" in our internal discussions.

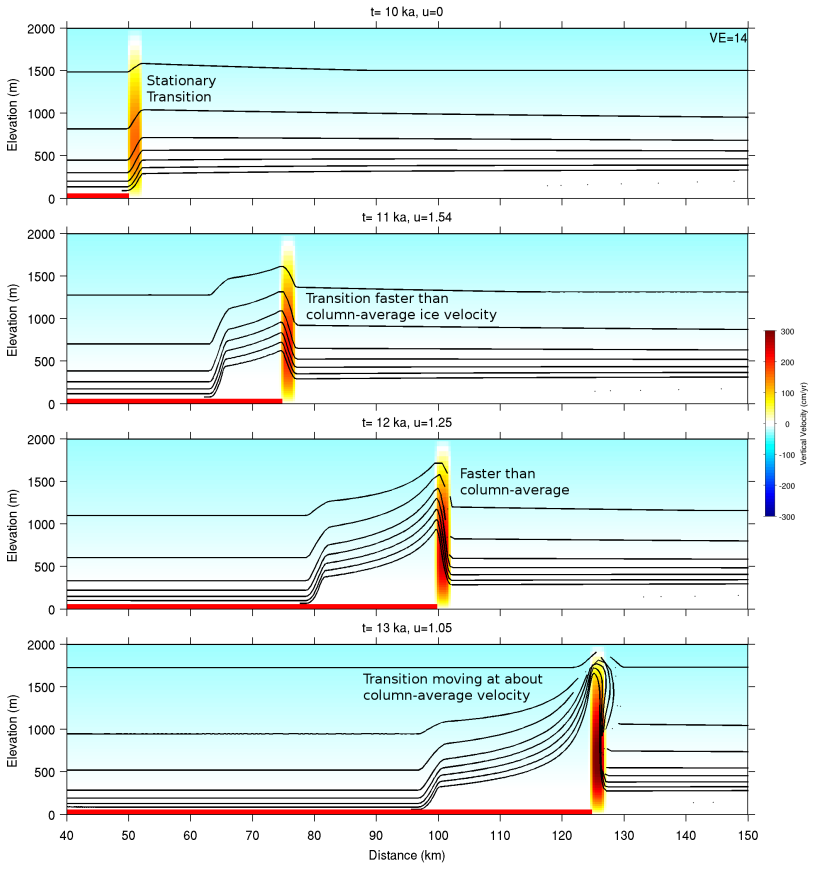

Figure 3.8: Stratigraphic test. In this test, a slip-to-deformation transition was prescribed with a constant ice surface. Top plot shows stratigraphic geometry after 10 ka of a stationary transition, other plots shows stratigraphy as the transition travels downstream at a constant 25 m/yr. Indicated values of u above each subplot denote transition velocity divided by column-average ice velocity.

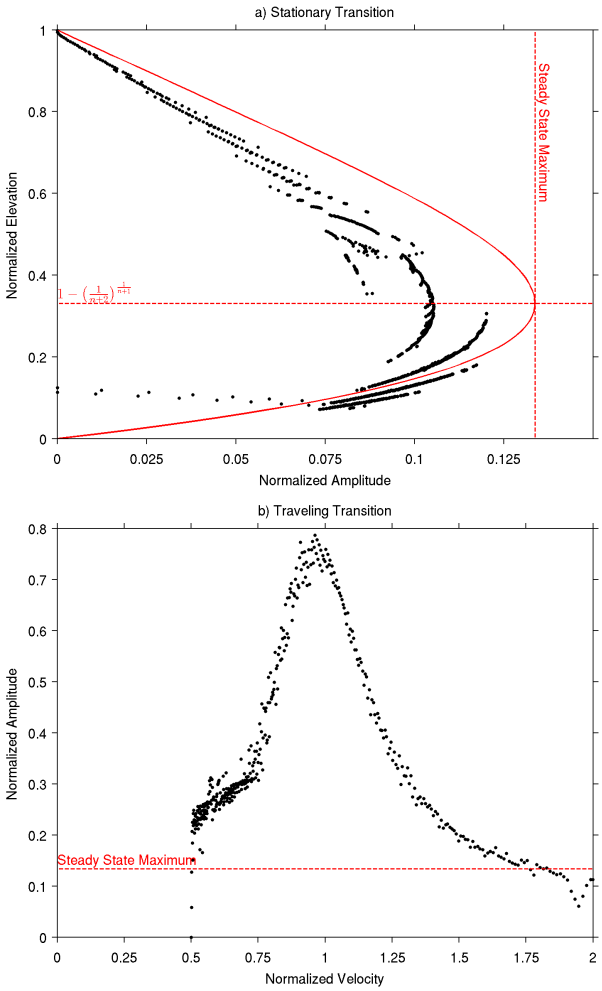

Figure 3.9: Stratigraphic test. Top plot shows stratigraphic amplitude as a function of elevation for 5 ka of a stationary transition. The analytic approximation is overlain, although care must be exercised because the analytic approximation assumes small layer displacements. Bottom plot shows how stratigraphic amplitude varies with normalized transition velocity.

Table 3.1: The following symbols and values were used in this chapter:

Symbol	Value	Units	Meaning
a	30	cm/yr	accumulation rate
A	variable	$Pa^{-3}s^{-1}$	rheological rate factor
A_0	4.9x10^{-25}	$Pa^{-3}s^{-1}$	value of rheological rate factor at reference temperature
B	variable	m	bed elevation
c_p	1900 for ice, 4200 for water	$Jkg^{-1}K^{-1}$	specific heat at constant pressure
d	variable	m	layer amplitude
D	variable	m	ice thickness
F	variable	-	sliding fraction
G	0.05	Wm^{-2}	geothermal flux
g	9.8	ms^{-2}	gravitational acceleration
k	2.4	$WK^{-1}m^{-1}$	thermal conductivity
L	333500	J/kg	latent heat of fusion
m	variable	m/s	basal melt rate
n	3	-	rheological exponent
P	variable	Pa	hydrostatic pressure
P_e	variable	-	Peclet number
Q	139 above T_0, 60 below T_0	kJ/mol	activation energy for creep
r	3	-	sliding law stress exponent
R	8.314	$Jmol^{-1}K^{-1}$	universal gas constant
S	variable	m	ice surface elevation
t	variable	s	time
T	variable	K	temperature
T_0	263	K	reference temperature
T_b	variable	K	basal temperature
T_m	variable	K	melting temperature
T_s	1	K	e-folding temperature for sliding law
T_{surf}	variable	K	surface temperature
u	variable	m/s	horizontal ice velocity
u_0	10	m/yr	reference value of sliding velocity
u_b	variable	m/s	sliding velocity
W	variable	m^2s^{-1}	water flux
w	variable	m/s	vertical ice velocity
x	variable	m	horizontal coordinate
z	variable	m	vertical coordinate
β	7.4x10^{-8}	KPa^{-1}	pressure dependence of the melting point
ϵ	variable	s^{-1}	strain rate
μ	variable	Pa*s	effective viscosity
ρ	917 for ice, 1000 for water	kgm^{-3}	density
σ	variable	Pa	deviatoric stress
τ_0	60	kPa	reference value of basal stress
τ_b	variable	Pa	basal shear stress
Φ	variable	Pa	hydraulic potential
κ	1.3x10^{-6}	m^2s^{-1}	thermal diffusivity

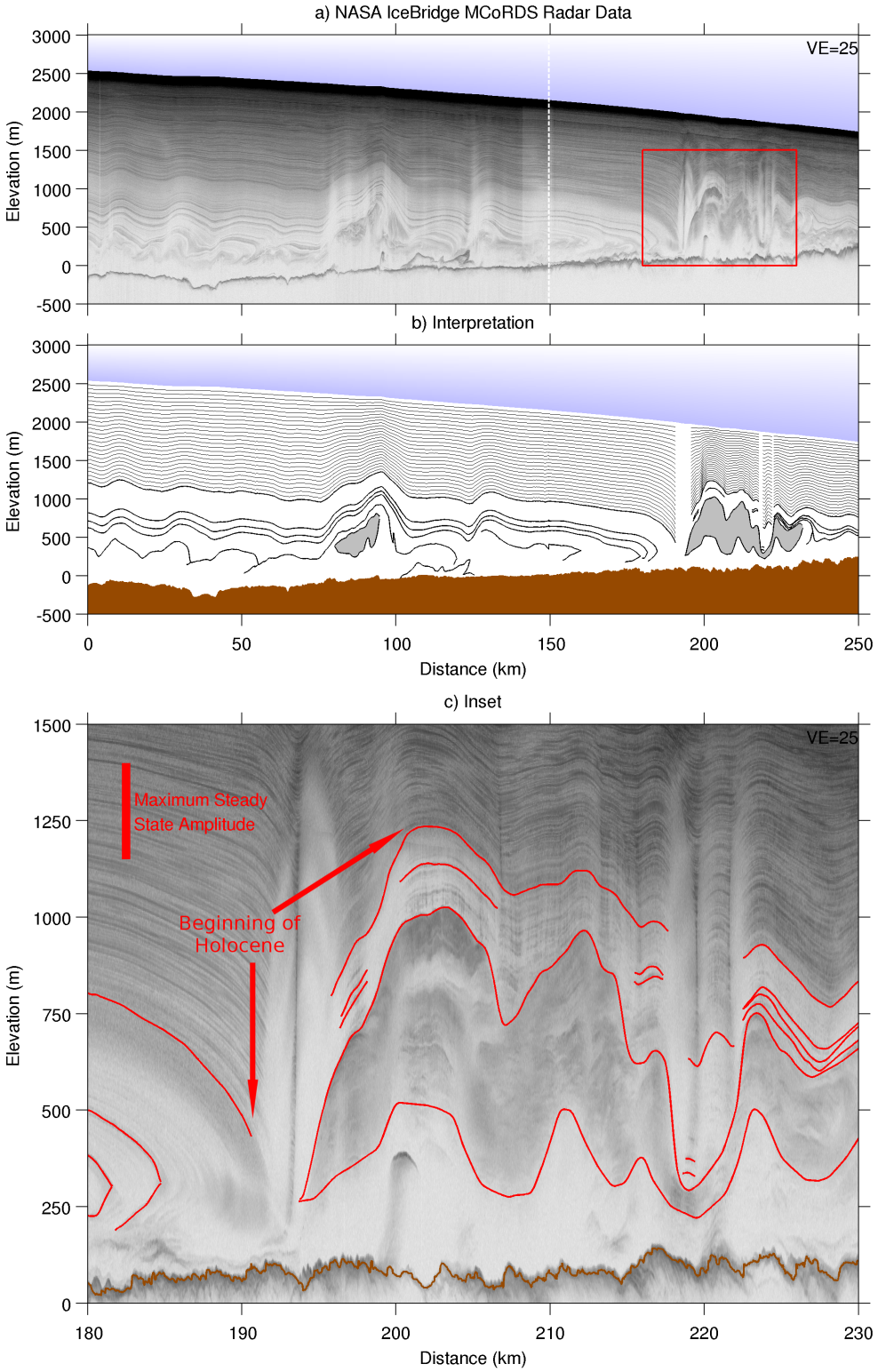

Figure 3.10: Inset of downstream stratigraphy in Figure 3.1. Top two plots as in Figure 3.1, bottom plot is inset with picked stratigraphy overlain. Vertical red bar shows the maximum stratigraphic amplitude for a stationary slip contrast (Figure 3.9). The base of the Holocene package (labeled) has a much larger amplitude than this.

Chapter 4

Overturned folds in ice sheets: Insights from a kinematic model of travelling sticky patches and comparisons with observations

Michael J. Wolovick, Timothy T. Creyts
In review at Journal of Geophysical Research: Earth Surface

4.1 Abstract

Overturned folds are observed in the Greenland ice sheet in regions where driving stress is highly variable. Transitions in stress modulate the tradeoff in ice flow between basal slip and internal deformation and deflect ice stratigraphy vertically. If these transitions move, the slip–deformation tradeoff can produce large folds. The resulting folds record the integrated effects of time–varying basal slip. To understand how dynamic changes in basal slip influence ice sheet stratigraphy, we develop a kinematic model of ice flow in a moving reference frame that follows a single travelling sticky patch. In this moving reference frame, the ice flow field forms a vortex with backward flow near the base. The backward flow allows ice to be trapped in the vortex as overturned folds develop. Sticky patches that travel downstream near the regional surface velocity produce the largest folds. We use the model as an interpretive tool to infer properties of basal slip from three folds of varying sizes. Our model suggests that the sticky patches underneath these folds propagated downstream at rates between one half and the full ice velocity. The regional flow regime for the smaller folds requires substantial internal deformation whereas the regime for the largest fold requires significantly more basal slip. Folds that overturn rapidly bring cold ice closer to the bed, influencing freezing and loss of basal water and potentially strengthening basal drag. The distribution and character of stratigraphic folds reflects the evolution and propagation of individual patches and their effects on ice sheet flow.

4.2 Introduction

Large irregular stratigraphic folds in the lower part of the ice sheet have been observed in radar data from both Greenland (*Bell et al.*, 2014; *MacGregor et al.*, 2015a) and Antarctica (*Bell et al.*, 2011). The deformation in the lower part of the ice sheet disturbs the overlying strata into anticlines, synclines, and overturned folds. The vertical amplitude of the folds ranges from the lower limit of radar detectability to over a kilometer (Figure 4.1).

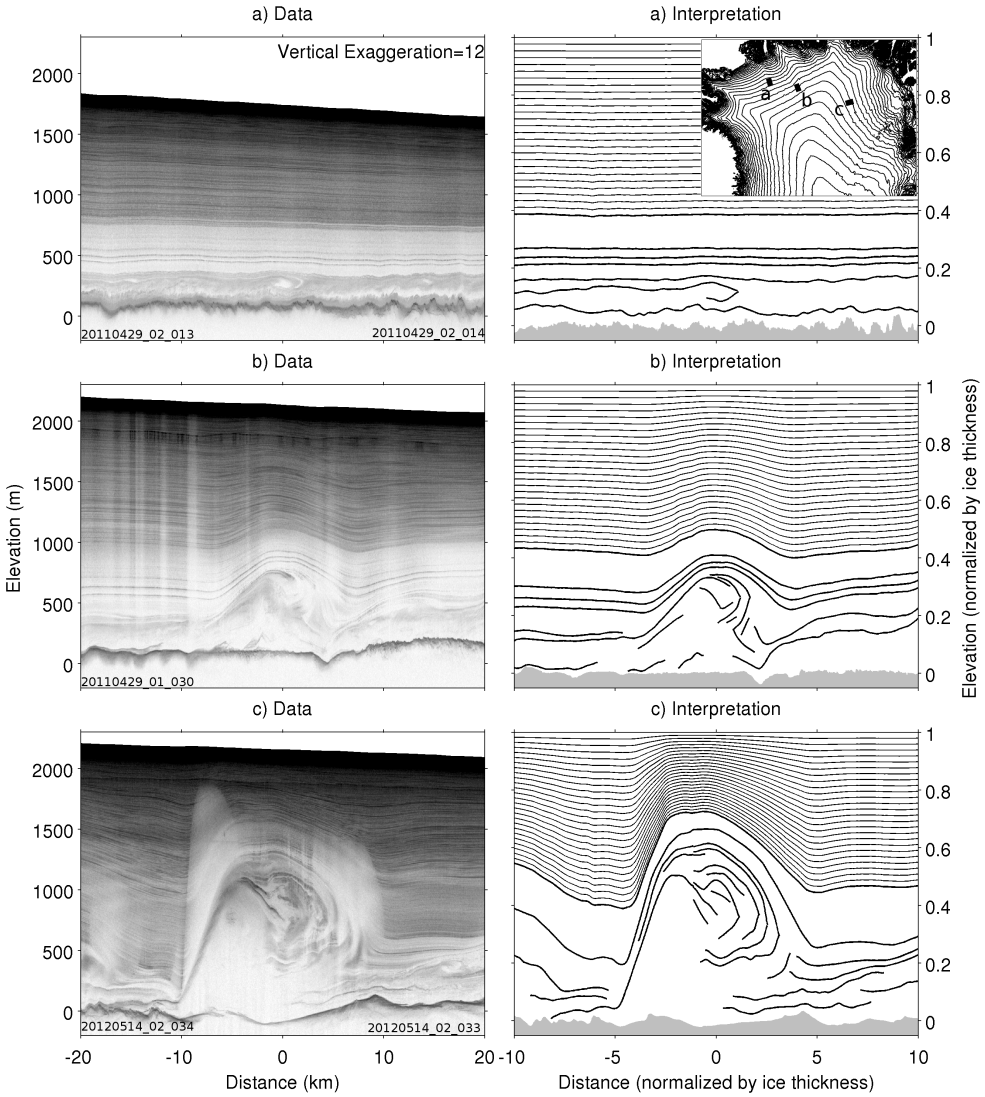

Figure 4.1: Overturned folds in ice-penetrating radar data from northern Greenland. a-c) Small, medium, and large fold, respectively. Left column are radar echograms, right column are interpretations of the echograms. The stratigraphic interpretation is shown on normalized coordinates. Elevation has been normalized using a low-pass filtered bed pick with a wavelength three times the mean ice thickness. The angles between the flight lines and the ice flow direction are 3°, 19°, and 9°. Radar data come from NASA's Operation IceBridge (*Li et al.*, 2013). Identification numbers at the bottom of the echograms can be used to locate the radar data at data.cresis.ku.edu/data/rds. (c) was also included in Figure 3c of *Bell et al.* (2014). Inset map shows location overlain on 100 m surface elevation contours.

The overturned stratigraphic folds in Greenland occur in regions where surface driving stress shows a repeating rib-like structure, and geophysical inversions show similar rib-like patterns in basal drag (*Sergienko et al.*, 2014). A series of ribs contains elongated patches of strong bed oriented oblique to flow within a larger weak-bedded region. Individual patches have widths of 2-6 ice thicknesses and lengths of 5-30 ice thicknesses. The exact locations and dimensions of the basal ribs depend on details of the inversion process, but the ribbed structure of surface driving stress is a robust result that depends only on ice sheet geometry (e.g., *Bamber et al.*, 2013a; *Fretwell et al.*, 2013).

A consequence of patchy basal drag and driving stress is that the ice flow regime shifts between internal deformation and basal slip. When basal drag is low but velocity is high, the entire ice sheet slides in plug flow over the bed. Higher basal drag causes reduced sliding and higher shear stresses within the ice column, leading to an increase in internal deformation. Internal deformation produces a shear layer in the lower third of the ice column where velocity varies rapidly with depth, and a thick mass of ice higher in the column moving quickly downstream at a nearly uniform rate. Here, we show how the tradeoff between basal slip and internal deformation associated with a sticky patch can produce overturned stratigraphic folds when the sticky patch moves downstream over time.

There are two factors necessary to produce overturned folds, an initial stratigraphic disturbance and englacial shear (*Waddington et al.*, 2001; *Jacobson and Waddington*, 2004, 2005). The initial stratigraphic disturbance can be caused by a transition between basal slip and internal deformation. The change in ice velocity profile across this transition induces vertical flow that distorts ice sheet strata. This process, the "Weertman Effect" (*Weertman*, 1976; *Hindmarsh et al.*, 2006), has been used to study stationary transitions between sliding and internal deformation, such as those found on the shores of subglacial lakes (*Hindmarsh et al.*, 2006; *Parrenin and Hindmarsh*, 2007; *Leysinger Vieli et al.*, 2007). When these transitions move downstream, a dynamic Weertman Effect is capable of producing large overturned basal folds (*Wolovick et al.*, 2014). The second factor, englacial shear, is necessary to turn an initial stratigraphic disturbance into an overturned fold. The increase in velocity above the bed causes englacial disturbances to steepen and eventually roll over (*Waddington et al.*, 2001). In a train of travelling sticky and slippery patches (*Wolovick et al.*, 2014), the englacial shear is found above the sticky patches, where ice moves by internal deformation rather than by sliding. Here, we focus on a single travelling sticky patch in order to better understand stratigraphic overturn produced by travelling patches.

4.3 Theory

We use a kinematic model in a moving reference frame to systematically explore the relationship between travelling sticky patches and the associated stratigraphic folds. We vary patch propagation velocity and the slip contrast between the patch and the far field. The tradeoff between basal slip and internal deformation is represented by using a linear superposition of a plug flow profile and a shear profile for the horizontal flow field. Mass conservation determines vertical velocity from the horizontal flow field.

We make several simplifying assumptions. Surface accumulation and basal melt are set to zero. We use this simplification because travelling sticky patches are relatively short-

wavelength features located away from a dome. Most of the mass flux moving through the ice sheet above the sticky patches is horizontal flow coming from upstream, rather than local snow deposition. For example, for a surface accumulation rate of 0.1 m a^{-1}, an ice flow rate of 10 m a^{-1}, and a sticky patch 10 ice thicknesses long, 90% of the mass flux above the sticky patch comes from upstream. Ice thickness is assumed to be constant. The shear profile we use to represent internal deformation is a simple power-law with depth, neglecting the effects of temperature, longitudinal stresses, and other variations in ice rheology.

4.3.1 Kinematic Modelling Strategy

Our model follows a single sticky patch in a moving reference frame as it travels downstream along an ice sheet flowline. The kinematic model has a small domain (∼40 km) and operates in a moving reference frame travelling at the same velocity as the sticky patch. By operating in a moving reference frame that follows the patch, we are able to gain a better understanding of the processes causing stratigraphy to fold and potentially overturn.

4.3.2 Mass Conservation

The mass conservation equation is expressed here in two dimensions as,

$$\frac{\partial u}{\partial x} + \frac{\partial w}{\partial z} = 0, \tag{4.1}$$

where x is along-flow distance, z is elevation, u is horizontal velocity, w is vertical velocity, and cross-flow spreading has been assumed to be zero.

4.3.3 Nondimensionalization

Distance and elevation are normalized by the ice thickness,

$$\begin{aligned} \hat{x} &= \frac{x}{D}, \\ \hat{z} &= \frac{z - B}{D}, \end{aligned} \tag{4.2}$$

where D is ice thickness and B is bed elevation. Over-hats indicate nondimensionalized variables.

Both velocity components are normalized by the column averaged horizontal velocity, $\bar{u}$, while horizontal velocity is also measured relative to the velocity of the propagating sticky patch, u_p,

$$\begin{aligned} \hat{u} &= \frac{u - u_p}{\bar{u}}, \\ \hat{w} &= \frac{w}{\bar{u}}. \end{aligned} \tag{4.3}$$

The nondimensionalized mass conservation equation then follows as,

$$\frac{\partial \hat{u}}{\partial \hat{x}} + \frac{\partial \hat{w}}{\partial \hat{z}} + \frac{\hat{u}}{\bar{u}} \frac{\partial \bar{u}}{\partial \hat{x}} = 0, \tag{4.4}$$

where the additional term accounts for the gradient of the column velocity, and the gradient of ice thickness is assumed to be negligible.

4.3.4 Flow Field

The linear superposition of sliding and internal deformation is,

$$\hat{u} = \hat{u}_b + (1 - \hat{u}_b)\frac{n+2}{n+1}(1 - (1 - \hat{z})^{n+1}) - \hat{u}_p, \tag{4.5}$$

where $\hat{u}_b$ is the normalized sliding velocity and n is the rheological exponent for ice, taken to be 3 by convention (*Cuffey and Paterson*, 2010). Examples of this flow field with different values of basal slip are shown in Figure 4.2a. When $\hat{u}_b = 1$, the ice sheet moves by a vertically uniform plug flow. As the sliding velocity $\hat{u}_b$ decreases, the shear profile in the lower part of the ice sheet becomes more pronounced and velocity in the upper part of the ice sheet increases to keep the average flow rate constant.

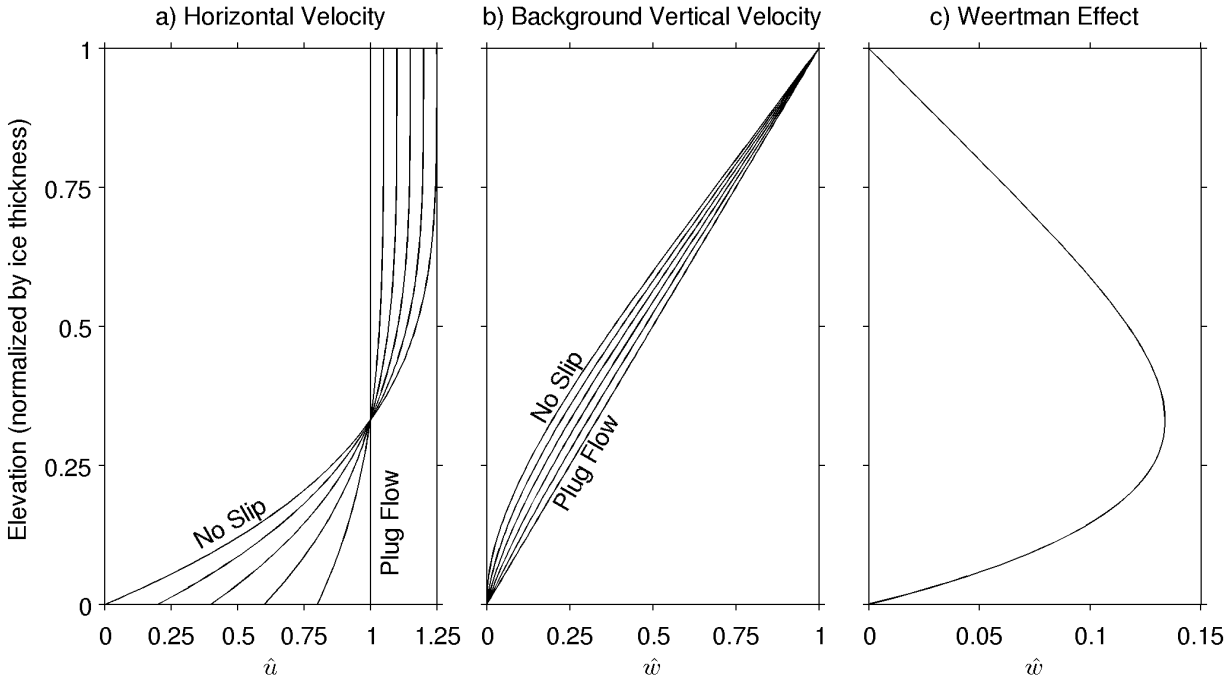

Figure 4.2: Velocity Functions. a) Horizontal velocity. b) Background vertical velocity, or the vertical flow that balances surface accumulation in steady state. c) Weertman effect, or the vertical flow caused by the variation in basal slip. Panel (a) can be redimensionalized by multiplying by the column velocity, $\bar{u}$, (b) can be redimensionalized by multiplying by the gradient in total ice flux, $-\partial(\bar{u}D)/\partial x$ (equal to surface accumulation in steady state), and (c) can be redimensionalized by multiplying by the gradient in sliding flux, $-\partial(u_b D)/\partial x$. In the first two panels a range of values of basal slip are shown. Note the scale change between (b) and (c).

Once we have specified the horizontal component of velocity, we can use mass conservation to derive the vertical velocity component,

$$\hat{w} = \underbrace{\frac{-1}{\bar{u}}\frac{\partial \bar{u}}{\partial \hat{x}}\left[\frac{1-\hat{u}_b}{n+1}(1-\hat{z})^{n+2} + \left(\hat{u}_b + (1-\hat{u}_b)\frac{n+2}{n+1}\right)\hat{z} - \frac{1-\hat{u}_b}{n+1}\right]}_{\text{background vertical flow}}$$
$$\underbrace{-\frac{\partial \hat{u}_b}{\partial \hat{x}}\frac{1}{n+1}\left(1-\hat{z}-(1-\hat{z})^{n+2}\right)}_{\text{Weertman effect}}. \tag{4.6}$$

In this equation, the background vertical flow is proportional to the gradient in column-average velocity ($\partial\bar{u}/\partial\hat{x}$), and the Weertman effect is proportional to the gradient in basal slip ($\partial\hat{u}_b/\partial\hat{x}$). The background vertical flow (Figure 4.2b) is the term that balances surface accumulation in a steady state. In a plug flow regime, the background vertical flow is simply a linear gradient from the bed to the surface. When horizontal flow is by internal deformation, the background vertical flow profile is curved. The Weertman effect (Figure 4.2c) is the vertical velocity caused by the tradeoff between slip and deformation. The Weertman effect is zero at the bed and the surface, with a maximum in the ice column at an elevation about 30% above the bed. The vertical flow drops to zero at both the bed and the surface because the Weertman effect represents an internal rearrangement of mass within the ice column.

4.3.5 Stratigraphic Overturning

Stratigraphic overturn above a travelling sticky patch is caused by an overturning vortex. In a reference frame that moves with the travelling patch, there is backward flow near the bed and forward flow higher in the column. Shear between the forward and backward flows produces the vortex. The ice column above a travelling sticky patch is split into three regions: a lower throughflow, the overturning vortex, and an upper throughflow (Figure 4.3). In the lower throughflow, ice that is moving backward relative to the travelling patch flows past the patch and escapes into the far field. The lower throughflow only exists if the far-field slip rate is less than the propagation velocity, because the lower throughflow cannot escape if there is no backward flow in the far field. Above the lower throughflow is trapped ice inside the overturning vortex. Within the overturning vortex, forward flow and backward flow balance one another, causing the ice to rotate over time. Ice within the overturning vortex remains above the travelling patch as the patch moves downstream rather than escaping into the far field. Above the overturning vortex is the upper throughflow, where ice that is moving faster than the patch escapes into the far field.

The boundaries between the overturning vortex and the two throughflows can be computed based on mass conservation. The total flux in the far-field ice column must be the same as the total flux across the sticky spot in all reference frames, regardless of the presence of forward or backward flow. The forward flux in the upper throughflow must also equal the forward flux in the far-field. Likewise, the backward flux in the lower throughflow must equal the backward flux in the far field. The remaining flow above the sticky spot must be evenly balanced forward and backward flux in the overturning vortex. The process of

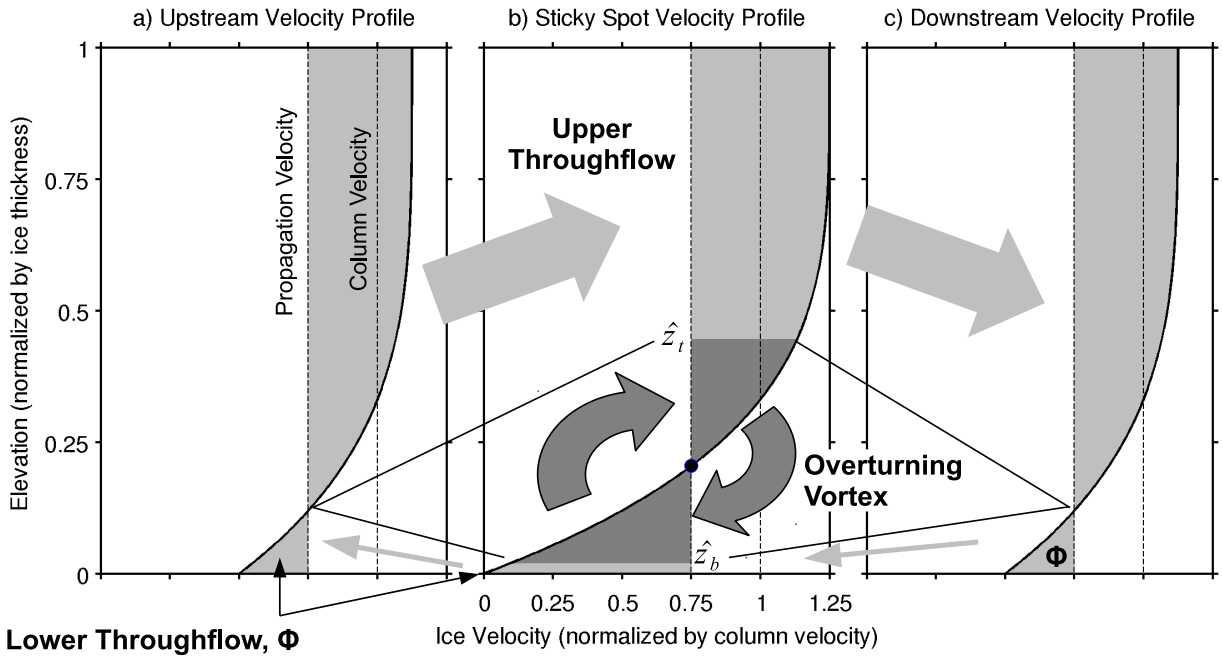

Figure 4.3: Schematic Explanation of Stratigraphic Overturn. a) Upstream velocity profile, b) sticky patch velocity profile, c) downstream velocity profile. In this example the propagation velocity is 0.75 times the column velocity, the center of the sticky patch has no slip, and the far-field flow regime has half slip. The upper throughflow consists of ice flux moving faster than the sticky patch, the lower throughflow consists of ice moving slower than the sticky patch, and stratigraphic overturn occurs for the vortex in the middle.

computing the boundaries of the overturning vortex begins with computing the magnitude and thickness of the lower throughflow.

The magnitude of the lower throughflow, ϕ, is given by the integrated backward flow in the far-field (Figure 4.3),

$$\phi = \int_{\hat{u}_{ff} < \hat{u}_p} (\hat{u}_{ff} - \hat{u}_p) d\hat{z} \tag{4.7}$$

where $\hat{u}_{ff}$ is the far-field velocity profile, and integration is over depths where the far-field velocity is less than the propagation velocity. In Figure 4.3b, ϕ is the thin lightly shaded area near the bed, while in Figure 4.3 a and c, ϕ is the lightly shaded triangle to the left of the vertical line representing propagation velocity. All of the areas representing the lower throughflow are the same in the three profiles. The bottom of the overturning vortex, $\hat{z}_b$, is determined by the top of the lower throughflow in the sticky patch velocity profile,

$$\phi - \int_0^{\hat{z}_b} (\hat{u} - \hat{u}_p) d\hat{z} = 0, \tag{4.8}$$

where the velocity profile $\hat{u}$ used in the integration is taken from the center of the sticky patch. Equation 4.8 determines the boundary between the thin lightly shaded lower throughflow in Figure 4.3b and the darkly shaded trapped ice. The top of the vortex, $\hat{z}_t$, is determined by mass conservation as the elevation where forward and reverse flow balance one another,

$$\int_{\hat{z}_b}^{\hat{z}_t} (\hat{u} - \hat{u}_p) d\hat{z} = 0. \tag{4.9}$$

If there is no reverse flow in the far field, then the vortex sits on the bed and $\hat{z}_b = 0$. The remaining ice flow above the top of the vortex is the upper throughflow. The magnitude of the upper throughflow is equal to the forward ice flux in the far field.

We use Equations 4.7, 4.8, and 4.9 to solve for the top and bottom of the vortex as a function of the propagation velocity of the patch and the regional slip rate (Figure 4.4). The parameter space defined by those two variables is split into three separate regions depending on where the vortex is located in the ice column (Figure 4.4d). When the regional slip rate is greater than the propagation velocity, no lower throughflow forms. The lower throughflow requires backward flowing ice to escape into the far field, which cannot happen if all of the ice in the far field is moving faster than the travelling patch. When there is no lower throughflow the top of the vortex is a function of propagation velocity only, indicated by vertical contours in Figure 4.4a, and the bottom of the vortex rests on the bed (Figure 4.4b).

The two remaining regions of Figure 4.4 are separated by the line where propagation velocity equals far-field surface velocity. When propagation velocity is greater than far-field surface velocity (the upper right triangle in Figure 4.4), there is no upper throughflow. The upper throughflow requires forward flow in order to escape to the far field, and there is no forward flow when the propagation velocity is greater than the surface velocity. Without an upper throughflow, the overturning vortex is in contact with the surface (Figure 4.4a). Observations indicate that overturned folds are always in the lower portion of the ice sheet, and never in contact with the surface.

When propagation velocity is greater than far-field slip rate and less than far-field surface velocity both an upper and a lower throughflow exist. In this case the vortex forms in the middle of the ice column (Figure 4.4). The lower throughflow is thin and the bottom boundary generally is close to the bed (Figure 4.4b). In this region overturn geometry is a function of both propagation velocity and regional slip rate, indicated by curved contours in Figure 4.4 a and b. The total thickness of the overturning vortex is largest when the sticky patch moves downstream at the far-field surface velocity.

We have assumed that the center of the sticky patch has no basal slip and ice moves completely by internal deformation. When the sticky patch is weaker, greater propagation velocities and far-field slip rates are required to produce the same thickness of overturn. Weakening the sticky patch linearly shrinks the results in Figure 4.4 towards $(1, 1)$, the point where far-field slip rate and propagation velocity both equal the ice column velocity. The shapes of the contours and the critical triangular regions in Figure 4.4 are unaffected by the slip rate in the sticky patch itself, they are simply confined to an increasingly small region of parameter space around $(1, 1)$.

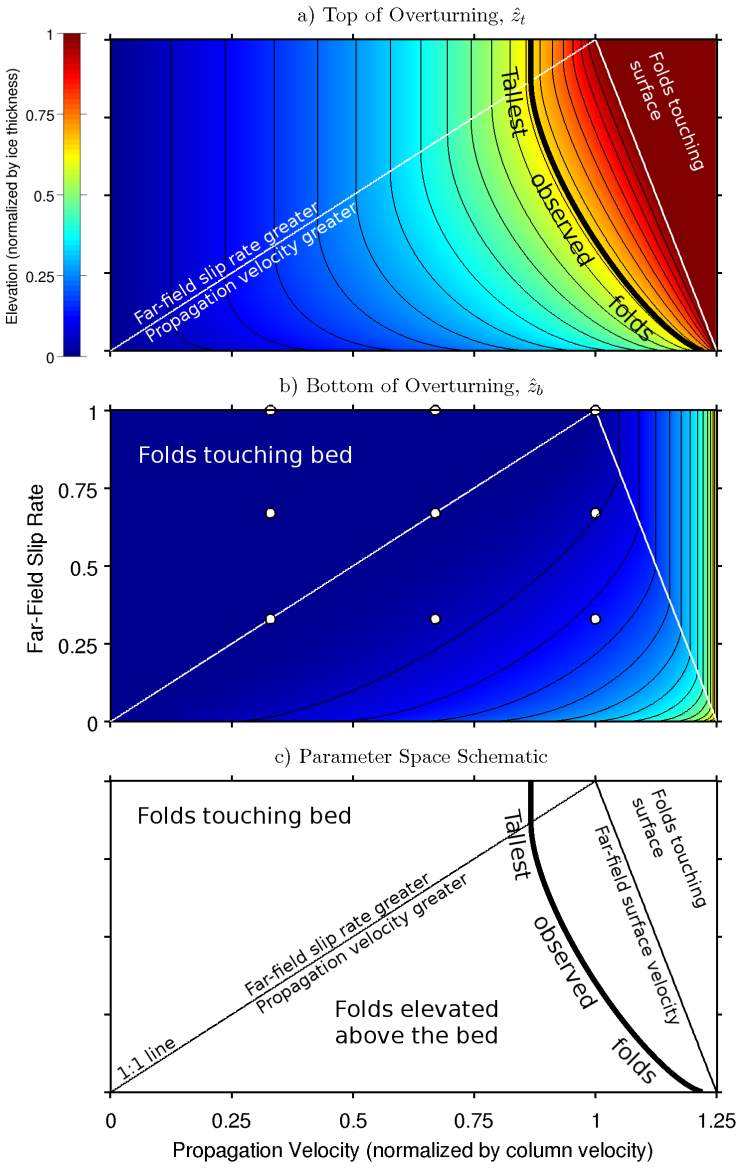

Figure 4.4: Dimensions of the overturning vortex as a function of propagation velocity and far-field slip rate. a) Top and (b) bottom of the overturning vortex. c) Schematic diagram of the important regions of parameter space. The 1:1 line and the line where propagation velocity equals far-field surface velocity separate parameter space into three separate triangles, where the overturning vortex is either in contact with the bed, suspended in the middle of the ice column, or in contact with the surface. Thick curved line indicates the approximate height of the tallest observed folds. White circles in (b) show the locations of the model runs in Figure 4.6.

4.3.6 Numerical Methods

We use a particle tracking model to simulate ice sheet stratigraphy in a moving reference frame. The velocity field is constructed using equations 4.1 and 4.5. Strata are initially horizontal, and the boundary conditions at the edges of the domain are constant layer elevation. We set accumulation to zero, so ice only enters or exits the domain on the side boundaries.

The velocity field is interpolated linearly from an Eulerian grid onto the Lagrangian tracer locations. The model tracks the connectivity between tracers in coherent layers. We plot the stratigraphy using straight line segments connecting the tracers. We use a model domain 20 ice thickness long. We run the model to an elapsed time of 20 times $D/\bar{u}$. This is the throughflow timescale, or the average time it takes ice to traverse the model domain. The throughflow timescale for a sticky patch is also the characteristic overturn timescale for the vortex above that patch (Section 4.5.2). To simplify the analysis, we choose to investigate gaussian sticky patches. A gaussian function provides a smooth variation in slip that approximates the averaging effects of longitudinal stress gradients that we do not include explicitly (*Kamb and Echelmeyer*, 1986). The patch size is set to a standard deviation of 2.5 D, much smaller than the model domain.

4.4 Results

We investigate the relationship between travelling sticky patches and ice sheet stratigraphy. First, we show how the overturning vortex is reflected in velocity vectors in a moving reference frame. Next, we show stratigraphic snapshots for nine combinations of far-field slip rate and propagation velocity. We space the combinations to form a 3x3 grid in increments of 1/3 $\bar{u}$ (Figure 4.4b). Finally, we use this model to infer slip rates and propagation velocities based on measurements of fold geometry.

4.4.1 Velocity Vectors

The propagation velocity has a strong control on the form of the velocity field and the development of englacial vortices (Figure 4.5). When the propagation velocity is zero, the velocity field above the sticky patch simply reflects a shear profile within the ice, while velocity in the far field is uniformly forward (Figure 4.5a). The stationary Weertman Effect produces only a small vertical deflection of the vectors in Figure 4.5a. When the sticky patch moves downstream, a vortex forms near the bed. Figure 4.5 shows how the size of the vortex responds to increasing propagation velocity when far-field slip rate is held constant. When the patch is propagating at half the ice column velocity (Figure 4.5b), ice near the bed moves slower than the propagation velocity. This basal ice flows backward in the moving reference frame. Higher up, the ice moves forward. The backward flowing ice near the bed and the lowest part of the forward flowing ice form a closed loop in an overturning vortex. The vortex occupies roughly the lower quarter of the ice column, and flow vectors in the overlying ice are deflected vertically around the vortex. When propagation velocity equals the column velocity (Figure 4.5c), the overturning vortex expands to fill the entire ice column and velocity vectors in the far field fall off to zero. The result is that the entire ice column is trapped above the travelling sticky patch. Though vortices spanning the full ice thickness are not observed, this end-member result suggests that time-varying basal slip can have a very large impact on ice sheet stratigraphy.

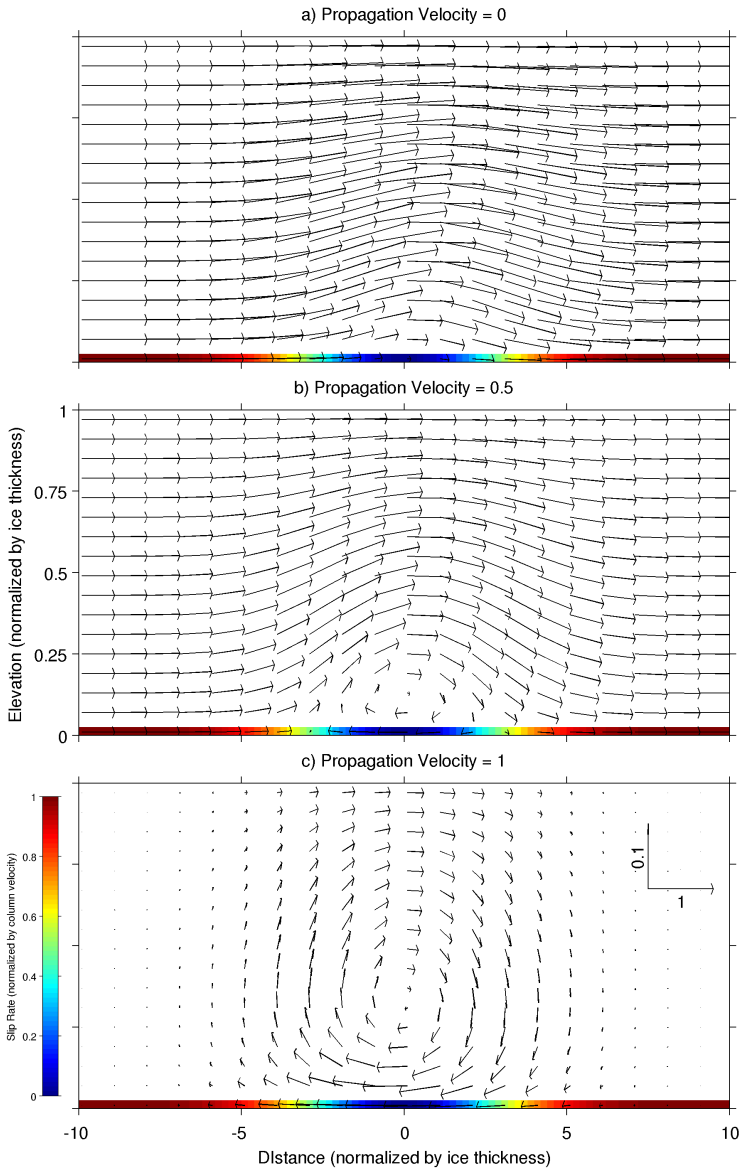

Figure 4.5: Velocity vectors in a moving reference frame. a-c) Relative velocity field for a travelling sticky patch as the propagation velocity of the sticky patch increases from 0 to 1. Scale arrows in panel (c) show relative scaling of horizontal and vertical components. Color scale at the bottom of the plots shows the basal slip rate. The relative scaling of the horizontal and vertical components of the velocity vector and the exaggeration of the figure itself are both 10. The far-field flow regime is plug flow in these plots, corresponding to points along the upper border of the parameter space in Figure 4.4.

4.4.2 Stratigraphy

In order to better understand the stratigraphic structures produced by our simple model, we present stratigraphy for a variety of parameter combinations based on our analysis in Section 4.3.5. We vary far-field slip rate and propagation velocity to form a 3x3 grid in parameter space (Figure 4.4b). Both far-field slip rate and propagation velocity vary by 1/3 of the column velocity. All of the model runs produce an overturning vortex in the

lower part of the ice sheet and an anticline in the upper part (Figure 4.6). Vortex size increases with both increasing far-field slip rate and increasing propagation velocity. Within the vortex, stratigraphic order is reversed, with younger layers underneath older layers. Because of our short model integration, we do not see any repeated overturns. When the far-field slip rate is greater than or equal to propagation velocity (Figure 4.6a-e,g) no lower throughflow forms, and layers within the vortex approach the bed. Conversely, when far-field slip rate is less than propagation velocity (Figure 4.6f,h,i) a lower throughflow should be present. The lower throughflow can be seen as a subhorizontal layer above the bed but below the vortex (Figure 4.6i). Short integration times and a finite number of layers make it difficult to identify the lower throughflow in Figure 4.6 f and h. The upper two plots in the right-hand column (Figure 4.6 c,f) are outside the range of observed folds (Figure 4.4a), while the others are within the range of observations. The stratigraphy models confirm the existence of overturning vortices described earlier and provide us with a schematic picture of what englacial stratigraphy produced by travelling sticky patches might look like. The stratigraphy models also indicate the difficulty in identifying a thin lower throughflow near the bed.

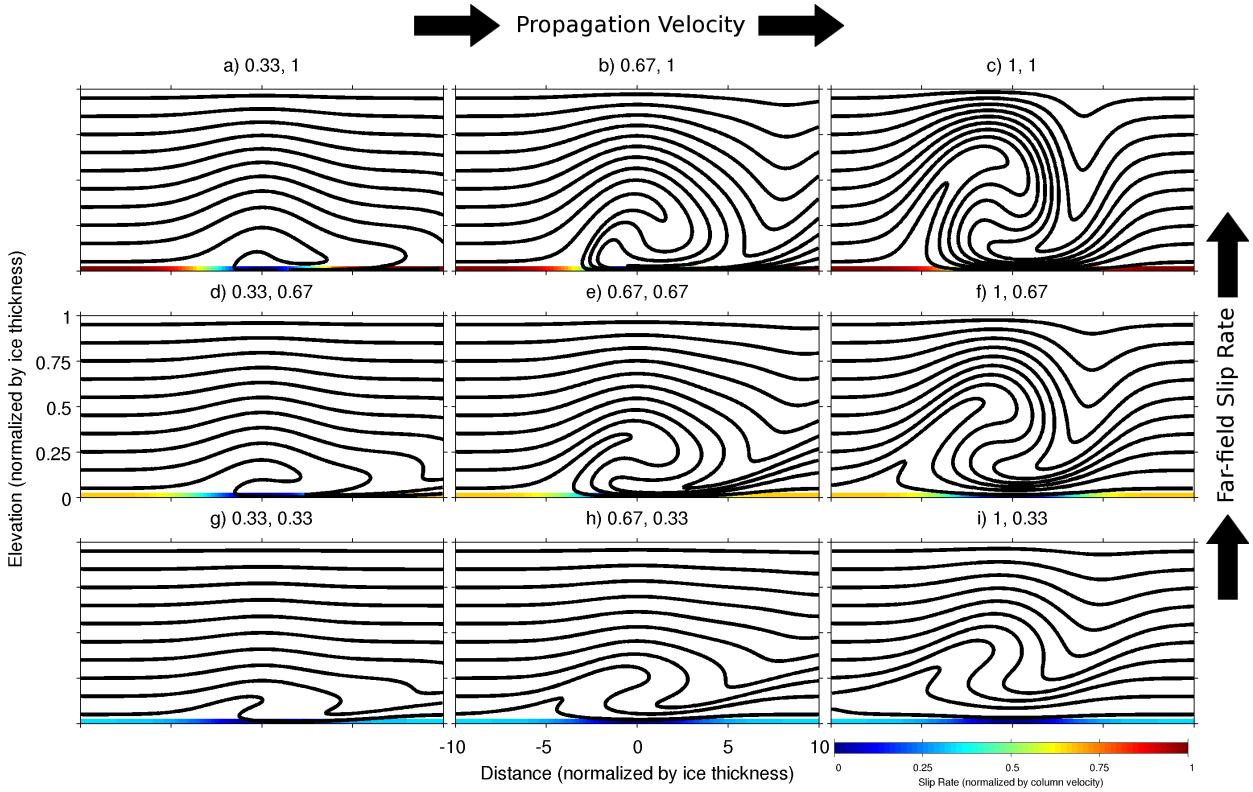

Figure 4.6: Model stratigraphy. a-i) Stratigraphic snapshots after an elapsed time of 20 times $D/\bar{u}$. Model runs form a 3x3 grid in the parameter space of propagation velocity (horizontal axis) and far-field slip rate (vertical axis). Labels above the plots give the coordinates of each model run in Figure 4.4. The first number is propagation velocity, the second is far-field slip rate. Color scale at the bottom of each panel indicates basal slip rate. Vertical exaggeration is 10.

4.4.3 Interpretation of Observed Folds

We use this model to interpret three example stratigraphic folds (Figure 4.1) in terms of moving sticky patches. All three overturned folds were sampled in radar lines subparallel to flow. The accumulation rates are 14, 17, and 10 cm/yr. Basal topography is less than 10% of ice thickness, and basal melt rates are unknown. Additionally, ice in Greenland has

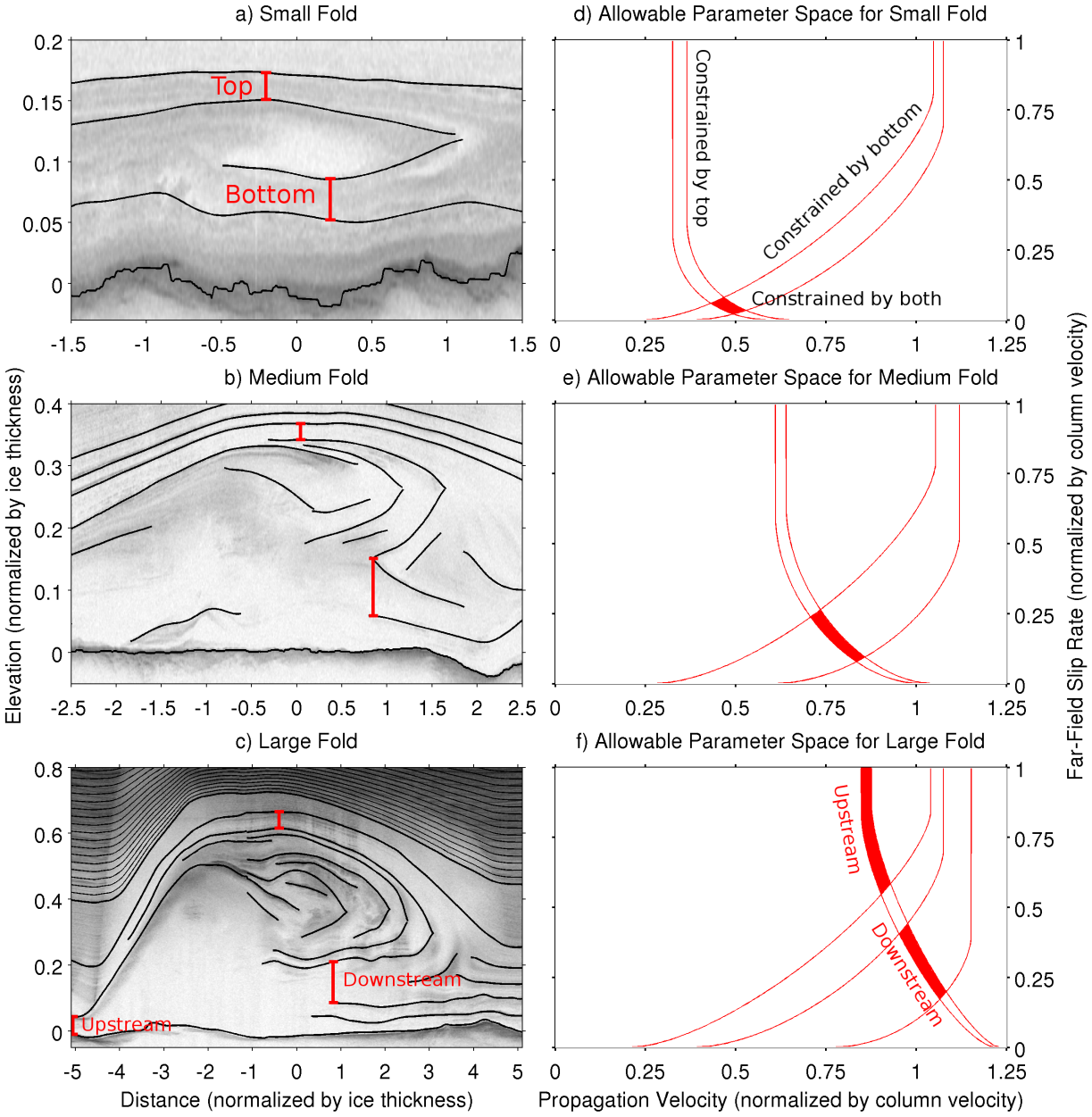

Figure 4.7: Measurements of the overturned folds in Figure 4.1, and corresponding constraints on parameter space. a-c) Echograms with picks and measurements overlain. Images correspond to plots a-c in Figure 4.1. Note scale change to zoom in on overturned folds. d-f) Parameter space corresponding to each fold. Red lines represent the constraints provided by the top or bottom of the fold separately, red shading represents the combined constraint.

rheological contrasts resulting from impurities, differing crystal sizes, and warmer temperatures near the bed. These environmental variables differ from the model assumptions of flow perfectly along track, no surface accumulation, a flat bed, and a homogeneous power-law rheology.

These overturned folds appear to have bottom boundaries above the bed based on the presence of continuous reflectors underneath the overturned portions. These non-overturned layers underneath the overturned units suggest the presence of a lower throughflow. A lower throughflow can only be present if the propagation velocity is greater than the far-field slip rate (Section 4.3.5). The larger two structures (Figure 4.1b,c) also deflect the upper layers into anticlines.

Regional slip rate and patch propagation velocity can be constrained by measuring the top and bottom boundaries of observed overturned folds. The "top" is defined as the highest point of the highest layer that can be traced to an overturn. We use this definition because it is compatible with the mass-conservation equations used to define the boundaries of the overturning vortex (Section 4.3.5). By using this definition we obtain higher estimates of fold amplitude than *Bell et al.* (2014). The "top" defined here is a meteoric layer, as opposed to the lower disorganized scattering reflectors in the "basal units" (*Bell et al.*, 2014). The uncertainty of the top is the difference between the highest point of the uppermost overturned layer and the next traceable layer overlying it. The "bottom" is defined in a similar way, as the lowest point of the lowest layer that can be traced to an overturn. If a traceable layer cannot be found below the lowest overturned layer, the uncertainty of the bottom extends to the bed. Measurements of fold tops and bottoms are shown in Figure 4.7a-c. The large fold in Figure 4.7c is big enough to have two bottom measurements, one each for the upstream and the downstream sides.

The measurements of fold top and bottom define permissible combinations of regional slip rate and patch propagation velocity (Figure 4.7d-f). The measurements of fold top and bottom correspond to contours in Figure 4.4 a and b, respectively. The uncertainty in the measurements corresponds to a set of parallel contours. When the fold is elevated above the bed, contours of constant top elevation and constant bottom elevation cross each other. The intersection of the contours defines a closed region in parameter space that is consistent with the observations.

Larger folds are produced by faster sticky patches and higher regional slip rates (Figure 4.7 d-f). Increasing fold size correlates with both increasing far-field slip rate and increasing propagation velocity. The dependence of fold amplitude on regional slip rate is weaker than the dependence on propagation velocity, resulting in more overlap between the examples. All three folds have a propagation velocity between approximately one half the column velocity and the column velocity. Only the downstream margin of the large fold is consistent with a propagation velocity greater than the column velocity (Figure 4.7f). The two smaller folds and the downstream margin of the largest fold indicate relatively low far-field slip rates of less than half the column velocity. The upstream margin of the largest fold is consistent with high sliding rates in the surrounding region.

Our results are consistent with the interpretation of *Bell et al.* (2014) that the largest fold (Figure 4.7c,f) is related to the freeze-on of basal water. Upstream of the fold, slip rates are high, indicating the presence of basal water. The uncertainty in the upstream measurement even allows for full plug flow. Underneath the center of the fold slip rate drops, consistent

with loss of basal water, potentially due to freezing along the upstream margin of the fold. Downstream of the fold, slip rate recovers to an intermediate value of about a quarter to a half of the column velocity. In our interpretation, this entire system of basal processes would be travelling downstream at 80-100% of the velocity of the overlying ice column as the deformation continues.

4.5 Discussion

Basal traction and slip are highly variable underneath ice sheets (*Sergienko et al.*, 2014). We have shown that transitions between slip and stick produce large overturned folds for a wide range of far-field slip rates and patch propagation velocities. While we have chosen a simple power-law rheology in our model, our results can be generalized to other ice rheologies. The transition between a shear profile and a plug flow profile produces folds. We expect folds to be produced wherever basal slip gives way to internal deformation over short distances. If the transitions between slip and stick migrate downstream, folds become large and overturned.

Our results have direct implications for ice streams and their tributaries, where variations in driving stress and basal drag are especially pronounced (*Joughin et al.*, 2004b, 2009; *Sergienko and Hindmarsh*, 2013; *Sergienko et al.*, 2014). If sticky patches in the tributaries move, they will induce velocity vortices and folds. As ice flows into the main trunk of the stream, velocities increase dramatically (*Joughin et al.*, 2010; *Rignot et al.*, 2011). If the sticky patches cannot match the increase in flow speed, then the stratigraphic structures become separated from the patches and are advected downstream. Longitudinal stretching will thin the folds over time, while internal deformation (if present) would augment the folds. Surface accumulation compresses the folds downward. If there is little deformation then structures will advance as a package, crossing the grounding zone and potentially confounding interpretations of englacial stratigraphy there (*Christianson et al.*, 2013; *Bingham et al.*, 2015).

4.5.1 Thermal Overturn

Thermal structure near the bed exerts a critical control on ice flow, deformation, basal melting, and water transport. If stratigraphic overturn happens more rapidly than thermal diffusion, then the strata will carry their temperature structure with them as they deform and the ice sheet will develop a temperature inversion. As layers fold in the overturning vortex, initially horizontal isotherms will be advected and become overturned as well. The balance between advection and diffusion is described by the Peclet number, P_e,

$$P_e \equiv \frac{\bar{u}D}{\hat{L}\kappa} \tag{4.10}$$

where $\hat{L} \equiv L/D$ is the normalized length of the sticky patch, and κ is the thermal diffusivity of ice. For an ice sheet 2-3 km thick, with a sticky patch 5-10 ice thicknesses (10-30 km) long, and a column velocity of 1-100 m/yr, the Peclet number ranges between approximately 5 and 1500. Values of the Peclet number much larger than one indicate that advection dominates

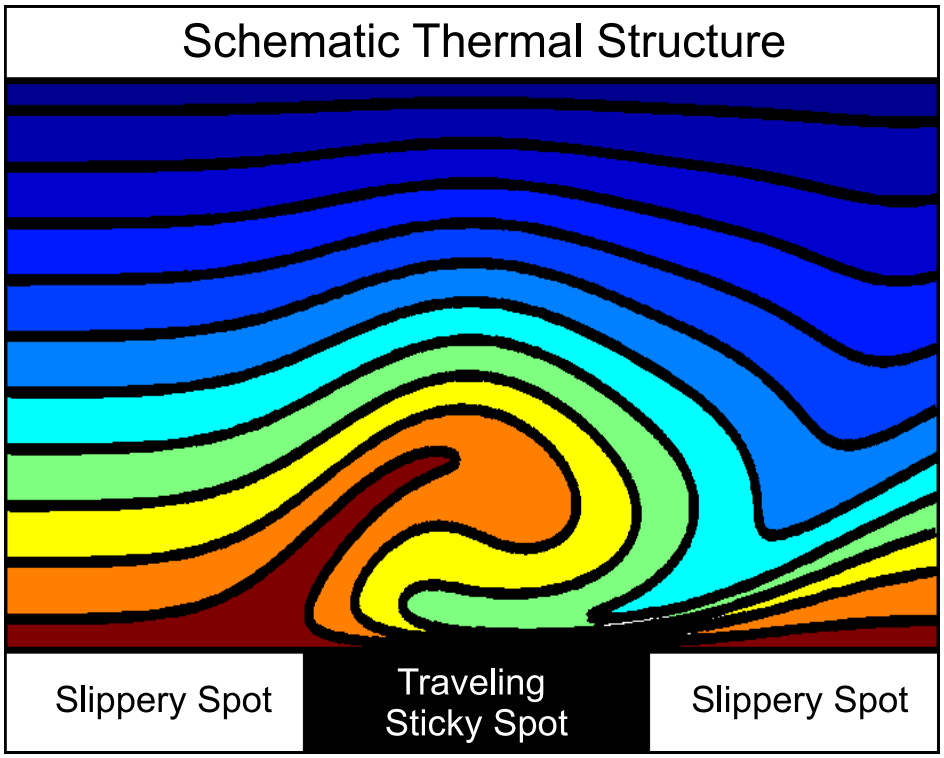

Figure 4.8: Schematic diagram showing the thermal structure produced by stratigraphic overturn. Initially horizontal isotherms are transported with the overturning ice and become overturned as well. Stratigraphic geometry used to define the schematic thermal structure taken from Figure 4.6e.

over diffusion and thermal overturn is possible. Boreholes drilled through actively overturning stratigraphic folds should measure a temperature inversion, with cold ice underneath warm ice in the lower third of the ice column.

Thermal overturn will reinforce a travelling sticky patch, creating a positive feedback. A cold downwelling limb of an overturning vortex reaches its lowest point above the middle of the sticky patch (Figure 4.8). This cold ice near the bed increases conductive cooling that promotes basal freeze-on, loss of basal water, and a reduction in sliding. This progression of processes allows a sticky patch to continuously dewater the bed as it travels downstream. Thermal overturn compliments the mechanism for downstream propagation described by *Wolovick et al.* (2014) and provides an explanation for how the patches strengthen over time.

Ice sheet temperature and the distribution of basal water are difficult to constrain. The most reliable results come from borehole measurements, but the distribution of these is extremely sparse. Indirect estimates of temperature in the upper part of the ice column may be made from measurements of radar attenuation rate (*MacGregor et al.*, 2015b). Basal water has been constrained by radar reflectivity estimates using column-average attenuation rates that often do not account for variable thermal structure (e.g., *Oswald and Gogineni*, 2008; *Wolovick et al.*, 2013; *Jacobel et al.*, 2010; *Carter et al.*, 2007), even though attenuation is highly sensitive to warm ice near the bed (*MacGregor et al.*, 2012; *Matsuoka*, 2011). Our model indicates that ice sheet thermal structure in the vicinity of overturned stratigraphic folds may be extremely complex, with warm attenuating ice high in the ice column. Folds

cause laterally and vertically variable attenuation in the ice column, making interpretation of both englacial and bed echoes more challenging.

4.5.2 Folding Timescale

The time required to produce an overturned fold above a travelling sticky patch impacts the distance the patch travels downstream while the ice is deforming. The time required to produce the fold also impacts the potential range of processes that could be expressed in the fold. The characteristic timescale t to produce a large overturned fold is proportional to the throughflow timescale for the sticky patch, $t \propto L/\bar{u}$. The constant of proportionality depends on the amplitude and geometry of the sticky patch as well as the specific distribution of velocity with depth. For an ice sheet 2-3 km thick, a sticky patch 5-10 ice thicknesses (10-30 km) long, and a column velocity of 1-100 m/yr, the characteristic timescale ranges between 100 and 30,000 years. In this time period, a sticky patch with $\hat{u}_p = 1$ will migrate 10-30 km downstream. The distance travelled is independent of $\bar{u}$ because the timescale is inversely related to column velocity. Changing the patch propagation velocity $\hat{u}_p$ will alter the distance travelled proportionally. The timescales and propagation distances are reasonable given the environment of the observed folds in northern Greenland.

4.5.3 Ice Cores

Near the center of ice sheets, ice cores show disturbances near the bed. Strong variations between isotope records from adjacent cores and the presence of flow microstructures suggest deformational processes (*Grootes et al.*, 1993; *Dahl-Jensen et al.*, 1997; *Faria et al.*, 2010; *Montagnat et al.*, 2014). Observations from the NEEM core in Greenland (*NEEM Community Members*, 2013) and the differences in the cores between the GRIP and GISP2 records (*Grootes et al.*, 1993) suggest folding. Along the ice divide in Greenland, there are rib-like variations in driving stress, suggesting variations in basal resistance (*Sergienko et al.*, 2014). These ribs could give rise to large overturned folds, but our mechanism alone cannot give the exact results seen at NEEM because two inverted sections are observed there without an intervening upright section. Our results are compatible with folds resulting from viscosity variations (*Dahl-Jensen et al.*, 1997) or steep topography (*Hindmarsh et al.*, 2006; *Gudmundsson*, 1997) as well as the presence of freeze on ice (*Bell et al.*, 2014, 2011; *Creyts et al.*, 2014). We expect all these processes to be active in the deep ice environment, and further work is necessary to understand their relative contributions in different regions.

4.5.4 Observational Constraints

The range of allowable parameter space for travelling sticky patches can be constrained by comparing model stratigraphic structures with observed stratigraphic structures. Overturned folds are always found nearer to the bed than the surface (*Bell et al.*, 2011, 2014; *MacGregor et al.*, 2015a), indicating that propagation velocity is less than regional surface velocity (Figure 4.4). The tops of the observed folds are usually less than half of the ice thickness (*Bell et al.*, 2014). The large example fold (Figure 4.1c) is approximately two-thirds of the ice thickness and represents the extreme high end of the range of observed overturned folds. This

upper limit is shown by the thick curved line in Figure 4.4a,c. All observed folds fall to the left of this curve, indicating that the sticky patches usually propagate at a velocity less than or equal to the ice column velocity. The uncertainty in the measurements of fold geometry allows for the possibility that the fastest sticky patches could propagate slightly faster than the column velocity (Figure 4.7f). Many of the observed folds have both distinct tops and distinct bottoms (*MacGregor et al.*, 2015a), implying that patch propagation velocity is in between far-field slip rate and far-field surface velocity.

Observations of the bottom boundaries of overturned folds are crucial for interpreting regional slip rates. Bottom observations are both difficult to acquire because of increasing radar attenuation and geometric spreading deeper in the ice sheet, and difficult to interpret due to the complexity of reflectors near the bed. The presence of reflectors beneath the overturned folds suggests that a lower throughflow is present. The presence of a lower throughflow implies that internal deformation is an important component of bulk ice flow in the region surrounding the folds.

4.6 Conclusions

Travelling sticky patches produce overturning vortices in the lower part of the ice sheet when viewed in a moving reference frame. The vortices produce overturned stratigraphic folds that rotate over time. Ice within overturning vortices is trapped above the moving sticky patch, allowing the thickness of the vortex to be calculated by mass conservation. The overturning vortices are largest when the patch moves downstream at the regional surface velocity. Travelling sticky patches can produce overturned folds at any elevation within the ice column, from the bed to the surface, although folds near the bed are more likely. As a result, measurements of the upper and lower boundaries of observed overturned folds can be used to constrain the parameter range of real travelling sticky patches. Three example folds were measured and all three could have been produced by sticky patches moving at a velocity between 0.5 and 1.0 times the ice column velocity. The presence of subhorizontal reflectors underneath many of the overturned folds implies that internal deformation is an important contributor to bulk ice flow in northern Greenland.

The kinematic model presented here suggests an inverted thermal structure can form near the bed underneath the overturned folds. Thermal overturn provides a positive feedback that can make a travelling sticky patch even stickier by bringing cold ice from mid-depths closer to the bed above the center of the sticky patch. The resulting conductive cooling produces freeze-on and loss of basal water. Thermal overturn results whenever the strata rotate faster than diffusion can erase their thermal structure. Recent work suggests that basal resistance may be concentrated in narrow ribs (*Sergienko and Hindmarsh*, 2013; *Sergienko et al.*, 2014), and thermal overturn provides a mechanism to keep the ribs cold and strong-bedded if they move downstream. *Wolovick et al.* (2014) explained how slippery and sticky patches can migrate downstream. This work illustrates how patches can strengthen over time and how a simple kinematic model can be used to understand observed folds in radar.

Chapter 5

Controls on the thickness of freeze-on units beneath large ice sheets

Michael J. Wolovick, Timothy T. Creyts, W. Roger Buck, Robin E. Bell

This chapter is in preparation for publication.

5.1 Abstract

Liquid water underneath ice sheets is crucial for controlling the coupling between the sliding ice and the bed. Freezing of this water to the base of the ice sheet can remove water and sediment from the subglacial environment, modify ice rheology, and increase basal drag. Recent ice-penetrating radar observations in Greenland and Antarctica have revealed large basal units potentially composed of freeze-on ice. These observations have raised the question of where freeze-on is likely to occur and of how much ice can be added by basal freezing. Here, we use a simple model of basal energy balance and ice flow to determine what conditions foster basal freeze-on and what thicknesses of freeze-on are likely to be produced. We compute freeze-on thickness as a function of thermal boundary conditions, ice sheet flow and geometry, and subglacial water flux. Conductive cooling is capable of producing freeze-on units up to two hundred meters thick when surface temperature is low ($\leq$ -45°C), ice thickness is small ($\leq$ 2500 m), and the overlying ice sheet moves slowly ($\leq$ 3 m/yr). Glaciohydraulic supercooling can produce freeze-on units over a thousand meters thick when surface and bed slopes are appropriately oriented and ample water flux is available to transport sensible heat downstream. Large freeze-on units produced by supercooling are most likely to be found in the ablation zone where water fluxes are high and surface slopes are steep. Observed basal units in East Antarctica are likely to have been produced by basal freeze-on, while basal units in the accumulation zone of northern Greenland are more likely to have been produced by an alternate mechanism, such as travelling slippery patches or rheological contrasts in the ice column. Around the margins of the former Northern Hemisphere ice sheets mountainous topography and overdeepenings likely hosted freeze-on units produced by supercooling.

5.2 Introduction

Large (100-1000m) basal structures have been imaged with ice-penetrating radar data from Antarctica (*Bell et al.*, 2011) and Greenland (*Bell et al.*, 2014; *MacGregor et al.*, 2015a). These structures were originally interpreted to result from the freeze-on of subglacial water (*Bell et al.*, 2011). Recently, we proposed that some of the structures in Greenland may have been formed from travelling slippery patches at the ice sheet base with only small volumes of freeze-on ice (*Wolovick et al.*, 2014). The *NEEM Community Members* (2013) proposed that the Greenland structures may have been formed by rheological contrasts between glacial and interglacial ice within the ice column. The size of englacial structures that can be produced by basal freeze-on and the environmental conditions where they will develop remain unknown. Here, we use a simple model to estimate the size of englacial structures that can be produced both by conductive freezing and by supercooling of flowing subglacial water. We then use this model to estimate where freeze-on is likely to happen based on known and inferred ice sheet boundary conditions.

Subglacial water freezes onto the overlying ice sheet when heat is removed from the bed either by conduction into the ice column (e.g. *Joughin et al.*, 2004a) or by supercooling of the flowing water (*Rothlisberger*, 1972; *Hooke*, 1991; *Lawson et al.*, 1998; *Alley et al.*, 1998; *Creyts and Clarke*, 2010; *Creyts et al.*, 2013). Freeze-on releases latent heat, warming and softening the overlying ice sheet. Freeze-on ice may also have a different crystal size and sediment content than meteoric ice (*Jouzel et al.*, 1999), and hence a different rheology. If a large fraction of the ice column is composed of freeze-on ice, the different properties of freeze-on ice will be reflected in the flow of the overall ice sheet. Freeze-on removes water from the subglacial hydrologic system, modifying the traction between the sliding ice and the bed and potentially causing ice stream shutdown (*Bougamont et al.*, 2003).

We use an idealized numerical model to investigate the boundary conditions and glaciological parameters that control the distribution and size of basal freeze-on structures. This analysis will enable us to determine which of the observed basal units can be attributed to basal freeze-on rather than travelling slip patches or englacial rheological contrasts. By considering the control that water flux has on the size and distribution of basal freeze-on, we can gain insights into the subglacial hydrologic system.

5.3 Methods

We use a simple model to estimate freezing rate from local thermal forcing and upstream water supply. Once we know the freezing rate, we estimate the steady-state thickness of the freeze-on unit based on the flux of meteoric ice from local accumulation and horizontal transport, the partitioning of ice flow between basal slip and internal deformation, and cross-flow divergence.

We consider water flow that occurs in an area-averaged thin layer flowing along the basal plane. Local heterogeneities in bed topography, sediment coverage, and water distribution ensure that the ice sheet experiences drag as it slides over the bed and does not float. As our analysis is focused on lengthscales of an ice thickness or greater, we use an area-averaged approach to local heterogeneity in the basal hydrologic system. We represent the basal

hydrologic system as an equivalent area-averaged sheet flow and consider the contributions of that equivalent sheet flow to the energy budget of the basal plane. This treatment of basal hydrology, where the water system is parameterized in terms of a water layer thickness and a water velocity, is common in larger-scale ice sheet models (e.g. *Le Brocq et al.*, 2009; *Sergienko and Hulbe*, 2011; *Aschwanden et al.*, 2012). An equivalent sheet-flow treatment is appropriate when the temporal and spatial scales we are interested in are the scales of the overlying ice sheet.

The freezing rate at the base of an ice sheet is determined by the heat fluxes into and out of the basal plane. Conduction and supercooling act to cool the bed and promote freeze-on. Conductive cooling is caused by the decrease of temperature from the bed into the ice column. Supercooling is caused by changes in the pressure-dependent melting point of flowing subglacial water. Supercooling occurs when water flows towards lower pressure where the melting point rises. This liquid water is now below the melting point, and some of this water freezes. The latent heat that is released by freezing warms the remaining water up to the new melting point. The residual warmer water transports that heat away from the freezing zone.

The processes that warm the bed are shear heating of the sliding ice, geothermal flux, and viscous dissipation in the water system. Shear heating occurs when the drag of ice sliding over the bed converts gravitational potential energy into heat. Similarly, viscous dissipation arises from the energy released as water flows towards lower hydraulic potential. Geothermal flux results partly from radiogenic heating in the crust and mantle and partly from secular cooling of the Earth's interior. Latent heat that is released by freezing or absorbed by melting closes the basal thermal budget when water is available. When insufficient water is available to close the basal energy balance by freezing, the basal temperature drops below the melting point. This reduction in basal temperature reduces the conductive heat flux into the overlying ice sheet until energy balance is achieved.

To compute freeze-on thickness from freezing rate, we consider ice flow in a closed volume corresponding to a steady-state ice sheet above the freezing region. The ambient ice flow regime affects the thickness of a freeze-on layer that forms at the bottom of this volume by varying the flux of meteoric ice crossing the boundaries: horizontal flow enters the upstream margin, surface accumulation enters the top margin, cross-flow convergence enters the side margins, while basal freeze-on enters through the bottom margin. The entire package of meteoric and freeze-on ice exits the downstream margin, where the thickness of the freeze-on component is determined by comparing the volume of freeze-on ice with the volume of meteoric ice. We also consider how the partitioning of ice flow between sliding and internal deformation modifies the thickness of the freeze-on unit. This closed-volume integral treatment of mass conservation is equivalent to a local differential approach because of Gauss's Theorem. We choose this approach because freeze-on thickness is determined by the integrated volume of freeze-on ice added as the ice flows over the freezing zone, rather than the local freezing rate at any given point. While the cross-flow width of the freezing zone cancels out of the expression for thickness (Equation 5.12), the along-flow length remains an important free parameter. We explore the influence of freezing zone length in Section 5.4.5.

5.3.1 Heat Fluxes

Conductive Heat Flux

We estimate conductive heat flux using a steady-state one-dimensional vertical model of advection and diffusion. This model should capture the first-order influences of surface climate and ice thickness on conductive heat flow. The thermal structure of the ice sheet is given by,

$$\kappa \frac{\partial^2 T}{\partial z^2} - w \frac{\partial T}{\partial z} = 0 \tag{5.1}$$

where κ is thermal diffusivity, T is temperature, w is vertical velocity, and z is the vertical coordinate, with 0 being the ice base and D being the surface. The boundary conditions are that temperature equals the surface temperature, T_s, at z=D, and the pressure-dependent melting point, T_m, at z=0. Vertical velocity is determined by the surface accumulation rate, a, and a dimensionless shape function defined by $\hat{w} \equiv -w/a$. The minus sign indicates that positive surface accumulation produces downward flow within the ice sheet. If we define normalized temperature to be $\theta \equiv (T - T_s)/(T_m - T_s)$, normalized vertical coordinate to be $\hat{z} \equiv z/D$, and the Peclet number to be $P_e \equiv aD/\kappa$, then Equation 5.1 reduces to the dimensionless form,

$$\frac{\partial^2 \theta}{\partial \hat{z}^2} - P_e \hat{w} \frac{\partial \theta}{\partial \hat{z}} = 0. \tag{5.2}$$

The only remaining unknown is the distribution of velocity with depth, given by $\hat{w}$. We approximate the velocity field using a linear superposition of sliding and internal deformation (*Wolovick and Creyts*, 2015, in review), resulting in vertical velocity given by[1],

$$\hat{w}(\hat{z}) = \frac{1 - \hat{u}_b}{n+1}(1 - \hat{z})^{n+2} + \left(\hat{u}_b + (1 - \hat{u}_b)\frac{n+2}{n+1} \right) \hat{z} - \frac{1 - \hat{u}_b}{n+1} \tag{5.3}$$

where $\hat{u}_b \equiv u_b/\bar{u}$ is the fraction of ice flow due to basal sliding and n is the rheological exponent of ice, taken to be 3 by convention (*Cuffey and Paterson*, 2010). When ice flow is by basal sliding ($\hat{u}_b = 1$), then vertical strain rate is constant and vertical velocity varies linearly from the bed to the surface. When ice flow is by internal deformation ($\hat{u}_b = 0$), then vertical strain rate is lower near the bed than near the surface, and the profile of vertical velocity is curved (Figure 5.1a).

Once $\hat{w}$ is known, we solve Equation 5.2 numerically to determine the temperature profile (Figure 5.1b). The normalized conductive heat flux, $\hat{Q} = \partial\theta/\partial\hat{z}$, is determined by evaluating the temperature gradient at the bed. The conductive heat flux is determined by $Q_{cond} = \hat{Q}Q_0$, where $Q_0 \equiv k(T_m - T_s)/D$ is the fundamental conductive flux. Basal heat flux increases with increasing Peclet number for both basal slip and internal deformation velocity profiles (Figure 5.1c). As the Peclet number rises, increasing surface accumulation pushes cold surface temperatures deeper into the ice sheet, steepening the basal temperature gradient. When the Peclet number is negative (indicating surface ablation), vertical advection is upwards, pushing warm basal temperatures higher into the ice column and creating a nearly isothermal layer near the bed that reduces conductive heat flow.

[1] This is the "background vertical flow" in Equation 4.6.

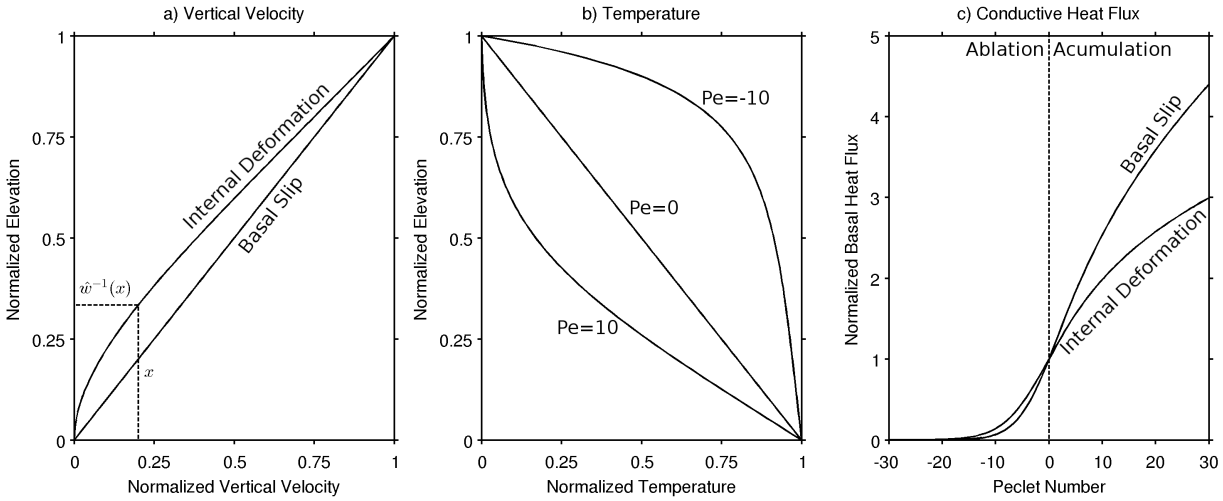

Figure 5.1: Thermal Model. a) Normalized vertical velocity ($\hat{w}$) as a function of normalized elevation ($\hat{z}$). b) Normalized temperature (θ) at several values of Peclet number (P_e). c) Normalized basal heat flow ($\hat{Q}$) as a function of Peclet number. Negative values of Peclet number represent surface ablation. Vertical velocity can be redimensionalized by multiplying by the negative accumulation rate ($-a$), elevation can be redimensionalized by multiplying by the ice thickness (D), temperature can be redimensionalized by pinning the top to the surface temperature and the bottom to the melting point, and heat flow can be redimensionalized by multiplying by the fundamental conductive flux, $Q_0 = k(T_m - T_s)/D$. Panel (a) also shows the inverse function $\hat{w}^{-1}$.

Supercooling

The melting point of water is dependent on pressure. As subglacial water flows along a pressure gradient the melting point changes, resulting in liquid water that is either above or below the melting point. If water is above the melting point, there is excess sensible heat available to melt ice. If water is below the melting point, it is in a supercooled state and some of the water must freeze. The freezing water releases latent heat that warms the remaining liquid water until the new melting point is reached. This phenomenon is called "glaciohydraulic supercooling" (*Rothlisberger*, 1972; *Lawson et al.*, 1998; *Alley et al.*, 1998; *Creyts and Clarke*, 2010; *Creyts et al.*, 2013). The supercooling heat flux is given by,

$$Q_{sc} = \rho_w c_p \beta \vec{\phi}_{water} \cdot \nabla P \tag{5.4}$$

where $\vec{\phi}_{water}$ is the specific water flux per unit cross-flow width, ρ_w is the density of water, c_p is the specific heat of water at constant pressure, P is water pressure, and β is the pressure coefficient of the melting point. $\vec{\phi}_{water}$ is equivalent to the product of area-averaged water layer thickness with area-averaged water velocity.

Viscous Dissipation

Heating from viscous dissipation occurs when water flows down the hydraulic potential gradient, converting potential energy into heat. The viscous dissipation term is given by,

$$Q_{visc} = \vec{\phi}_{water} \cdot \nabla \Phi \tag{5.5}$$

where Φ is hydraulic potential. Hydraulic potential is given by the sum of gravitational potential and pressure potential, $\Phi = \rho_w g B + P$, where B is bed elevation. Pressure is approximated by the hydrostatic pressure of the ice overburden, $P = \rho_i g D = \rho_i g (S - B)$. We neglect effective pressure in this analysis. We make the assumption that water flow and ice flow are co-directional so that the vector water flux $\vec{\phi}_{water}$ can be replaced with water flux magnitude, ϕ_{water}. We represent the gradient of bed elevation in terms of the ratio to the gradient in surface elevation, B'/S', where the bed gradient is evaluated along the direction of flow. Positive values of B'/S' indicate that the bed is sloping downwards in the direction of flow, while negative values indicate backsloping conditions where the bed rises out of an overdeepening.

Because supercooling and viscous dissipation are both proportional to the subglacial water flux, we group them together into a net hydrologic heating term. The net hydrologic heating is,

$$Q_{hydro} = \rho_i g \phi_{water} S' \left[1 + \frac{\Delta\rho}{\rho_i} \frac{B'}{S'} + \rho_w c_p \beta \left(\frac{B'}{S'} - 1 \right) \right] \tag{5.6}$$

where $\Delta\rho = \rho_w - \rho_i$ is the density difference between water and ice. Q_{hydro} is defined to be positive when the hydrologic system is adding heat to the basal plane, promoting melting. Because water flux and surface slope are always positive, the sign of Q_{hydro} is determined by the bed/surface slope ratio. Setting $Q_{hydro} = 0$, we can solve for a critical slope ratio at which supercooling overcomes viscous dissipation in the water system. The supercoooling threshold is (*Rothlisberger and Lang*, 1987; *Alley et al.*, 1998; *Creyts and Clarke*, 2010),

$$\frac{B'}{S'} = \frac{\rho_w c_p \beta - 1}{\rho_w c_p \beta + \Delta\rho / \rho_i} \approx -1.7. \tag{5.7}$$

When bed slopes are more steeply backsloping than this ratio the basal plane will be cooled by the hydrologic system, and when bed slopes are above this ratio the basal plane will be heated by the hydrologic system.

Shear Heat

As the ice sheet slides over its bed, friction turns gravitational potential energy into heat. The rate of shear heating, Q_{shear}, is given by the product of slip rate, u_b, and basal drag, τ_b,

$$Q_{shear} = \tau_b u_b. \tag{5.8}$$

We approximate basal drag from the surface driving stress, giving $\tau_b = \rho_i g D S'$. We assume that all shear heating within the ice column warms the bed and we replace sliding velocity with column-averaged velocity, $\bar{u}$.

Geothermal Flux

Geothermal flux, Q_{geo} is one of the least well-constrained boundary conditions for modern ice sheets. Direct observations of geothermal flux require thermal measurements from boreholes drilled nearly to the bed. These observations are far too sparse to produce reliable

large-scale heat flow maps. All existing large-scale estimates of geothermal flux rely on indirect inferences from seismic tomography or satellite magnetic data with a resolution on the order of several hundred kilometers (*Shapiro and Ritzwoller*, 2004; *Maule et al.*, 2005). Measurements of geothermal flux on non-glaciated terrain indicate that geothermal flux varies substantially on much smaller distances due to shallow hydrothermal circulation, magmatic history, variations in rock type, and heterogeneities in the distribution of radioactive elements (*Waddington*, 1987; *Jaupart and Mareschal*, 2007). Temporal variations in geothermal flux occur because of the diffusive response of the rock to climatic transients in the overlying ice sheet (*Waddington*, 1987). We discuss the values of geothermal flux that we investigate in Section 5.3.4.

5.3.2 Freezing Rate

The freezing rate is determined by the energy balance of the basal plane. The freezing rate is given by,

$$f = -\left(\frac{Q_{geo} + Q_{shear} + Q_{hydro} - Q_{cond}}{\rho_i L}\right) \tag{5.9}$$

where L is latent heat. Equation 5.9 is equivalent to equation S9 of *Wolovick et al.* (2014), with melting rate replaced by freezing rate and isolated on the left-hand side[2]. Equation 5.9 is also equivalent to Equation 4 of *Sergienko and Hulbe* (2011), although *Sergienko and Hulbe* (2011) do not include the hydrologic heating terms. While *Sergienko and Hulbe* (2011) make the assumption that geothermal heat delivered to the base of the water layer cannot be used to melt the overlying ice, we assume that it can. The freezing rate also limits the length of the freezing zone when water flux is low. We discuss the water supply limitation for freezing zone length in Section 5.3.4.

5.3.3 Freeze-on Thickness

We compute the thickness of the freeze-on structure by comparing the flux of freeze-on ice with the flux of meteoric ice. We consider a stationary zone of basal freeze-on with freezing rate f (Figure 5.2). The freezing zone has an along-flow length l, an across-flow width W, an ice thickness D, a column-average velocity $\bar{u}$, and a surface accumulation rate a. The total flux of meteoric ice entering the domain is given by,

$$\phi_{met} = \bar{u}DW - DlW\dot{\epsilon}_{yy} + lWa \tag{5.10}$$

where $\dot{\epsilon}_{yy} = \partial v/\partial y$ is the cross-flow strain rate. The column-average velocity $\bar{u}$ is defined at the upstream margin of the domain. We assume that all ice entering or exiting the cross-flow boundaries of the domain is meteoric ice.

By comparison, the total flux of accreted ice entering the domain is given by,

$$\phi_{acc} = lWf. \tag{5.11}$$

[2]Equation 3.9 in this thesis.

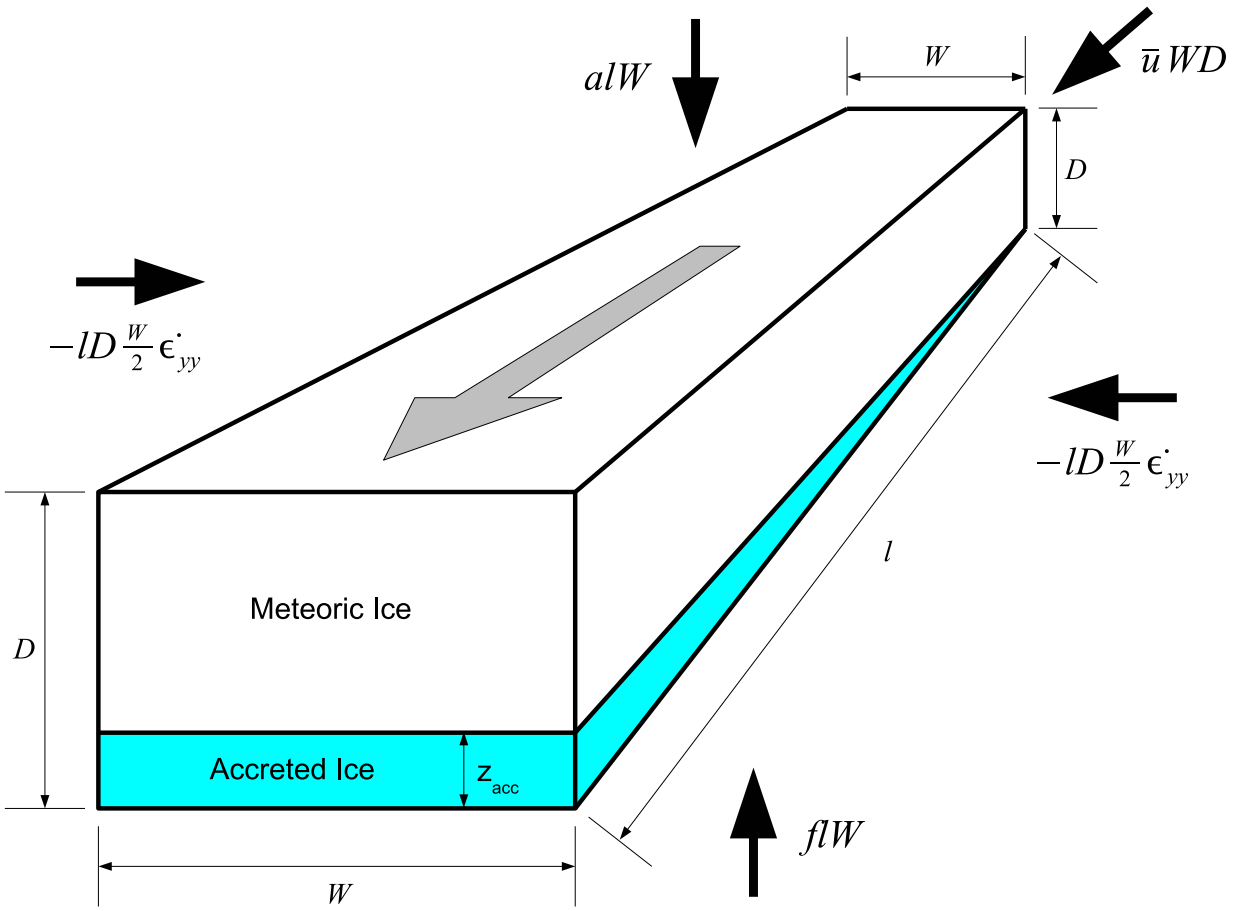

Figure 5.2: Model domain for calculating the thickness of accretion ice, z_{acc}. Black arrows around the outside of the domain show inwards flux of ice from horizontal flow, surface accumulation, cross-flow divergence, and basal freeze-on.

Both the meteoric and the accreted ice flux must leave through the downstream margin of the domain. The thickness of the freeze-on unit at the downstream margin is determined by the distribution of ice flux with depth. If the ice is flowing uniformly by basal sliding, then the accretion thickness is given by the ratio of accreted ice flux to total ice flux. If internal deformation produces an ice flow profile that is not uniform with depth, then the accretion thickness is given by the point at which the fraction of ice flux passing under that elevation is equal to the fraction of ice flux composed of accreted ice. The fraction of ice flux passing underneath a given elevation is equal to $\hat{w}$, the normalized vertical velocity used earlier (Section 5.3.1). Therefore, the thickness of the accretion unit is given by the inverse of vertical velocity, $\hat{z} = \hat{w}^{-1}(x)$ (Figure 5.1a). The normalized thickness of the accretion unit is given by,

$$\hat{z}_{acc} = \hat{w}^{-1}\left(\frac{\phi_{acc}}{\phi_{met} + \phi_{acc}}\right) = \hat{w}^{-1}\left(\frac{lf}{\bar{u}D - Dl\dot{\epsilon}_{yy} + l(a+f)}\right). \tag{5.12}$$

The cross-flow width of the freezing zone cancels out of the expression for freeze-on thickness but the along-flow length does not. Once the normalized thickness of the accretion

unit is known, the thickness is calculated by multiplying by the ice thickness, $z_{acc} = \hat{z}_{acc} D$.

5.3.4 Parameter Choices

Our model incorporates a broad range of factors that control the thickness of freeze-on units, including thermal boundary conditions, ice sheet geometry, subglacial water availability, and ice flow conditions. There are 11 total input parameters in our model: surface temperature, T_s, surface accumulation rate, a, ice thickness, D, geothermal flux, Q_{geo}, column-average ice velocity, $\bar{u}$, water flux, ϕ_{water}, surface slope, S', bed/surface slope ratio, B'/S', basal slip fraction, $\hat{u}_b$, freezing zone length, l, and cross-flow divergence, $\dot{\epsilon}_{yy}$. We identify three parameter combinations to represent the three main regions where basal structures are observed. These regions are the high East Antarctic plateau (*Bell et al.*, 2011), the interior (accumulation zone) of northern Greenland (*Bell et al.*, 2014), and the margins (ablation zone) of Greenland (*Bell et al.*, 2014). Below, we explore the effects of varying key two-dimensional slices through parameter space, with the other parameters held constant.

Surface Climate

Surface temperature over the modern ice sheets ranges between approximately -60 °C and 0 °C (*Comiso*, 2000; *Noel et al.*, 2015). Accumulation rate varies between a few centimeters per year and over a meter per year, while annually averaged ablation rate varies from zero to several meters per year (*Van de Berg et al.*, 2005; *Arthern et al.*, 2006; *Noel et al.*, 2015). For the East Antarctic plateau, we choose values of -50 °C and 5 cm/yr (*Comiso*, 2000; *Van de Berg et al.*, 2005; *Arthern et al.*, 2006). For the interior of northern Greenland, we choose -28 °C and 12 cm/yr (*Noel et al.*, 2015). For the Greenland ablation zone, we choose values of -5 °C and -30 cm/yr (*Noel et al.*, 2015), with negative values of accumulation indicating surface ablation.

High accumulation rates are never found together with cold surface temperatures (Figure 5.3). The moisture capacity of air has roughly an exponential dependence on temperature according to the Clausius-Clapeyron relationship. When surface temperature and accumulation rate are plotted against one another on semi-logarithmic axes, the upper margin of the observed climate forcing forms roughly a straight line. We manually fit a line with an e-folding temperature of 12.5 $°C$ to the upper envelope of the observed distribution (Figure 5.3). We use this line to represent the maximum observed accumulation as a function of temperature.

Geothermal Flux

Globally, continental crust averages a geothermal flux of 65 mW/m^2 (*Jaupart and Mareschal*, 2007). Cold continental cratons, such as East Antarctica, average 40-50 mW/m^2 based on *in situ* measurements (*Jaupart and Mareschal*, 2007, Table 3). Remote inferences of East Antarctic geothermal flux are also within the range of 40-50 mW/m^2 (*Shapiro and Ritzwoller*, 2004; *Maule et al.*, 2005). Within individual cratons, heat flux may vary by 20-30 mW/m^2 (*Jaupart and Mareschal*, 2007, Table 4). Tectonically and volcanically active regions, such

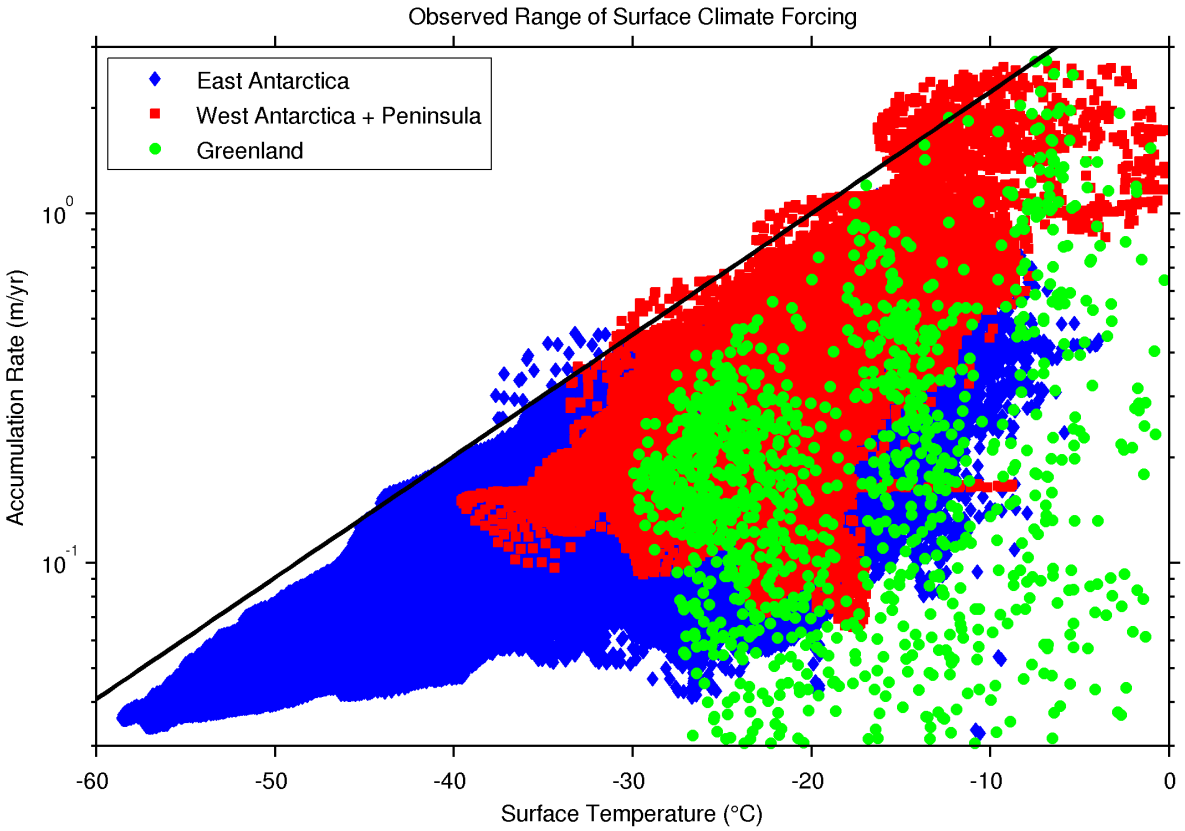

Figure 5.3: Observed distribution of surface temperature and accumulation rate for Antarctica and Greenland. The black line represents an approximate upper limit of surface accumulation as a function of temperature. The slope corresponds to an e-folding temperature of 12.5 °C. For Antarctica, surface temperature is taken from *Comiso* (2000), and surface accumulation is the mean of *Van de Berg et al.* (2005) and *Arthern et al.* (2006), all accessed via the ALBMAPv1 dataset (*Le Brocq et al.*, 2010). For Greenland, surface temperature and accumulation are both taken from RACMO2.3 (*Noel et al.*, 2015).

as West Antarctica, may have higher heat flows well in excess of 100 mW/m^2 *Jaupart and Mareschal* (2007). Preliminary heat flow estimates at the WAIS Divide ice core suggest that heat flow may be as high as 240 mW/m^2 in central West Antarctica (*Clow et al.*, 2012). As regions with high heat flow are unlikely to host basal freeze-on, we investigate a central value of 40 mW/m^2 and a range of 30-100 mW/m^2.

Ice Sheet Geometry

Ice thickness in the Gamburtsev Subglacial Mountains, where many of the East Antarctic basal structures have been observed, ranges from 1000 m to over 4000 m (*Bell et al.*, 2011; *Ferraccioli et al.*, 2011). Many of the structures, interpreted as freeze-on, originate where water networks terminate in ice that is ∼2200 m thick (*Creyts et al.*, 2014). We choose 2500 m as a central value for the East Antarctic parameter set, and investigate a range of 1000-4500 m. We choose 2200 m as the central value for the interior Greenland parameter set, and investigate the same range. We choose 1000 m as the ice thickness for the Greenland ablation zone parameter set.

Ice sheet surface slopes are typically in the range of 10^{-4}-10^{-2} (e.g. *Fretwell et al.*, 2013). Slopes are generally higher towards the margins, although substantial local variability exists throughout the ice sheet. East Antarctica has a generally lower slope than northern Greenland. We choose a central value of 10^{-3} for East Antarctica and 3x10^{-3} for both the interior and the margins of Greenland, with a range of 10^{-4}-10^{-2} for all three sets.

The range of bed to surface slope ratio that we consider is limited by the ability of water to flow uphill. Water cannot flow up an adverse bed slope steeper than $-\rho_i/\Delta\rho = -11$ times the surface slope. We investigate a range of bed/surface slope ratios of -10 to 10. To ensure that we are investigating a moderate supercooling geometry, we choose a central value of -5 for the bed/surface slope ratio in all parameter sets.

Water Flux

Our model uses specific water flux, with units of m^2/yr. Studies of subglacial and supraglacial water flows often use volume flux, with units of m^3/yr. Specific flux is volume flux distributed across the cross-flow width of the freezing zone; equivalently, it is also the product of area-averaged water layer thickness with area-averaged water velocity. The specific flux is given by,

$$\phi_{water} = \frac{mA}{W} \tag{5.13}$$

where m is the average upstream melt rate, A is the catchment area, and W is the cross-flow width of the freezing region. Observations indicate that basal units are in the range of 5-20 km in the cross-flow dimension (*Bell et al.*, 2011, 2014). For our model, we choose a range of specific water flux between 10^0-10^6 m^2/yr. This range captures the full spectrum of freeze-on dynamics, from water-limited conductive cooling, through conduction-limited freeze-on, to water-dominated supercooling (Section 5.4.3). We choose the geometric mean of this range, 10^3 m^2/yr, as the central value for both accumulation zone parameter sets. We choose a high value, 10^5 m^2/yr, as the central value for the ablation zone to ensure that we are in the supercooling regime and because the ablation zone has abundant surface melt. In the discussion (Section 5.5.3), we compare this range of specific water flux with observations of volume fluxes underneath Antarctica and Greenland.

Ice Flow Regime

Ice sheet surface velocities range from zero to over 10 km/yr (*Joughin et al.*, 2010; *Rignot et al.*, 2011). Thick freeze-on units are more likely to be found where ice velocities are low (Section 5.4.4). Near Dome A in East Antarctica, ice velocity measured by GPS at the AGAP-S camp was 1.7 m/yr (*Bell et al.*, 2011). In Greenland, many of the marginal units are found in slow-flowing ridges between fast-flowing outlet glaciers (*Bell et al.*, 2014), while the interior units are located where ice flow is of order 10 m/yr. We choose a range of 0.3-3000 m/yr for ice velocity with a central value of 1 m/yr in East Antarctica and 10 m/yr in the both Greenland parameter sets.

Basal slip ratio, $\hat{u}_b$, varies between 0 and 1 by definition. We choose a central value of 0 for both the accumulation zone and the ablation zone because the observed basal structures

are more likely to develop in slow-flowing regions where ice flow is dominated by internal deformation.

Cross-flow divergence varies depending on the geometry of the surrounding ice sheet. When flow is away from a dome or along a ridge, the ice will be spreading in the cross-flow dimension. When flow is becoming concentrated into an ice stream, the ice will by converging in the cross-flow dimension (*Ng and Conway*, 2004). In the simple case of flow diverging around a circular dome, cross-flow divergence is equal to half the vertical strain rate, a/D (*Nye*, 1959; *Reeh*, 1989). We scale the cross-flow divergence with the vertical strain rate, a/D. With that scaling, we investigate a range of +1 to -1 and a central value of zero.

Length

The along-flow length of the freezing region is determined by heterogeneity in basal topography, geothermal flux, and other forcings. We choose lengths based on the observed dimensions of the basal structures. The observed structures are on the order of 10-100 km long, although part of that length results from passive advection away from the source (*Bell et al.*, 2011, 2014). We choose a central value of 20 km for both accumulation zone sets, 10 km for the ablation zone set, and examined a range of 0-50 km.

Along-flow length can also be limited by the available water supply. When water supply is low, length is limited to,

$$l \leq \frac{\rho_w \phi_{water}}{\rho_i f}. \tag{5.14}$$

If water supply is low enough to limit the possible length of the freezing zone, we replace the assumed length in Equation 5.12 with the water-limited length.

5.4 Results

We use the simple model described above to examine the range of conditions that give rise to basal freeze-on and to explore the parameters that control freeze-on thickness. First, we explore how conductive cooling is affected by surface temperature and accumulation, ice thickness, and geothermal flux. Second, we analyze supercooling in the ablation zone. Third, we investigate how increasing water flux causes the freezing system to switch between water-limited, conduction-limited, and water-dominated regimes. Next, we explore the influence of the ice flow regime on the freeze-on units produced by both conductive cooling and supercooling. Finally, we examine how the lengthscale of the freezing region modifies the thickness of the resulting freeze-on unit.

5.4.1 Conduction

Our model results indicate that conductive cooling can create freeze-on units up to 100-200m thick in the accumulation zone (Figure 5.4). In the following sections we explore the effects of surface temperature, accumulation rate, ice thickness, and geothermal flux on conductive freeze-on.

Surface Temperature

Surface temperature has a simple monotonic effect on the size of freeze-on units. Colder temperatures always produce thicker freeze-on (Figure 5.4a,c). The effect of surface temperature is monotonic because surface temperature only enters the problem once, by controlling the conductive heat flux off of the bed. The fundamental conductive heat flux, $Q_0 = k(T_m - T_s)/D$, increases linearly with decreasing surface temperature.

Surface Accumulation Rate

Surface accumulation rate affects the size of basal freeze-on units in two ways, by modifying both the conductive heat losses and the flux of meteoric ice. Increasing surface accumulation increases the downwards advection of cold ice and the conductive heat losses from the bed (Figure 5.1). Increasing surface accumulation also increases vertical thinning within the ice column, pushing freeze-on units downwards. The thinning effect of surface accumulation is represented in our model by an increasing flux of meteoric ice entering the domain (Figure 5.2), reducing the fraction of total ice flux composed of freeze-on ice.

The thermal effect of accumulation dominates at all of the observed temperature/accumulation combinations (Figure 5.4a,c). At any given surface temperature, there is a value of surface accumulation that will produce the thickest conductive freeze-on unit, with smaller units found above and below that level. However, the "sweet spot" is higher than the observed

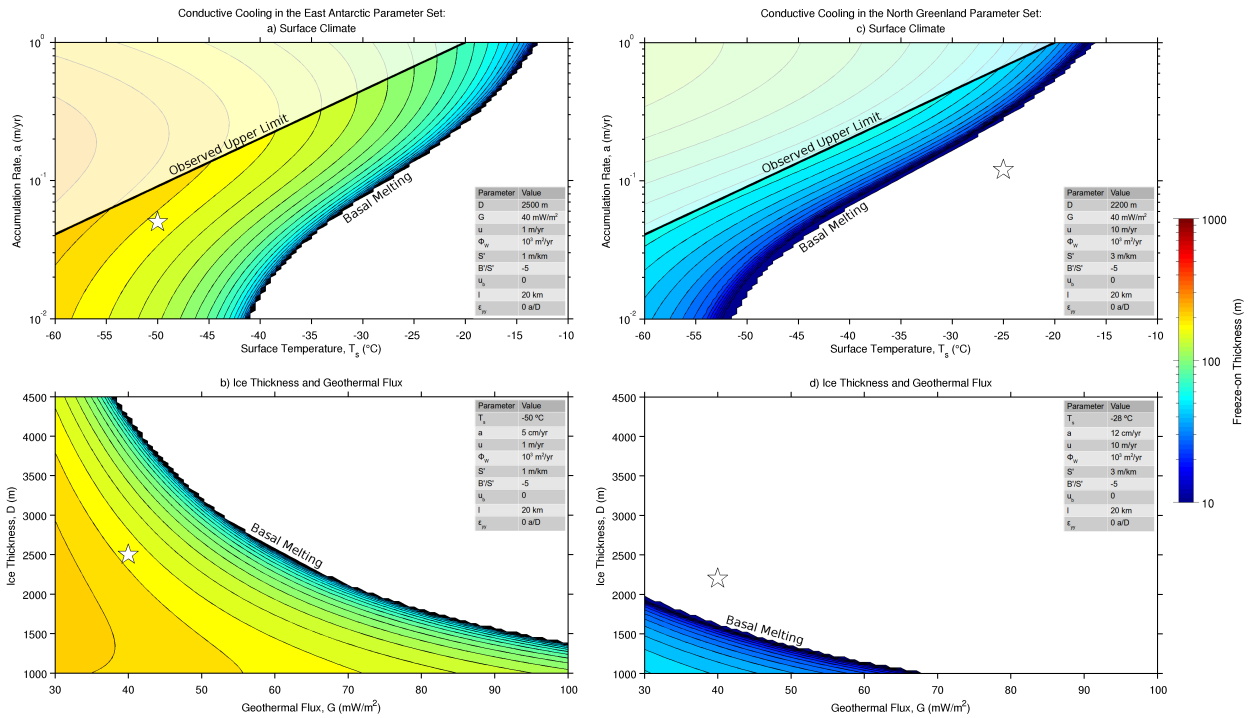

Figure 5.4: Freeze-on thickness, z_{acc}, as a function of (a,c) surface temperature and accumulation rate, and (b,d) ice thickness and geothermal flux. The observed upper limit of accumulation as a function of temperature (Figure 5.3) is shown in (a) and (c), and model output above that line is set partially transparent. Left column represents the East Antarctic parameter set and right column represents the North Greenland parameter set. White stars indicate the parameter combinations used for the other accumulation zone figures.

upper limit of accumulation rate as a function of temperature. For example, at -60 °C in the East Antarctic parameter set the largest freeze-on units are found when accumulation is roughly 20 cm/yr, but the highest observed accumulation rate at that temperature is only 4 cm/yr. Within the observed range of accumulation as a function of surface temperature, increased surface accumulation always produces a larger conductive freeze-on structure.

Geothermal Flux

Geothermal flux affects the system in one way, by changing the balance of heat flows at the bed. Increasing geothermal flux warms the bed, reducing the freezing rate and eventually causing basal melting. As a result, freeze-on thickness monotonically decreases for increasing geothermal flux (Figure 5.4b,d).

Ice Thickness

Ice thickness affects basal freeze-on in multiple ways. Increasing ice thickness reduces the conductive heat flux by reducing the thermal gradient, $Q_0 = k(T_m - T_s)/D$. Ice thickness also increases the Peclet number, $P_e = aD/\kappa$, increasing the dominance of advection over diffusion and increasing the conductive heat flux. A larger ice thickness increases the flux of meteoric ice entering the domain from upstream (Figure 5.2), as well as increasing the driving stress and shear heating. Finally, ice thickness controls the overall scale of all englacial structures by affecting the conversion of normalized thickness ($\hat{z}_{acc}$) to thickness (z_{acc}).

The impact of ice thickness on the fundamental conductive flux ($Q_0 = k(T_m - T_s)/D$) dominates. For most of the parameter range that we consider, increasing ice thickness reduces the conductive heat flux off of the bed and reduces the thickness of the freeze-on unit (Figure 5.4b,d). Only when ice thickness and geothermal flux are both small in the East Antarctic parameter set does thicker ice leads to thicker conductive freeze-on units.

5.4.2 Glaciohydraulic Supercooling

Glaciohydraulic supercooling is dependent on subglacial water flow to remove latent heat from the freezing region. The net hydrologic heat flux, Q_{hydro}, depends on water flux, surface slope, and bed/surface slope ratio.

In the ablation zone, surface temperatures are warm and advection within the ice column is upwards. Conductive heat losses are negligible (Figure 5.1c). As a result, freeze-on in the ablation zone requires supercooling. Freeze-on occurs when water flux is high, surface slope is steep, and the bed is steeply backsloping (Figure 5.5). In those conditions, supercooling is capable of producing very thick freeze-on units. If water flux is too low, if the bed slope is not appropriately oriented, or if surface slope is shallow, then the ice sheet will be melting at the base.

5.4.3 Water Flow

In the ablation zone, freeze-on is dominated by the ability of the hydrologic system to remove heat via supercooling. In the accumulation zone, basal freeze-on can be divided into three

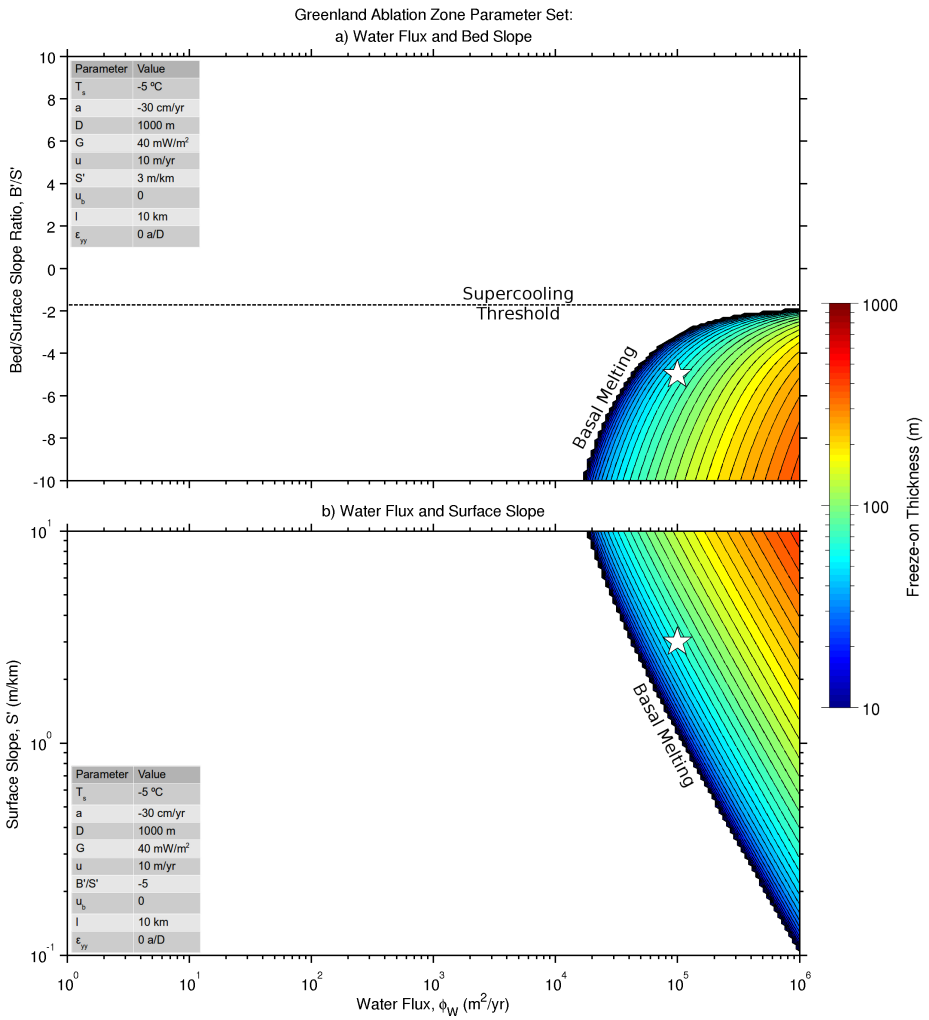

Figure 5.5: Supercooling freeze-on thickness in the ablation zone. Thickness as a function of (a) water flux and bed/surface slope ratio, and (b) water flux and surface slope. The bed slope threshold for supercooling (Equation 5.7) is shown in (a). The white star represents the parameter combinations used for the other ablation zone figures. Those parameter combinations are chosen to be within the supercooling regime.

regimes based on the subglacial water flux: water-limited, conduction-limited, and water-dominated (Figure 5.6).

Water-Limited Regime

In the water-limited regime, all of the subglacial water is removed from the hydrologic system by conductive freezing. Our model represents the water supply limitation by reducing the along-flow length of the freezing region (Equation 5.14). The downstream margin of the freezing zone in this regime is a freezing front, a line where the water supply is used up, the water system seals off, and hydraulic conductivity drops to zero. Downstream of the freezing front basal temperature drops below the melting point and sliding ceases. The water-limited regime begins when water flux is in between 10^1 and 10^2 m^2/yr in our model (Figure 5.6).

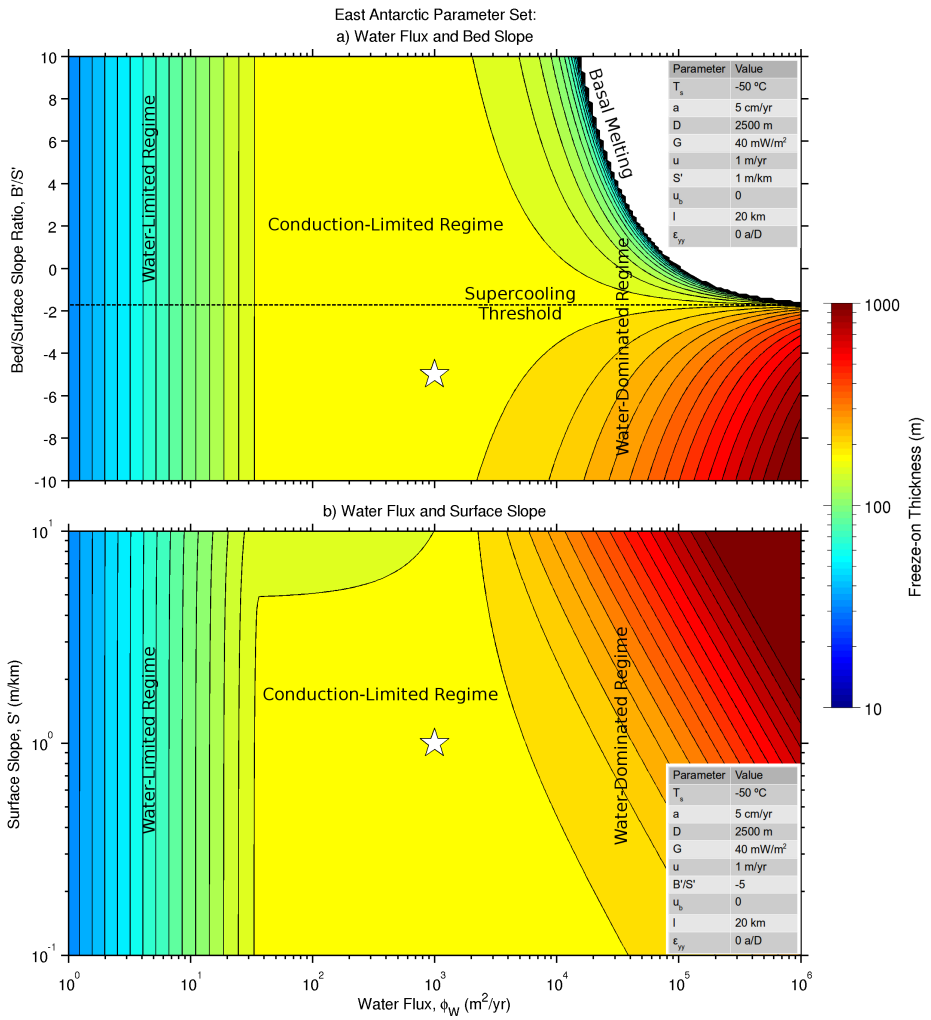

Figure 5.6: Freeze-on thickness as a function of water flux in the accumulation zone. Thickness as a function of (a) water flux and bed/surface slope ratio, and (b) water flux and surface slope. The bed slope threshold for supercooling (Equation 5.7) is shown in (a). The white star represents the parameter combinations for the other East Antarctic figures. Water-limited, conduction-limited, and water-dominated regions indicated.

Conduction-Limited Regime

In the conduction-limited regime, the freezing rate is controlled by the rate that heat is conducted into the overlying ice sheet. The available water supply is not used up in this regime and the bed downstream of the freezing zone remains at the melting point. The downstream margin of the freezing region is marked by a change to melting conditions, rather than by a freezing front. Sliding may continue downstream of the freezing region, although less water will be available in the hydrologic system than was available upstream. Since the water flux is still relatively low in the conduction-limited regime, viscous dissipation and supercooling (Q_{hydro}) are small compared to the other terms in the basal energy balance. In the conduction-limited regime freeze-on thickness is insensitive to water flux, as represented by a broad plateau in the center of Figure 5.6. In this regime, freeze-on thickness is controlled by thermal forcing, ice thickness, and ice flow.

Water-Dominated Regime

In the water-dominated regime, viscous dissipation and supercooling (Q_{hydro}) are the dominant terms in the basal energy balance. As water flux increases past 10^4 m^2/yr, the other terms in the basal energy balance gradually lose importance. Once water flux reaches 10^5-10^6 m^2/yr, the freezing rate depends only on water flux, surface slope, and bed slope. When the bed/surface slope ratio is greater than the supercooling threshold (Equation 5.7), Q_{hydro} is positive and basal melting occurs. When the bed/surface slope ratio is less than the supercooling threshold, Q_{hydro} is negative and basal freezing occurs. Freeze-on can reach a kilometer thick in the water-dominated regime with sufficiently high water flux (Figure 5.6).

5.4.4 Ice Flow

The ambient ice flow regime exerts a strong control on the size of basal accretion reflectors. Any increase in the flux of meteoric ice into the domain reduces the thickness of the freeze-on unit. Internal deformation also increases the elevation at which the freeze-on unit will exit the domain relative to basal sliding.

Ice Velocity

Fast ice flow affects the size of accretion units in two ways. First, fast flow carries newly accreted ice away from the freezing zone before it can thicken. The second effect is shear heating, where fast flow warms the bed and reduces the freezing rate. As both effects have the same sign, freeze-on thickness monotonically decreases with increasing ice velocity (Figure 5.7a,c). The effect of shear heating can be seen as freeze-on thickness decreases with increasing surface slope (Figure 5.7a,c). Fast flow with a steep surface slope produces the most shear heating and the least freeze-on, while slow flow with a shallow slope produces the thickest freeze-on units.

Cross-Flow Divergence

Divergence in the cross-flow direction, as for ice flow along a ridge or away from a dome, pulls accretion units up from the bed. Cross-flow convergence, as at the onset of an ice stream, acts to push accretion units downwards. In our model, cross-flow divergence is represented by a flux of meteoric ice through the side boundaries of the domain (Figure 5.2). Because we have assumed that regions outside of the freezing zone are not also freezing, all of the ice entering from the sides in a convergent regime is meteoric ice. We have also assumed that all of the ice leaving the side margins in a divergent regime is meteoric ice, when some of it should be accreted ice as well. This simplified treatment of cross-flow divergence means that our thickness estimates are an upper limit when cross-flow divergence is positive. Cross-flow divergence will monotonically increase the thickness of basal freeze-on units (5.7b,d).

Basal Sliding and Internal Deformation

Ice flow in our model is accommodated both by basal sliding and internal deformation. Both

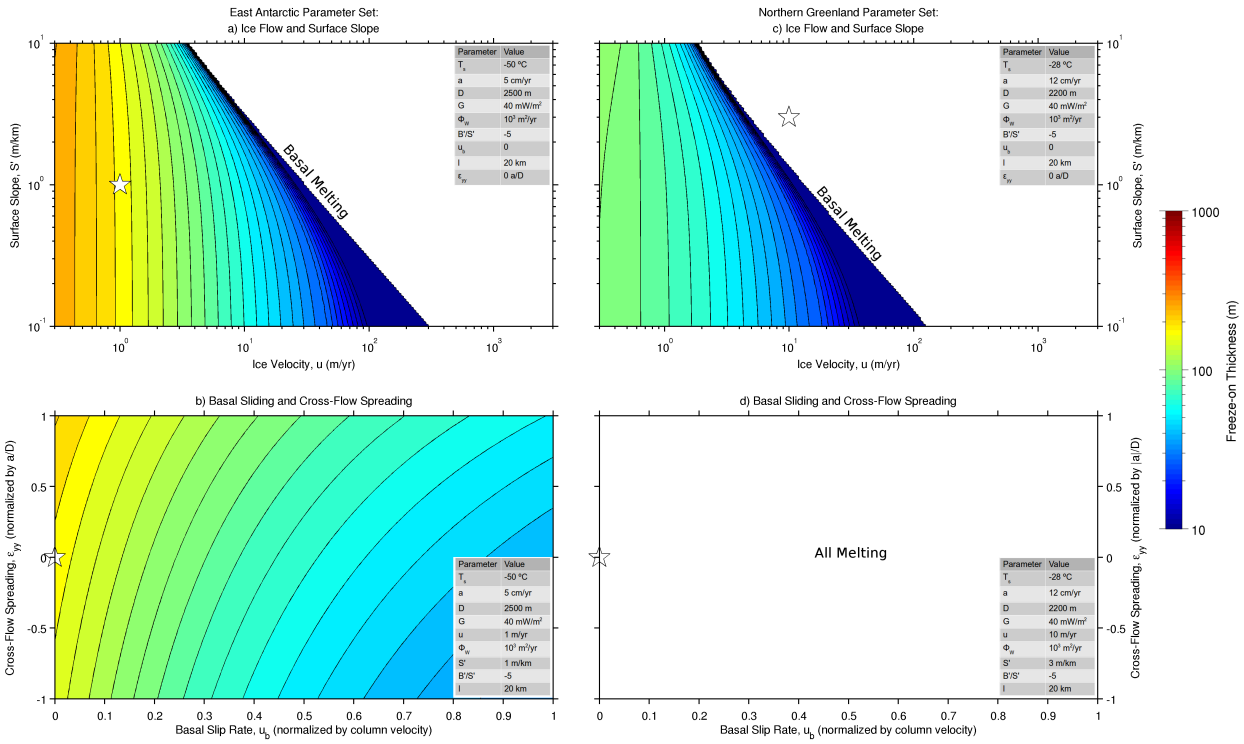

Figure 5.7: Ice flow effects on freeze-on thickness in the accumulation zone. Top row (a,c) shows thickness as a function of ice column-average velocity and surface slope, bottom row (b,d) shows thickness as a function of slip ratio (sliding velocity divided by column-average velocity) and cross-flow divergence. Left column (a,b) is for the East Antarctic parameter set, right column (c,d) is for the north Greenland set. White stars show the parameter combinations used for other figures.

processes can impact the thickness of basal freeze-on units. When basal sliding increases, the conductive heat loss is enhanced because of increased downward advection near the bed (Figure 5.1a,c). Increased conductive heat loss increases the freezing rate. When internal deformation increases, thicker freeze-on units will form for a given freezing rate. Internal deformation is associated with a lower vertical strain rate near the bed (Figure 5.1a), allowing freeze-on to thicken before being exposed to stretching and thinning higher in the column. The thickening due to internal deformation is the dominant process.

Basal freeze-on units are largest when the ice sheet moves by internal deformation. Internal deformation creates a slow-moving basal section where freeze-on units can grow before being swept away by fast ice flow higher in the column. In contrast, basal sliding sweeps freeze-on ice downstream before it thickens, like a plume of smoke in a strong wind. The ice flow effect is represented in our model through $\hat{w}^{-1}$, a function that depends on the distribution of ice flow between sliding and deformation (Equation 5.3, Figure 5.1a). Increased basal sliding monotonically decreases the thickness of freeze-on units (Figure 5.7b,d).

5.4.5 Length

The thickness of a freeze-on unit depends on the along-flow length of the freezing zone. Freeze-on thickness, like all englacial stratigraphy, is sensitive to forcings that are integrated

over time and space. Thickness responds to the integrated volume added to the ice column as the ice flows over the freezing zone. Longer freezing zones add more volume to the ice sheet and produce thicker freeze-on units (Figure 5.8). Internal deformation fosters the initial formation of freeze-on units when length is small but restricts further thickening once the freeze-on unit reaches faster flowing ice higher in the column. Freeze-on thickness for the internal deformation profile increases rapidly when length is less than ∼10 km, but begins to level off after that (Figure 5.8). Ice traversing a long freezing zone also experiences greater vertical thinning due to surface accumulation. As length increases, the additional volume of freeze-on ice comes to be balanced by surface accumulation and cross-flow divergence. The limiting value of freeze-on thickness as length increases is given by,

$$\lim_{l\to\infty} \hat{z}_{acc} = \hat{w}^{-1}\left(\frac{f}{a+f-D\dot{\epsilon}_{yy}}\right). \tag{5.15}$$

The limiting value of freeze-on thickness is independent of horizontal velocity, $\bar{u}$. As the freezing zone lengthens, the influence of the ice flux entering from upstream declines.

At the other extreme, when the freezing zone is small the meteoric ice flux is almost completely composed of upstream horizontal transport. In the limit that the length of the freezing zone approaches zero, surface accumulation and cross-flow divergence can be

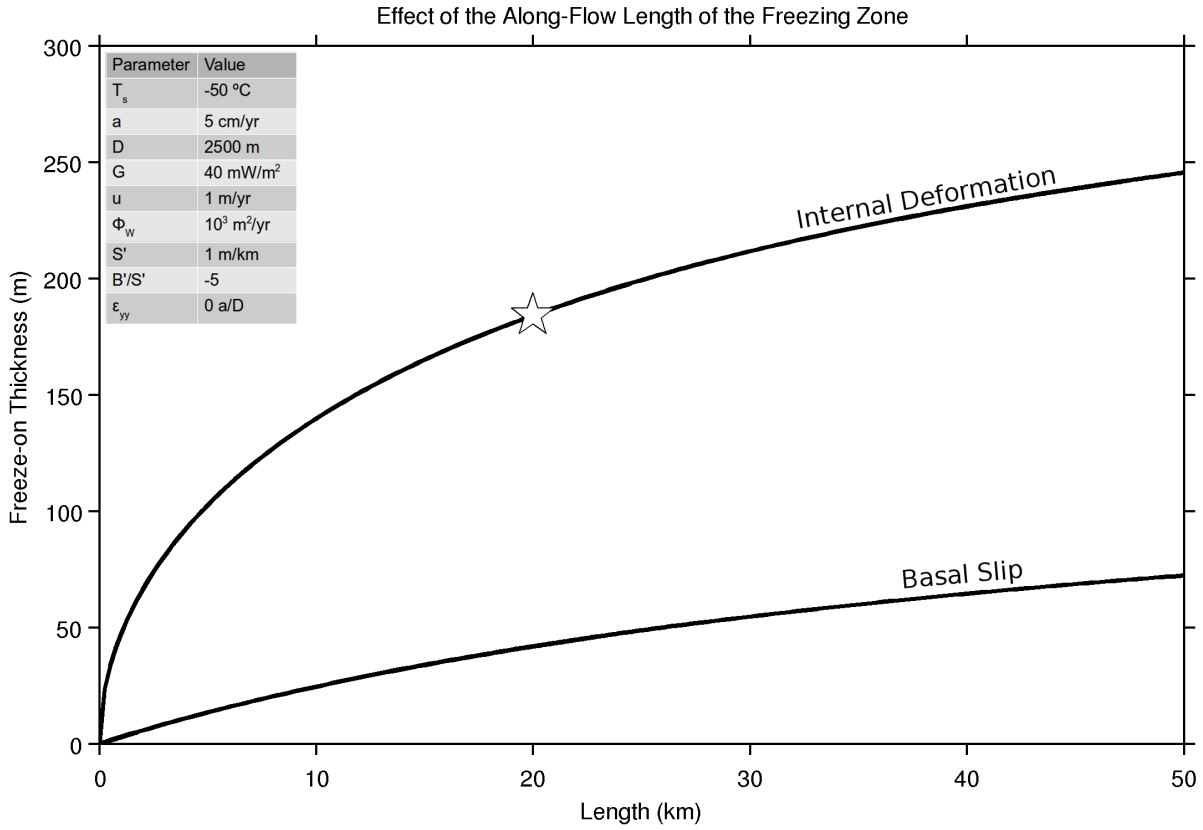

Figure 5.8: Lengthscale effects on freeze-on thickness for the East Antarctic parameter set. Plot shows the thickness of the freeze-on units as a function of the along-flow length of the freezing zone for basal sliding and internal deformation velocity profiles. White star shows the parameter value used for other figures.

neglected from the meteoric flux. In that limit, freeze-on thickness is given by,

$$\lim_{l \to 0} \hat{z}_{acc} = \hat{w}^{-1} \left(\frac{lf}{\bar{u}D} \right). \tag{5.16}$$

When the length of the freezing zone is small, the fraction of total ice flux composed of freeze-on ice is proportional to the length of the freezing zone.

5.5 Discussion

Given the results described above, we discuss the implications of our model for the subglacial water flow and internal structure of ice sheets. First, we compare the specific water fluxes required to produce large conductively cooled or supercooled freeze-on structures with melt rates and catchment areas in Antarctica and Greenland. We discuss the likely relationship between large subglacial water fluxes and fast ice flow, and consider that exceptions to that relationship might occur at flow bifurcations. We compare the water fluxes in our model with known subglacial water fluxes from active lakes, moulins, and outburst floods. We discuss model limitations. Finally, we apply our model to Greenland and Antarctica and discuss locations that are favorable for basal freeze-on.

5.5.1 Subglacial Water Flow

Conductive cooling requires 10^2-10^3 m^2/yr of water flux to build moderate accretion units ($\sim$100m). Here, we assume that the freezing zone has a cross-flow width of 10 km based on the observed structures (*Bell et al.*, 2011, 2014). Cross-flow width cancels out of our analysis of freeze-on thickness (Equation 5.12), but cross-flow width is necessary to make comparisons between specific water flux and volume water flux, melt rate, or catchment area. For flow through a 10 km wide freezing zone, 10^2-10^3 m^2/yr of specific flux is equivalent to 1 mm/yr of melt from a catchment area of 10^3-10^4 km^2. At Dome A in East Antarctica, the water networks that feed the freeze-on units have catchments that are also in the range of 10^3-10^4 km^2 (*Wolovick et al.*, 2013, Table 2)[3]. The Dome A basal structures are on average 100-200 m thick. Conductive freeze-on of subglacial meltwater can produce these structures.

Supercooling requires 10^4-10^6 m^2/yr of water flux to build accretion units thicker than $\sim$100 m. As supercooling is likely dominant in the ablation zone, we consider water flux from surface melt in addition to basal melt. In the ablation zone surface melt rates are on the order of 1 m/yr. This melt rate could produce sufficient water flux for supercooling from a catchment area of 10^2-10^4 km^2. For comparison, we estimate potential catchment areas in the ablation zone of the Greenland Ice Sheet. The ablation zone along the western Greenland margin is 50-100 km wide (*Noel et al.*, 2015). We assume that half of this width, 25-50 km, is available to feed a potential freeze-on unit. Because of the strong influence of ice surface slope on hydraulic potential gradient, we assume that the catchment region cannot be elongated parallel to the coast. The maximum catchment area is therefore given by the half-width of the ablation zone squared, or 625-2500 km^2. This catchment area is within the

[3]Table 2.2 in this thesis.

range of 10^2-10^4 km^2 needed to produce large freeze-on structures from supercooled surface meltwater. In contrast to surface melt, basal melt rates in the accumulation zone are on the order of 1 mm/yr, requiring catchment areas of 10^5-10^7 km^2 to build substantial freeze-on units via supercooling. The high end of this range is the same order of magnitude as the entire Antarctic continent, while the low end is similar to the catchment area of Pine Island Glacier. Water from a single ice stream catchment basin could be funnelled to a single freezing zone at an adverse bed slope within the trunk of the ice stream.

5.5.2 Correlation Between Ice Flow and Water Flow

Fast ice flow and fast water flow both tend to be concentrated in ice streams and outlet glaciers. Because of the dominant impact of ice surface slope on hydraulic potential gradient, water generally follows ice flow downstream. Just as ice streams collect ice from a wide catchment area, ice streams also tend to collect water from a similarly wide catchment area. Fast flowing ice streams also produce meltwater through shear heating, further increasing the water flux. The greatest subglacial water fluxes in the accumulation zone are likely to be found in fast flowing ice streams and outlet glaciers. Ice streams may be the only locations where the water-dominated regime occurs in the accumulation zone. Supercooling will be favored when ice streams flow up adverse bed slopes out of subglacial overdeepenings. Because of fast ice flow and extensive basal sliding in these regions, freeze-on structures are likely to be thin layers ($\leq$10 m) near the bed. Where supercooling constricts water passages up adverse slopes, water pressure tends to increase, causing water to spread out into a distributed system and reducing basal drag (*Rothlisberger*, 1972; *Hooke*, 1991; *Creyts and Clarke*, 2010).

Large water fluxes may be found in the accumulation zone outside of fast flowing ice streams at water flow bifurcations. Subglacial water flow is not always coincident with ice flow. In places, bed or surface topography may route subglacial water that was originally in the trunk of a fast-flowing ice stream out of the ice stream. For example, there is evidence that basal freeze-on occurs in the Shackleton Range at the margins of Recovery Ice Stream, where water from a network of active lakes is routed out of a deep subglacial trough uphill into a slower flowing thin ice region (*Fricker et al.*, 2014). In these locations, high water flux generated in a fast-flowing ice stream is transported into a region of slower ice flow, thin ice, and uphill bed slopes. Flow bifurcations have the potential to produce thick freeze-on units adjacent to ice streams.

5.5.3 Comparison with Known Water Fluxes

One of the only observational estimates of subglacial water flux in the accumulation zone of large ice sheets comes from satellite records of the filling and draining cycles of active lakes in Antarctica. These satellite-based estimates are at the high end of the range of subglacial water fluxes that we have considered. Lower fluxes may not produce rapid surface changes observable from space. *Fricker et al.* (2007) estimated water volume fluxes on the order of 1 km^3/yr in the Whillans and Mercer Ice Streams, equivalent to 10^5 m^2/yr if we assume 10 km cross-flow width. *Fricker et al.* (2010) and *Smith et al.* (2009) found similar order of magnitude volume fluxes. The observed active lakes have filling and draining cycles on the

order of several years, although the short observational record cannot rule out longer cycles. Many active lakes are in ice streams (*Smith et al.*, 2009) where freeze-on structures will be a small fraction of ice thickness, but supercooling freeze-on could still play an important role in regulating basal drag.

In the ablation zone, water fluxes can be estimated from moulin inputs. *Smith et al.* (2015) estimated volume fluxes for individual moulins in the range of 1-10 m^3/s, or about 10^7-10^8 m^3/yr. Using our assumed 10 km cross-flow width, this translates to 10^3-10^4 m^2/yr water flux per moulin. As supercooling requires 10^4-10^6 m^2/yr to build large freeze-on units, subglacial flow must collect the input from 1-1000 moulins to produce a large freeze-on unit. For comparison, *Smith et al.* (2015) found a moulin density of approximately 0.1 per km^2, and *McGrath et al.* (2011) found a moulin density of approximately 1 per km^2, implying that large freeze-on units require catchments of 10^0-10^4 km^2 during peak melt season. This range represents subglacial catchments collecting the input from multiple moulins, while the moulins themselves could have larger supraglacial catchments. The supraglacial catchments must be in the range of 10^2-10^4 km^2 (Section 5.5.1). Care is also required when considering moulin inputs, because the melt season in Greenland is only part of the year and subglacial water flux must be averaged over many years when determining the size of englacial freeze-on structures.

Freeze-on thickness is a time-integrated quantity. Depending on the length of the freezing zone and the ice flow rate, freeze-on structures may take several hundred to a thousand years to form. During this time period, water flux and freezing rate may fluctuate wildly. In the ablation zone, supercooling produces extremely high freezing rates during the melt season, and no freezing at all during the rest of the year. In the accumulation zone, active lakes may fill and drain on timescales of several years, producing wide swings in downstream water flux. Small variations in ice sheet surface gradient far upstream may alter water routing, causing variations in water flux through the freezing zone (*Wright et al.*, 2008). In both the accumulation zone and in the ablation zone, freeze-on ice that forms during times of high water flux will be thinned and advected away by ice flow during times of low water flux.

If water flux varies on longer timescales than it takes to build a freeze-on structure, or if a large amount of freeze-on ice is created all at once, then freeze-on thickness should fluctuate as well. Short-lived subglacial outburst floods or jokulhlaups are capable of producing temporary water fluxes greater than the water fluxes we have considered. Estimates of maximum discharge for historical outburst floods are as high as $3x10^5$ m^3/s (*Roberts*, 2005), while geologic evidence from the Labyrinth on the margin of the East Antarctic Ice Sheet indicates that outburst floods there during the Miocene had flow rates on the order of 10^6 m^3/s (*Lewis et al.*, 2006). The Labyrinth volume flux translates to 10^{13} m^3/yr, or about 10^9 m^2/yr for a 10 km cross-flow width. During such floods, supercooling could potentially produce extremely high freezing rates in areas with favorable bed and surface geometry. In the case of sudden outbursts through regions with favorable geometry, thick freeze-on units would form immediately after a flood, while between floods the freeze-on units would be thinned and transported down-flow.

5.5.4 Model Limitations

This simple model has a number of limitations. This analysis has not considered the negative

feedback of upwards advection caused by freeze-on. Basal freeze-on produces upwards flow near the ice sheet base, reducing the temperature gradient and limiting conductive heat losses. Our simple temperature model (Section 5.3.1) assumes no vertical velocity at the ice sheet base. When freeze-on structures are small, the difference between conductive heat losses with and without upwards advection should also be small. When freeze-on structures are large, upwards advection should become an important limiting feedback. Upwards advection associated with large freeze-on structures will produce a nearly isothermal layer near the bed, reducing conductive heat losses and limiting the rate of freeze-on.

Local one dimensional analyses are necessarily limited. Horizontal temperature advection and longitudinal stress gradients cannot be included. A steady state model cannot account for transient freeze-on events, ice flow disturbances, or surface climate variability. Despite the limitations of a simple model, the relationships between the variables controlling freeze-on structures can be highlighted.

5.5.5 Where is Freeze-on Likely to be Found?

To investigate where freeze-on can occur, we apply our model to Antarctica and Greenland. We use ice sheet geometries from *Fretwell et al.* (2013) and *Bamber et al.* (2013a). Greenland surface temperature and accumulation are taken from RACMO2.3 (*Noel et al.*, 2015). Antarctic surface temperature is taken from *Comiso* (2000) and accumulation is the mean of *Arthern et al.* (2006) and *Van de Berg et al.* (2005). Geothermal flux for both ice sheets is from *Shapiro and Ritzwoller* (2004). Antarctic surface climate and geothermal flux are accessed via the ALBMAPv1 dataset (*Le Brocq et al.*, 2010). Ice flow velocities are taken from *Joughin et al.* (2010) for Greenland and from *Rignot et al.* (2011) for Antarctica. We do not correct the velocity data for the difference between surface velocity and column-average velocity. We assume that ice flow is by internal deformation because freeze-on is generally found in slowly flowing areas. For the accumulation zone in both ice sheets, we assume the freezing zone is 20 km long, we low-pass filter the input datasets at 20 km, and we assume that 10^3 m^2/yr of water flux is available everywhere. For the ablation zone in Greenland, we assume the freezing zone is 5 km long, we low-pass filter the input datasets at 2.5 km, and we assume that 10^6 m^2/yr of water flux is available everywhere.

Many areas of East Antarctica are ideal for basal freeze-on (Figure 5.9). Surface temperature and geothermal flux are both very low (roughly -50 °C and 40-50 mW/m^2), favoring conductive cooling (*Comiso*, 2000; *Shapiro and Ritzwoller*, 2004). Widespread slow ice flow via internal deformation allows freeze-on to thicken. The areas around Dome A, Ridge B, Dome C, and Dome F are all favorable for freeze-on. Thin ice regions near the margins in between fast-flowing ice streams, such as the Shackleton Range (*Fricker et al.*, 2014), are also favorable for freeze-on. Smaller peripheral domes, such as Law Dome and Berkner Island, are also favorable for freeze-on.

Pattyn (2010) estimated Antarctic basal temperature and melt rate using a three dimensional steady-state model. Our model generally shows more extensive basal freezing than his in East Antarctica. Both models predict cold conditions underneath Dome A, Dome F, and in the Vostok Highlands underneath Ridge B, although the extent of cold-based conditions in our model is larger for all locations (Figure 5.9, c.f. *Pattyn* (2010, Figure 3)). Pattyn's model shows small patches of cold-based conditions underneath Dome C, while our model

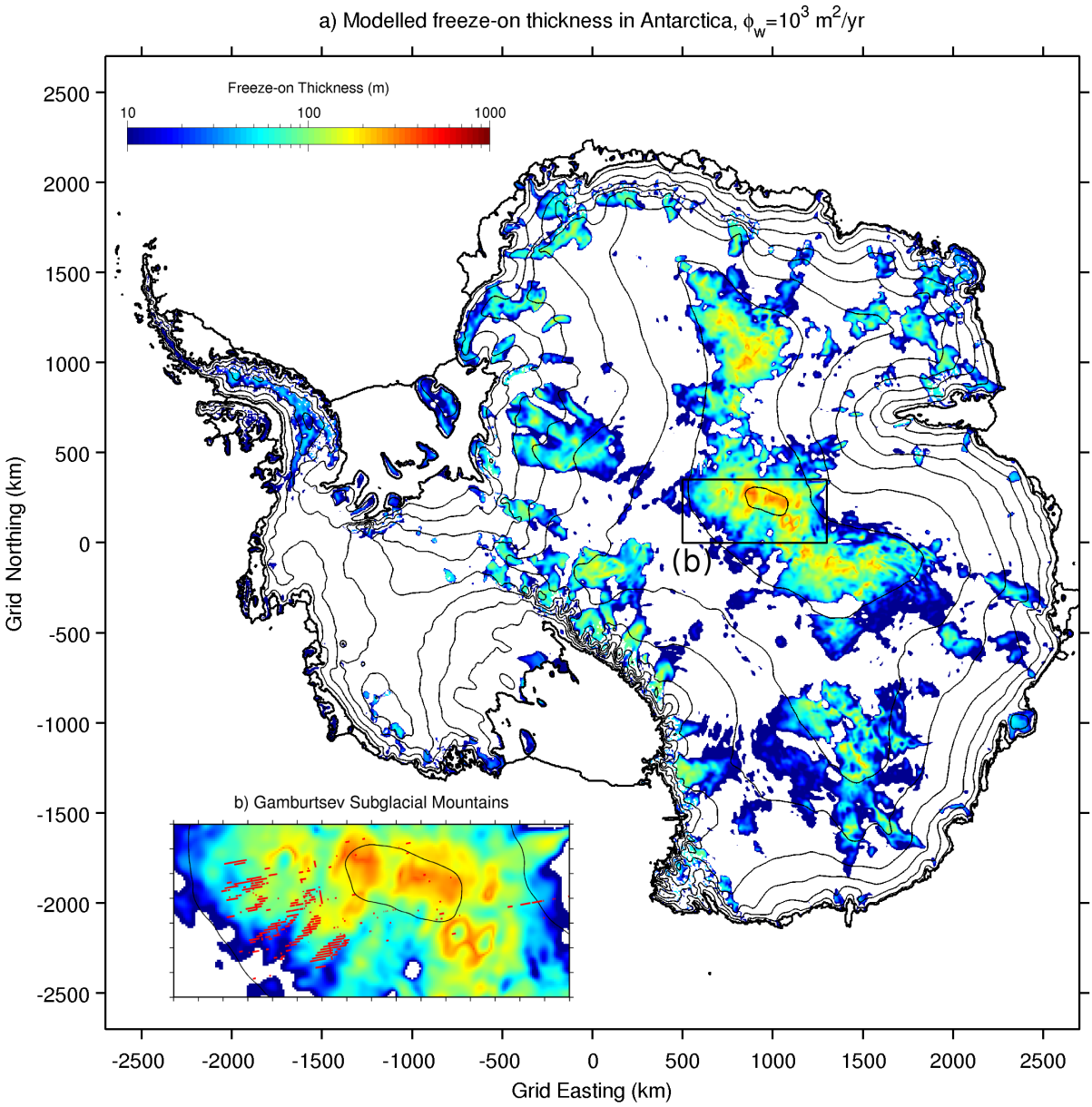

Figure 5.9: Distribution of maximum freeze-on thickness, z_{acc}, for Antarctica. A constant water flux of 10^3 m^2/yr is assumed to be available everywhere. Surface contours are shown at 500 m intervals. Inset shows the Gamburtsev Subglacial Mountains with Accretion Type 1 picks from *Bell et al.* (2011) in red.

shows more spatially extensive freezing conditions there. Both models place basal melting in the deep subglacial troughs underneath Dome C, as well as cold-based conditions in the thin ice in between the outlet glaciers on the back side of the Transantarctic Mountains, in Palmer Land in the Antarctic Peninsula, in Berkner Island, in Roosevelt Island, and in the ice rises of the Filchner-Ronne Ice Shelf. Both models show freezing conditions in downstream Kamb and Whillans Ice Streams, even though neither steady-state model should be expected to capture the transient dynamics at work there (*Retzlaff and Bentley*, 1993). Many of the differences between the models can be attributed to different geothermal flux inputs; Pattyn's

model used a lower geothermal flux in West Antarctica and a higher geothermal flux in East Antarctica, as well as a geothermal flux input that was locally tuned to produce melting in the locations of known subglacial lakes (*Pattyn*, 2010, Figure 2). Other differences arise because our model used an updated ice thickness map (*Fretwell et al.*, 2013), while Pattyn's used a more advanced three dimensional thermal model.

While much of the Antarctic ice sheet has conditions favorable for freezing, the distribution of freeze-on is limited by of the availability of subglacial water. Water flows down the gradient of hydraulic potential, generally moving away from ice domes and becoming concentrated in fast-flowing ice streams. Marginal domes such as Law Dome and Berkner Island are likely to be cold-bedded rather than actively freezing because of the lack of water. Borehole measurements of basal temperature at both locations indicate cold-based conditions there (*Morgan et al.*, 1997; *Mulvaney et al.*, 2007). Underneath the larger domes, variability in bedrock topography will modify the routing of subglacial water. Underneath Dome A, the Gamburtsev Subglacial Mountains play a crucial role in directing water flow because of low ice surface slopes (*Wolovick et al.*, 2013). Deep subglacial valleys provide warm melting catchments that funnel water up and over mountain ridges where freeze-on occurs (*Creyts et al.*, 2014). The highly incised bed topography concentrates water into a few narrow freezing regions. Our simple model does not take into account the influence subglacial water networks have on the distribution of basal freeze-on. While our Antarctic map (Figure 5.9) shows where basal freeze-on is possible, water availability will limit the actual distribution.

We also compute potential freeze-on locations in Greenland for both a low water flux accumulation zone case and a high water flux ablation zone case. The conditions in the interior of northern Greenland where large basal structures have been observed are not favorable for conductive freeze-on (Figure 5.10). Warmer surface temperatures (*Noel et al.*, 2015), faster ice flow (*Joughin et al.*, 2010), and steeper surface slopes (*Bamber et al.*, 2013a) in most of the Greenland accumulation zone make freeze-on difficult compared to East Antarctica (Figures 5.4 and 5.7). The bed topography in the interior of Greenland is also relatively flat. With little variability in ice thickness, it is difficult for warm catchments to coexist in close proximity to cold freezing zones. An alternate explanation for the large basal structures observed in the interior of northern Greenland is likely. Travelling slippery patches (*Wolovick et al.*, 2014) or rheological contrasts within the ice column (*NEEM Community Members*, 2013) are likely to be active here. Only regions close to the margins where ice is thinner are favored for conductive freeze-on in Greenland.

The margins of Greenland have high rates of surface ablation. Surface ablation produces far more melt than basal melting, supporting supercooling where bed slopes are appropriately oriented. Ridges in between outlet glaciers around the Greenland margin are ideal locations for large supercooled freeze-on structures because ice flow is slow and water fluxes can be high. Our model indicates that the basal structure observed near Eqip Sermia may be a thin unit of freeze-on uplifted over meteoric ice (Figure 5.10b), while the structure observed near Storstrommen may become a thick package of freeze-on ice at it's downstream margin (Figure 5.10c). A thin unit of freeze-on ice may be uplifted over meteoric ice if the freezing front has advanced downstream over time. The marginal Greenland units (*Bell et al.*, 2014) are likely to have been produced by basal freeze-on. Our model indicates that many areas around the Greenland margin in addition to the places where basal structures have already been observed could also be favorable for super-cooled freeze-on. Water availability may limit

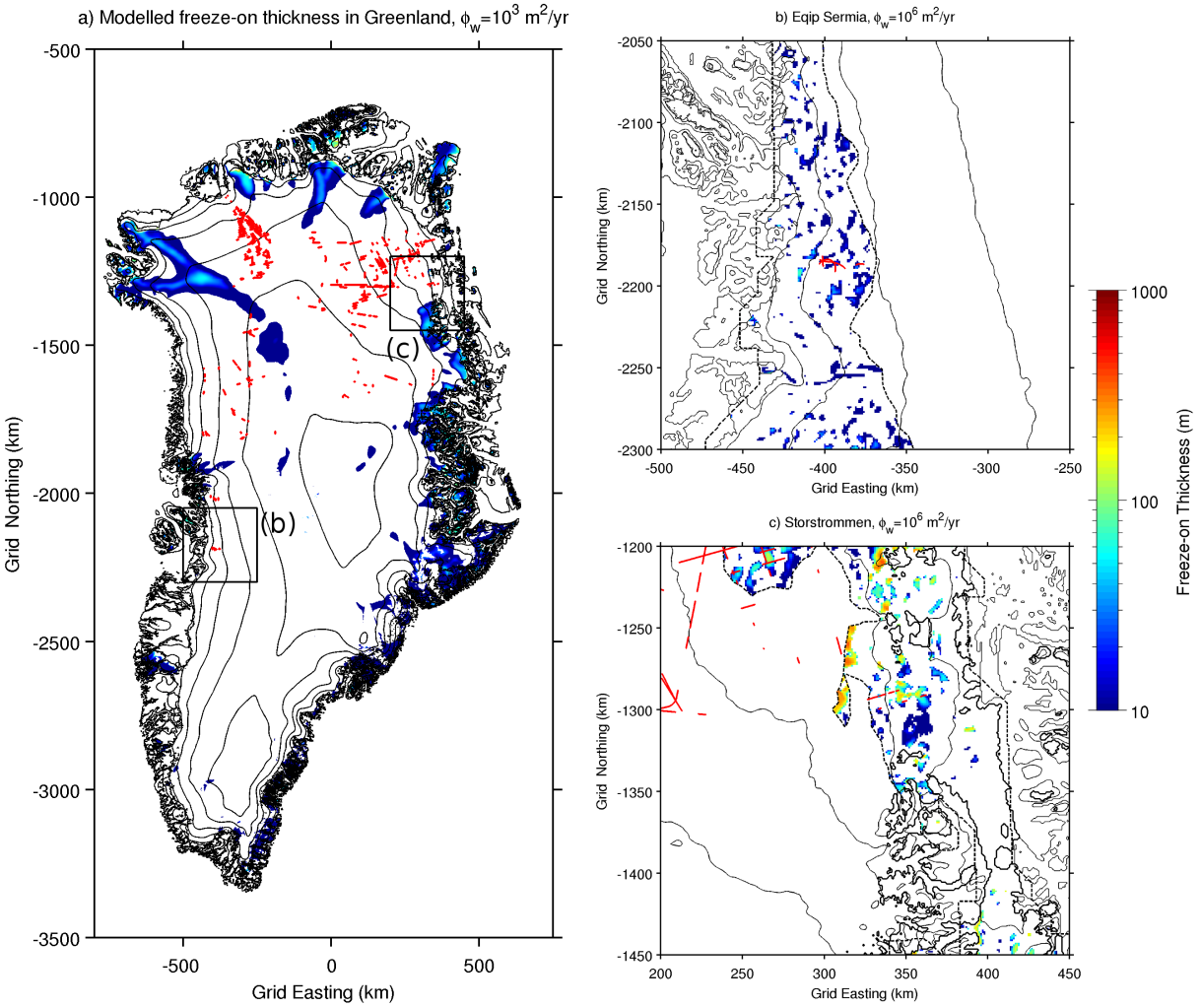

Figure 5.10: Distribution of maximum freeze-on thickness, z_{acc}, for Greenland. a) Low water flux, appropriate for the interior (10^3m^2/yr), (b,c) high water flux, appropriate for the ablation zone (10^6 m^2/yr). (b) and (c) are shown zoomed in near the marginal units shown in *Bell et al.* (2014). Freeze-on thickness is not plotted above the Equilibrium Line (dashed black line) in (b) and (c). Freeze-on length is assumed to be 20 km in (a) and 2.5 km in (b) and (c), so that short-wavelength adverse bed gradients are preserved. Surface contours are shown at 500 m intervals.

the distribution of real freeze-on units, and undetected freeze-on units may be obscured by the difficult radar environment near the ice sheet margin.

Freeze-on may also have been an important process in the former northern hemisphere ice sheets. Mountainous nucleation sites near the ice sheet center, such as the Torngats underneath the Laurentide Ice Sheet, would have been ideal locations for conductive freeze-on analogous to the Gamburtsevs in East Antarctica (*Creyts et al.*, 2014). Mountainous topography around the ice sheet margin, such as the Adirondacks, White Mountains, and Green Mountains, would have been ideal locations for adverse bed slopes that could have produced large supercooled freeze-on structures. In addition, overdeepenings in fast flowing regions could have hosted important freeze-on zones that helped control basal drag, even if fast flow prevented the formation of large englacial freeze-on units.

5.6 Conclusions

In the accumulation zone, conductive freeze-on is capable of producing freeze-on structures 100-200 meters thick. Conductive freezing rates will be highest when surface temperature is low, accumulation rates are relatively high, and ice thickness and geothermal flux are both low. Supercooling is capable of producing freeze-on structures up to a kilometer thick if water flux is sufficiently high. Supercooling requires high water flux, a steep ice surface slope, and a steeply backsloping bed. Both conductive freeze-on and supercooling build larger structures in slow-flowing regions where shear heating and the flux of meteoric ice are low. If the ice flow is by internal deformation rather than basal sliding, freeze-on structures can grow larger in the slowly-flowing ice near the bed before being carried downstream by fast flow higher in the column. Surface ablation acts to create upwards flow in the ice column, pulling basal freeze-on units up off of the bed.

Conductive freeze-on likely produces the basal structures observed in East Antarctica (*Bell et al.*, 2011). Surface temperatures are very low in East Antarctica, increasing conductive heat losses. The deeply incised valleys of the Gamburtsev Subglacial Mountains funnel water from deep melting regions to shallow ridges where freezing takes place (*Wolovick et al.*, 2013; *Creyts et al.*, 2014). In addition, adjacent areas of the Vostok Highlands may also host freeze-on structures. Our model suggests that basal freeze-on may be commonplace in slow-flowing areas of East Antarctica. In contrast, the large basal units observed in the interior of northern Greenland are likely to be explained by another mechanism, such as travelling slippery patches or rheological contrasts within the ice column (*Wolovick et al.*, 2014; *NEEM Community Members*, 2013). Basal structures observed around the margins of the Greenland Ice Sheet are likely to be produced by supercooling of surface meltwater. Similar supercooling is also likely to have occurred in mountainous regions and overdeepenings around the margins of the former northern hemisphere ice sheets.

Basal freeze-on releases latent heat, warming the ice column. Water flow transports excess heat from the warm catchment region into the cold freezing region, rearranging mass and energy underneath the ice sheet. Freeze-on ice is likely to have a different crystal size, sediment content, and hence rheology from the meteoric ice that composes the rest of the ice sheet. The injection of a different ice type near the base, where strain rates are highest, is likely to have important effects on ice flow. Freeze-on also removes water from the hydrologic system, reducing the amount of water available downstream and potentially dewatering subglacial till and increasing basal drag. Alternately, closure of subglacial conduits may increase water pressure and force water to spread out in a distributed system, reducing basal drag. Through these combined influences, freeze-on may play a crucial role in regulating basal drag, even in fast-flow ice streams.

Chapter 6

Conclusion

The flow and history of ice sheets is reflected in their internal structure. Climatic forcings, internal deformation, and basal processes all leave their mark in the stratigraphic structure of ice sheets. The stratigraphically complex layers near the bed provide an especially rich environment for studying the processes that control the flow and sliding of ice sheets.

In 2009, during my first year of graduate school, we observed large-amplitude basal reflectors in ice-penetrating radar data from East Antarctica (*Bell et al.*, 2011). Operation IceBridge data collected beginning in 2010 detected similar structures in Northern Greenland (*Bell et al.*, 2014). These structures deform the overlying stratigraphy into anticlines, synclines, and overturned folds. The vertical amplitude of the structures ranges from below the limit of radar detectability to approximately a kilometer. These structures point towards new processes at the ice bed or within the ice column.

Three explanations have been advanced to explain these structures: freeze-on of subglacial water, traveling patches of slippery and sticky conditions, and rheological contrasts within the ice column. Freeze-on was the mechanism we originally proposed in (*Bell et al.*, 2011). In Chapter 2 I identified subglacial water networks feeding the East Antarctic freeze-on units, and in Chapter 5 I explored the conditions that are favorable for freeze-on. I described the thermal feedback responsible for traveling slippery patches in Chapter 3, and I explored the stratigraphic overturn caused by traveling sticky patches in Chapter 4. The rheological contrasts mechanism was proposed by (*NEEM Community Members*, 2013). I have not explored the rheological contrasts mechanism in this thesis. However, the rheological structure of the ice sheet is likely to interact with both of the other two mechanisms. The overturning that occurs above traveling sticky patches is caused by deformation within the ice column, and freeze-on structures require an ice flow regime dominated by internal deformation in order to grow large.

Different mechanisms likely dominate in different settings. In East Antarctica, freeze-on is the most likely cause of the observed basal structures because of cold surface temperatures, slow ice flow, and deep valleys that feed water to shallow cirques. In the interior of northern Greenland, a combination of traveling patches and rheological contrasts produces the observed structures. The interior of northern Greenland has warmer surface temperatures, faster ice flow, and a much flatter bed than East Antarctica. The margin of northern Greenland may contain freeze-on structures produced by supercooled surface melt.

Four main outstanding questions related to the large basal structures remain: the relative

contributions of the three mechanisms, the interactions between the mechanisms, the role of subglacial sediments, and the relationship between these mechanisms and basal conditions inferred from remote sensing observations.

The relative contributions of the three mechanisms to individual folds remains unresolved. Simple freeze-on models, such as the one used in Chapter 5, can give us an indications of the general settings where freeze-on is an adequate explanation for the observed structures and of the settings where freeze-on is not an adequate explanation. However, simple freeze-on models cannot partition the remaining structures between traveling patches and rheological contrasts, nor can these models reveal if the other two mechanisms are in play in addition to freeze-on. Quantitative attribution of stratigraphic folds between the three proposed mechanisms will require better models or new data.

The next major outstanding question is how the three mechanisms interact with one another. All three mechanisms are likely to be operating to some degree in most of the observed structures. For structures produced primarily by freeze-on, fluctuations in the freezing front position will produce stratigraphic effects via the traveling patches mechanism. If the freezing front advances downstream at a similar velocity to the overlying ice column, the freeze-on structure will be much larger than if the freezing front is stationary or retreating upstream. For structures produced primarily by traveling patches, freeze-on will be present at the downstream edges of the slippery patches or within the sticky patches. The rheological structure within the ice column will modify the boundaries of the overturning vortex that forms above a traveling sticky patch. Rheological contrasts can operate independently of the other two mechanisms in environments where the ice is completely frozen to the bed. However, variable basal sliding and freeze-on will modify the stratigraphic folds produced by the rheological contrasts. New feedback mechanisms may emerge when all three mechanisms operate together, potentially producing effects that are difficult to anticipate.

The role of basal sediments is also unknown. The traveling patches models developed to date (Chapters 3 and 4) do not include any representation of sediments. Soft, water-saturated sediments are crucial for reducing basal drag and increasing basal slip. The presence of unsaturated sediments has the potential to reduce the propagation velocity of traveling patches by providing a storage capacity at the bed. Storage of subglacial water in porous sediments will increase the response time of the basal system and therefore slow the propagation of slippery patches at the ice base. Similarly, sediments that are already saturated provide a reservoir of water that takes time to be removed by freeze-on, reducing the propagation velocity of sticky patches.

The relationship between the basal structures and basal conditions inferred from inversions of remote sensing data remains to be explored. Regular "ribs" have been seen in inversions of basal drag for both Greenland and Antarctica (*Sergienko and Hindmarsh*, 2013; *Sergienko et al.*, 2014). Similar rib-like structures have also been observed in the surface driving stress of both ice sheets. It is still unclear how these ribs are related to traveling patches or to the internal structure of the ice sheets. If the ribs move downstream over time, they could behave as traveling sticky patches and produce stratigraphic folds within the overlying ice column. Thermal advection associated with this stratigraphic deformation could cool the bed and keep the sticky ribs sticky. A detailed comparison of stratigraphic data with the ribs would test the whether the observed ribs move over time and if they are associated with large basal structures.

Many of the outstanding questions related to the basal structures can be addressed with additional field and modeling studies. A focused field program targeting an individual structure could be used to understand the basal conditions and clarify the contributions of the different mechanisms. A surface GPS grid could measure ice velocity, uplift rates, and surface strain rates. If a traveling sticky patch is the primary mechanism responsible for producing the fold, then the surface flow field should contain extension at the upstream margin and compression at the downstream margin. This occurs because surface longitudinal strain rates are opposite to basal strain rates. This strain rate field would be superimposed on the regional extensive strain field produced to balance surface accumulation. Basal freeze-on will be associated with additional surface extension, as the ice flows faster to accommodate the input of mass from below. Rheological contrasts within the ice column should produce a more complicated surface strain rate signature. Boreholes drilled through the basal structures should be able to measure the relative components of meteoric and accreted ice. Downhole temperature profiles could measure the thermal inversion characteristic of rapid stratigraphic overturn, or detect the excess heat in the basal ice due to latent heat of freeze-on. Sampling the basal conditions will provide insight into the relative role of slip, water, freeze-on, and sediments. Phase-sensitive radar measurements could be used to measure englacial profiles of vertical velocity. These velocity profiles will reveal the rates of uplift or subsidence associated with the stratigraphic deformation, as well as the distribution of velocity with depth.

Both forward and inverse models could be used to better understand the processes that produce basal structures. Forward models that incorporate all three mechanisms may reveal new feedbacks. The addition of rheological contrasts in forward models will be used to investigate whether rheology enhances or mitigates the stratigraphic effects of traveling patches. Inverse models using existing stratigraphic data could be used to solve for a history of basal slip and ice flow in northern Greenland. The inversion would reveal how the distribution of basal slip has propagated in the past, and how the deformation field within the ice has responded to changing rheology. Changing rheology occurs as rheological contrasts associated with climatic transitions migrate downwards over time within the ice column. The inverted flow history will enable a detailed examination of how the basal structures looked in the past and a reconstruction of their growth and decay over time.

All three mechanisms have consequences for the larger dynamics of the ice sheet. Basal traction and ice rheology control the flow of ice towards the margins and the dynamic response of the ice sheets to perturbations in a changing climate. Weak-bedded water-rich regions are vulnerable to rapid nonlinear changes, while strong-bedded frozen regions are less responsive. Traveling patches and basal freeze-on both modify the distribution of water at the ice sheet bed, creating a heterogeneous distribution of warm-based and cold-based regions. The coupling between different regions of the ice sheet, as well as the local response of cold-bedded regions, are determined by the rheological structure of the ice column. Basal freeze-on releases latent heat, warming and softening the ice column. Freeze-on ice itself is likely to have a different crystal size, sediment and impurity content, and hence rheology from the surrounding meteoric ice.

Deformation and folding associated with the basal structures disturbs the stratigraphic structure of the ice sheet. Stratigraphic disturbances alter the sequences observed in ice cores. Anticlines and synclines push old ice from near the bed either higher or lower in the column, respectively. Overturning vortices above traveling sticky patches can produce inverted and

repeated sections. Stratigraphic disturbances also modify the rheological structure of the ice column. When the ice is deformed, rheological contrasts associated with changing impurity concentrations at climatic boundaries are transported to new locations. Unusual flow and deformation patterns modify the ice sheet thermal structure via advection, regardless of the causal mechanism responsible for the deformation. If basal ice is uplifted into the middle of the ice sheet, sediment may be entrained up to a kilometer above the bed. When this sediment-rich deformed ice is later delivered to the calving front, such englacial debris may be transported long distances in icebergs before melting out. Deformed sediment-rich ice may contribute to far-flung deposits of ice-rafted detritus during Heinrich events (*Hemming*, 2004). Flow speedups associated with the interaction of multiple traveling patches (Chapter 3) could be related to the triggering of Heinrich surges.

The internal structure of ice sheets gives us a window into the processes that control ice dynamics and changes flow over time. The intriguing basal structures in Greenland and Antarctica tell a story of melting and freezing at the base, time-variable sliding, and deformation within the ice column. In different settings, different mechanisms operate to produce the observed folds. Even within the same setting, different mechanisms may contribute to individual folds to various degrees. For decades, the lower part of the ice column was hidden in a featureless "echo-free zone" (*Drewry and Meldrum*, 1978). As the supposedly "echo-free zone" has yielded to improved radar technology, a stratigraphic intricacy unmatched by structures higher in the ice column as been revealed. Many processes are active at or near the ice base, and these processes interact with each other over time to produce structures as mysterious as they are beautiful.

Bibliography

Alley, R., S. Anandakrishnan, C. Bentley, and N. Lord (1994), A water-piracy hypothesis for the stagnation of Ice Stream C, Antarctica, *Annals of Glaciology*, *20*(1), 187–194.

Alley, R. B., D. D. Blankenship, C. R. Bentley, and S. T. Rooney (1986), Deformation of till beneath ice stream B, West Antarctica, *Nature*, *322*(6074), 57–59, doi:10.1038/322057a0.

Alley, R. B., D. E. Lawson, E. B. Evenson, J. C. Strasser, and G. J. Larson (1998), Glaciohydraulic supercooling: a freeze-on mechanism to create stratified, debris-rich basal ice: II. Theory, *Journal of Glaciology*, *44*(148), 563–569.

Andrews, L. C., G. A. Catania, M. J. Hoffman, J. D. Gulley, M. P. Luthi, C. Ryser, R. L. Hawley, and T. A. Neumann (2014), Direct observations of evolving subglacial drainage beneath the Greenland Ice Sheet, *Nature*, *514*(7520), 80–83, doi:10.1038/nature13796.

Arcone, S. A., R. Jacobel, and G. Hamilton (2012a), Unconformable stratigraphy in East Antarctica: Part II. Englacial cosets and recrystallized layers, *Journal of Glaciology*, *58*(208), 253–264, doi:10.3189/2012JoG11J045.

Arcone, S. A., R. Jacobel, and G. Hamilton (2012b), Unconformable stratigraphy in East Antarctica: Part I. Large firn cosets, recrystallized growth, and model evidence for intensified accumulation, *Journal of Glaciology*, *58*(208), 240–252, doi: doi:10.3189/2012JoJ11J044.

Arthern, R. J., D. P. Winebrenner, and D. G. Vaughan (2006), Antarctic snow accumulation mapped using polarization of 4.3-cm wavelength microwave emission, *Journal of Geophysical Research: Atmospheres*, *111*(D6), doi:10.1029/2004JD005667, d06107.

Aschwanden, A., E. Bueler, C. Khroulev, and H. Blatter (2012), An enthalpy formulation for glaciers and ice sheets, *Journal of Glaciology*, *58*(209), 441–457, doi: doi:10.3189/2012JoG11J088.

Bailey, J. T., S. Evans, and G. d. Q. Robin (1964), Radio echo sounding of polar ice sheets, *Nature*, *204*(4957), 420–421, doi:10.1038/204420a0.

Bamber, J. L., R. L. Layberry, and S. P. Gogineni (2001), A new ice thickness and bed data set for the Greenland ice sheet: 1. Measurement, data reduction, and errors, *Journal of Geophysical Research: Atmospheres*, *106*(D24), 33,773–33,780, doi: 10.1029/2001JD900054.

Bamber, J. L., J. L. Gomez-Dans, and J. A. Griggs (2009), A new 1 km digital elevation model of the Antarctic derived from combined satellite radar and laser data - Part 1: Data and methods, *The Cryosphere*, *3*(1), 101–111, doi:10.5194/tc-3-101-2009.

Bamber, J. L., J. A. Griggs, R. T. W. L. Hurkmans, J. A. Dowdeswell, S. P. Gogineni, I. Howat, J. Mouginot, J. Paden, S. Palmer, E. Rignot, and D. Steinhage (2013a), A new bed elevation dataset for Greenland., *The Cryosphere*, *7*(2), 499–510, doi:10.5194/tc-7-499-2013.

Bamber, J. L., M. J. Siegert, J. A. Griggs, S. J. Marshall, and G. Spada (2013b), Paleofluvial mega-canyon beneath the central Greenland Ice Sheet, *Science*, *341*(6149), 997–999, doi:10.1126/science.1239794.

Bell, R., F. Ferraccioli, T. Creyts, D. Braaten, H. Corr, I. Das, D. Damaske, N. Frearson, T. Jordan, K. Rose, M. Studinger, and M. Wolovick (2011), Widespread persistent thickening of the East Antarctic Ice Sheet by freezing from the base, *Science*, *331*(6024), 1592–1595, doi:10.1126/science.1200109.

Bell, R. E., M. Studinger, A. A. Tikku, G. K. Clarke, M. M. Gutner, and C. Meertens (2002), Origin and fate of Lake Vostok water frozen to the base of the East Antarctic ice sheet, *Nature*, *416*(6878), 307–310, doi:10.1038/416307a.

Bell, R. E., K. Tinto, I. Das, M. Wolovick, W. Chu, T. T. Creyts, N. Frearson, A. Abdi, and J. D. Paden (2014), Deformation, warming and softening of Greenland's ice by refreezing meltwater, *Nature Geoscience*, *7*(7), 497–502, doi:10.1038/ngeo2179.

Benn, D., and D. Evans (1998), *Glaciers & Glaciation*, Arnold, London.

Bentley, C. R. (1987), Antarctic ice streams: A review, *Journal of Geophysical Research: Solid Earth*, *92*(B9), 8843–8858, doi:10.1029/JB092iB09p08843.

Bingham, R. G., D. M. Rippin, N. B. Karlsson, H. F. J. Corr, F. Ferraccioli, T. A. Jordan, A. M. Le Brocq, K. C. Rose, N. Ross, and M. J. Siegert (2015), Ice-flow structure and ice dynamic changes in the Weddell Sea sector of West Antarctica from radar-imaged internal layering, *Journal of Geophysical Research: Earth Surface*, *120*(4), 655–670, doi:10.1002/2014JF003291.

Blankenship, D. D., C. R. Bentley, S. T. Rooney, and R. B. Alley (1986), Seismic measurements reveal a saturated porous layer beneath an active Antarctic ice stream, *Nature*, *322*(6074), 54–57, doi:10.1038/322054a0.

Blatter, H. (1995), Velocity and stress fields in grounded glaciers- a simple algorithm for including deviatoric stress gradients, *Journal of Glaciology*, *41*(138), 333–344.

Bo, S., M. Siegert, S. Mudd, D. Sugden, S. Fujita, C. Xiangbin, J. Yunyun, T. Xueyuan, and L. Yuansheng (2009), The Gamburtsev mountains and the origin and early evolution of the Antarctic Ice Sheet, *Nature*, *459*(7247), 690–693, doi:10.1038/nature08024.

Bougamont, M., S. Tulaczyk, and I. Joughin (2003), Response of subglacial sediments to basal freeze-on 2. Application in numerical modeling of the recent stoppage of Ice Stream C, West Antarctica, *Journal of Geophysical Research: Solid Earth*, *108*(B4), doi: 10.1029/2002JB001936.

Boulton, G. S., and R. C. A. Hindmarsh (1987), Sediment deformation beneath glaciers: Rheology and geological consequences, *Journal of Geophysical Research: Solid Earth*, *92*(B9), 9059–9082, doi:10.1029/JB092iB09p09059.

Bowman, A., and A. Azzalini (1997), *Applied Smoothing Techniques for Data Analysis*, Oxford University Press, New York.

Budd, W. F., and R. C. Warner (1996), A computer scheme for rapid calculations of balance-flux distributions, *Annals of Glaciology*, *23*, 21–27.

Bueler, E., and J. Brown (2009), Shallow shelf approximation as a "sliding law" in a thermomechanically coupled ice sheet model, *Journal of Geophysical Research: Earth Surface*, *114*(F3), F03,008, doi:10.1029/2008JF001179.

Carter, S., D. Blankenship, M. Peters, D. Young, J. Holt, and D. Morse (2007), Radar-based subglacial lake classification in Antarctica, *Geochemistry Geophysics Geosystems*, *8*, doi:10.1029/2006GC001408.

Catania, G., C. Hulbe, and H. Conway (2010), Grounding-line basal melt rates determined using radar-derived internal stratigraphy, *Journal of Glaciology*, *56*(197), 545–554, doi: doi:10.3189/002214310792447842.

Catania, G. A., H. Conway, C. F. Raymond, and T. A. Scambos (2006), Evidence for floatation or near floatation in the mouth of Kamb Ice Stream, West Antarctica, prior to stagnation, *Journal of Geophysical Research: Earth Surface*, *111*(F1), F01,005, doi: 10.1029/2005JF000355.

Christianson, K., B. R. Parizek, R. B. Alley, H. J. Horgan, R. W. Jacobel, S. Anandakrishnan, B. A. Keisling, B. D. Craig, and A. Muto (2013), Ice sheet grounding zone stabilization due to till compaction, *Geophysical Research Letters*, *40*(20), 5406–5411, doi: 10.1002/2013GL057447.

Christianson, K., L. E. Peters, R. B. Alley, S. Anandakrishnan, R. W. Jacobel, K. L. Riverman, A. Muto, and B. A. Keisling (2014), Dilatant till facilitates ice-stream flow in northeast Greenland, *Earth and Planetary Science Letters*, *401*(0), 57 – 69, doi: 10.1016/j.epsl.2014.05.060.

Christoffersen, P., S. Tulaczyk, and A. Behar (2010), Basal ice sequences in Antarctic ice stream: Exposure of past hydrologic conditions and a principal mode of sediment transfer, *Journal of Geophysical Research: Earth Surface*, *115*(F3), F03,034, doi: 10.1029/2009JF001430.

Chu, V. W., L. C. Smith, A. K. Rennermalm, R. R. Forster, J. E. Box, and N. Reehy (2009), Sediment plume response to surface melting and supraglacial lake drainages on the Greenland ice sheet, *Journal of Glaciology*, *55*(194), 1072–1082, doi: 10.3189/002214309790794904.

Clark, C. D. (2010), Emergent drumlins and their clones: from till dilatancy to flow instabilities, *Journal of Glaciology*, *56*(200), 1011–1025, doi:10.3189/002214311796406068.

Clarke, G. (2005), Subglacial processes, *Annual Review of Earth and Planetary Sciences*, *33*, 247–276, doi:10.1146/annurev.earth.33.092203.122621.

Clarke, G. K. C., U. Nitsan, and W. Paterson (1977), Strain heating and creep instability in glaciers and ice sheets, *Reviews of geophysics*, *15*(2), 235–247, doi: 10.1029/RG015i002p00235.

Clarke, G. K. C., N. Lhomme, and S. J. Marshall (2005), Tracer transport in the Greenland ice sheet: three-dimensional isotopic stratigraphy, *Quaternary Science Reviews*, *24*(1–2), 155 – 171, doi:10.1016/j.quascirev.2004.08.021.

Clough, J. (1977), Radio-echo sounding: reflections from internal layers in ice sheets, *Journal of Glaciology*, *18*(78), 3–14.

Clow, G. D., K. M. Cuffey, and E. D. Waddington (2012), High heat-flow beneath the central portion of the West Antarctic Ice Sheet, *AGU Fall Meeting Abstracts*, p. A577, c31A-0577.

Cohen, D., T. S. Hooyer, N. R. Iverson, J. F. Thomason, and M. Jackson (2006), Role of transient water pressure in quarrying: A subglacial experiment using acoustic emissions, *Journal of Geophysical Research- Earth Surface*, *111*(F3), doi:10.1029/2005JF000439.

Comiso, J. C. (2000), Variability and trends in Antarctic surface temperatures from in situ and satellite infrared measurements, *Journal of Climate*, *13*(10), 1674–1696, doi: 10.1175/1520-0442.

Conway, H., B. L. Hall, G. H. Denton, A. M. Gades, and E. D. Waddington (1999), Past and future grounding-line retreat of the West Antarctic Ice Sheet, *Science*, *286*(5438), 280–283, doi:10.1126/science.286.5438.280.

Conway, H., G. Catania, C. F. Raymond, A. M. Gades, T. A. Scambos, and H. Engelhardt (2002), Switch of flow direction in an Antarctic ice stream, *Nature*, *419*(6906), 465–467, doi:10.1038/nature01081.

Cox, S., S. Thomson, P. Reiners, S. Hemming, and T. van de Flierdt (2010), Extremely low long-term erosion rates around the Gamburtsev Mountains in interior East Antarctica, *Geophysical Research Letters*, *37*, doi:10.1029/2010GL045106.

Creyts, T. T., and G. K. C. Clarke (2010), Hydraulics of subglacial supercooling: Theory and simulations for clear water flows, *Journal of Geophysical Research: Earth Surface*, *115*(F3), F03,021, doi:10.1029/2009JF001417.

Creyts, T. T., and C. G. Schoof (2009), Drainage through subglacial water sheets, *Journal of Geophysical Research-Earth Surface*, *114*(F4), F04,008, doi:10.1029/2008JF001215.

Creyts, T. T., G. K. C. Clarke, and M. Church (2013), Evolution of subglacial overdeepenings in response to sediment redistribution and glaciohydraulic supercooling, *Journal of Geophysical Research: Earth Surface*, *118*(2), 423–446, doi:10.1002/jgrf.20033.

Creyts, T. T., F. Ferraccioli, R. E. Bell, M. Wolovick, H. Corr, K. C. Rose, N. Frearson, D. Damaske, T. Jordan, D. Braaten, and C. Finn (2014), Freezing of ridges and water networks preserves the Gamburtsev Subglacial Mountains for millions of years, *Geophysical Research Letters*, *41*(22), 8114–8122, doi:10.1002/2014GL061491.

Cuffey, K., and W. Paterson (2010), *The Physics of Glaciers*, 4 ed., Butterworth-Heineman/Elsevier, Burlington, MA.

Cuffey, K., H. Conway, A. Gades, B. Hallet, R. Lorrain, J. Severinghaus, E. Steig, B. Vaughn, and J. White (2000), Entrainment at cold glacier beds, *Geology*, *28*(4), 351–354, doi:10.1130/0091-7613(2000)028.

Dahl-Jensen, D. (1989), Steady thermomechanical flow along two-dimensional flow lines in large grounded ice sheets, *Journal of Geophysical Research: Solid Earth*, *94*(B8), 10,355–10,362, doi:10.1029/JB094iB08p10355.

Dahl-Jensen, D., T. Thorsteinsson, R. Alley, and H. Shoji (1997), Flow properties of the ice from the Greenland Ice Core Project ice core: The reason for folds?, *Journal of Geophysical Research: Oceans*, *102*(C12), 26,831–26,840, doi:10.1029/97JC01266.

Dahl-Jensen, D., N. Gundestrup, S. P. Gogineni, and H. Miller (2003), Basal melt at North-GRIP modeled from borehole, ice-core and radio-echo sounder observations, *Annals of Glaciology*, *37*(1), 207–212, doi:10.3189/172756403781815492.

Das, I., R. E. Bell, T. A. Scambos, M. Wolovick, T. T. Creyts, M. Studinger, N. Frearson, J. P. Nicolas, J. T. M. Lenaerts, and M. R. van den Broeke (2013), Influence of persistent wind scour on the surface mass balance of Antarctica, *Nature Geoscience*, *6*(5), 367–371, doi:10.1038/ngeo1766.

Dowdeswell, J., and M. Siegert (1999), The dimensions and topographic setting of Antarctic subglacial lakes and implications for large-scale water storage beneath continental ice sheets, *Geological Society of America Bulletin*, *111*(2), 254–263, doi:10.1130/0016-7606.

Dowdeswell, J. A., and M. Siegert (2003), The physiography of modern Antarctic subglacial lakes, *Global and Planetary Change*, *35*(3-4), 221–236, symposium on Subglacial Lakes, San Francisco, CA.

Drewry, D. J., and D. T. Meldrum (1978), Antarctic airborne radio echo sounding, 1977–78, *Polar Record*, *19*(120), 267–273, doi:10.1017/S0032247400018271.

Drews, R., O. Eisen, I. Weikusat, S. Kipfstuhl, A. Lambrecht, D. Steinhage, F. Wilhelms, and H. Miller (2009), Layer disturbances and the radio-echo free zone in ice sheets, *The Cryosphere*, *3*(2), 195–203, doi:10.5194/tc-3-195-2009.

Engelhardt, H., N. Humphrey, B. Kamb, and M. Fahnestock (1990), Physical conditions at the base of a fast moving Antarctic ice stream, *Science*, *248*(4951), 57–59, doi:10.1126/science.248.4951.57.

Evans, S., and G. d. Q. Robin (1966), Glacier depth-sounding from the air, *Nature*, *210*(5039), 883–885, doi:10.1038/210883a0.

Fahnestock, M., W. Abdalati, I. Joughin, J. Brozena, and P. Gogineni (2001), High geothermal heat flow, basal melt, and the origin of rapid ice flow in central Greenland, *Science*, *294*(5550), 2338–2342, doi:10.1126/science.1065370.

Faria, S. H., J. Freitag, and S. Kipfstuhl (2010), Polar ice structure and the integrity of ice-core paleoclimate records, *Quaternary Science Reviews*, *29*(1-2), 338 – 351, doi:10.1016/j.quascirev.2009.10.016.

Ferraccioli, F., C. Finn, T. Jordan, R. Bell, L. Anderson, and D. Damaske (2011), East Antarctic rifting triggers uplift of the Gamburtsev Mountains, *Nature*, *479*(7373), 388–U139, doi:10.1038/nature10566.

Fischer, H., J. Severinghaus, E. Brook, E. Wolff, M. Albert, O. Alemany, R. Arthern, C. Bentley, D. Blankenship, J. Chappellaz, T. Creyts, D. Dahl-Jensen, M. Dinn, M. Frezzotti, S. Fujita, H. Gallee, R. Hindmarsh, D. Hudspeth, G. Jugie, and K. Kawamura (2013), Where to find 1.5 million yr old ice for the IPICS "Oldest-Ice" ice core, *Climate of the Past*, *9*(6), 2489–2505, doi:10.5194/cp-9-2489-2013.

Flowers, G., and G. Clarke (1999), Surface and bed topography of Trapridge Glacier, Yukon Territory, Canada: digital elevation models and derived hydraulic geometry, *Journal of Glaciology*, *45*(149), 165–174.

Fowler, A. (1986), Sub-temperate basal sliding, *Journal of Glaciology*, *32*(110), 3–5.

Fowler, A. (1987), Sliding with cavity formation, *Journal of Glaciology*, *33*(115), 255–267.

Fowler, A. (2010), Weertman, Lliboutry and the development of sliding theory, *Journal of Glaciology*, *56*(200), 965–972, doi:10.3189/002214311796406112.

Fowler, A., and D. Larson (1978), On the flow of polythermal glaciers. I. Model and preliminary analysis, *Proceedings of the Royal Society. A, Mathematical, physical, and engineering sciences*, *363*(1713), 217–242, doi:10.1098/rspa.1978.0165.

Fretwell, P., H. D. Pritchard, D. G. Vaughan, J. L. Bamber, N. E. Barrand, R. Bell, C. Bianchi, R. G. Bingham, D. D. Blankenship, G. Casassa, G. Catania, D. Callens, H. Conway, A. J. Cook, H. F. J. Corr, D. Damaske, V. Damm, F. Ferraccioli, R. Forsberg, and S. Fujita (2013), Bedmap2: improved ice bed, surface and thickness datasets for Antarctica., *The Cryosphere*, *7*(1), 375 – 393, doi:10.5194/tc-7-375-2013.

Fricker, H., T. Scambos, R. Bindschadler, and L. Padman (2007), An active subglacial water system in West Antarctica mapped from space, *Science*, *315*(5818), 1544–1548, doi:10.1126/science.1136897.

Fricker, H., T. Scambos, S. Carter, C. Davis, T. Haran, and I. Joughin (2010), Synthesizing multiple remote-sensing techniques for subglacial hydrologic mapping: application to a lake system beneath MacAyeal Ice Stream, West Antarctica, *Journal of Glaciology*, *56*(196), 187–199, doi:10.3189/002214310791968557.

Fricker, H. A., and T. Scambos (2009), Connected subglacial lake activity on lower Mercer and Whillans Ice Streams, West Antarctica, 2003-2008, *Journal of Glaciology*, *55*(190), 303–315, doi:10.3189/002214309788608813.

Fricker, H. A., S. P. Carter, R. E. Bell, and T. Scambos (2014), Active lakes of Recovery Ice Stream, East Antarctica: a bedrock-controlled subglacial hydrological system, *Journal of Glaciology*, *60*(223), 1015–1030, doi:10.3189/2014JoG14J063.

Gerya, T. (2010), *Introduction to Numerical Geodynamic Modelling*, 1 ed., Cambridge University Press.

Gillet-Chaulet, F., R. C. A. Hindmarsh, H. F. J. Corr, E. C. King, and A. Jenkins (2011), In-situ quantification of ice rheology and direct measurement of the Raymond Effect at Summit, Greenland using a phase-sensitive radar, *Geophysical Research Letters*, *38*(24), L24,503, doi:10.1029/2011GL049843.

Glen, J. W. (1953), Rate of flow of polycrystalline ice, *Nature*, *172*(4381), 721–722, doi:10.1038/172721a0.

Gogineni, S., T. Chuah, C. Allen, K. Jezek, and R. Moore (1998), An improved coherent radar depth sounder, *Journal of Glaciology*, *44*(148), 659–669.

Gogineni, S., D. Tammana, D. Braaten, C. Leuschen, T. Akins, J. Legarsky, P. Kanagaratnam, J. Stiles, C. Allen, and K. Jezek (2001), Coherent radar ice thickness measurements over the Greenland ice sheet, *Journal of Geophysical Research: Atmospheres*, *106*(D24), 33,761–33,772, doi:10.1029/2001JD900183.

Gorman, M. R., and M. J. Siegert (1999), Penetration of Antarctic subglacial lakes by VHF electromagnetic pulses: Information on the depth and electrical conductivity of basal water bodies, *Journal of Geophysical Research: Solid Earth*, *104*(B12), 29,311–29,320, doi:10.1029/1999JB900271.

Gray, L., I. Joughin, S. Tulaczyk, V. Spikes, R. Bindschadler, and K. Jezek (2005), Evidence for subglacial water transport in the West Antarctic Ice Sheet through three-dimensional satellite radar interferometry, *Geophysical Research Letters*, *32*(3), L03,501, doi:10.1029/2004GL021387.

Grootes, P. M., M. Stuiver, J. W. C. White, S. Johnsen, and J. Jouzel (1993), Comparison of oxygen isotope records from the GISP2 and GRIP Greenland ice cores, *Nature*, *366*(6455), 552–554, doi:10.1038/366552a0.

Gudmundsson, G. (1997), Basal-flow characteristics of a non-linear flow sliding frictionless over strongly undulating bedrock, *Journal of Glaciology*, *43*(143), 80–89.

Hallet, B. (1979), A theoretical model of glacial abrasion, *Journal of Glaciology*, *23*, 39–50.

Hallet, B. (1996), Glacial quarrying: A simple theoretical model, *Annals of Glaciology*, *22*, 1–8.

Heliere, F., C. Lin, H. Corr, and D. Vaughan (2007), Radio echo sounding of Pine Island Glacier, West Antarctica: Aperture synthesis processing and analysis of feasibility from space, *IEEE Transactions on Geoscience and Remote Sensing*, *45*(8), 2573–2582, doi: 10.1109/TGRS.2007.897433.

Hemming, S. R. (2004), Heinrich events: Massive late Pleistocene detritus layers of the North Atlantic and their global climate imprint, *Reviews of Geophysics*, *42*(1), RG1005, doi:10.1029/2003RG000128.

Hewitt, I. J. (2013), Seasonal changes in ice sheet motion due to melt water lubrication, *Earth and Planetary Science Letters*, *371–372*, 16 – 25, doi:10.1016/j.epsl.2013.04.022.

Hindmarsh, R. C., G. J. Leysinger Vieli, M. J. Raymond, and G. H. Gudmundsson (2006), Draping or overriding: the effect of horizontal stress gradients on internal layer architecture in ice sheets., *Journal of Geophysical Research: Earth Surface.*, *111*(F2), F02,018, doi: 10.1029/2005JF000309.

Hindmarsh, R. C., G. J.-M. Leysinger Vieli, and F. Parrenin (2009), A large-scale numerical model for computing isochrone geometry, *Annals of Glaciology*, *50*(51), 130–140, doi: 10.3189/172756409789097450.

Hindmarsh, R. C. A., E. C. King, R. Mulvaney, H. F. J. Corr, G. Hiess, and F. Gillet-Chaulet (2011), Flow at ice-divide triple junctions: 2. Three-dimensional views of isochrone architecture from ice-penetrating radar surveys, *Journal of Geophysical Research: Earth Surface*, *116*(F2), F02,024, doi:10.1029/2009JF001622.

Hodge, S., D. Wright, J. Bradley, R. Jacobel, N. Skou, and B. Vaughn (1990), Determination of the surface and bed topography in central Greenland, *Journal of Glaciology*, *36*(122), 17–30.

Hooke, R. (1991), Positive feedbacks associated with erosion of glacial cirques and overdeepenings, *Geological Society of America bulletin*, *103*(8), 1104–1108, doi:10.1130/0016-7606.

Hutter, K. (1981), The effect of longitudinal stress on the shear stress of an ice sheet: in defence of using stretched co-ordinate, *Journal of Glaciology*, *27*(95), 39–56.

Iken, A. (1981), The effect of the subglacial water pressure on the sliding velocity of a glacier in an idealized numerical model, *Journal of Glaciology*, *27*(97), 407–421.

Iverson, N. (1998), Ring-shear studies of till deformation: Coulomb-plastic behavior and distributed strain in glacier beds, *Journal of Glaciology*, *44*(148), 634–642.

Jacobel, R. W., K. E. Lapo, J. R. Stamp, B. W. Youngblood, B. C. Welch, and J. L. Bamber (2010), A comparison of basal reflectivity and ice velocity in East Antarctica, *The Cryosphere*, *4*(4), 447–452, doi:10.5194/tc-4-447-2010.

Jacobson, H., and E. Waddington (2005), Recumbent folding of divide arches in response to unsteady ice-divide migration, *Journal of Glaciology*, *51*(173), 201–209, doi:10.3189/172756505781829412.

Jacobson, H. P., and E. D. Waddington (2004), Recumbent folding in ice sheets: a coreferential study, *Journal of Glaciology*, *50*(168), 3–16, doi:10.3189/172756504781830204.

Jamieson, S., D. Sugden, and N. Hulton (2010), The evolution of the subglacial landscape of Antarctica, *Earth and Planetary Science Letters*, *293*(1-2), 1–27, doi:10.1016/j.epsl.2010.02.012.

Jankowski, E. J., and D. J. Drewry (1981), The structure of West Antarctica from geophysical studies, *Nature*, *291*(5810), 17–21, doi:10.1038/291017a0.

Jaupart, C., and J.-C. Mareschal (2007), 6.05 - Heat flow and thermal structure of the lithosphere, in *Treatise on Geophysics*, edited by G. Schubert, pp. 217 – 251, Elsevier, Amsterdam, doi:10.1016/B978-044452748-6.00104-8.

Jenkins, A. (2011), Convection-driven melting near the grounding lines of ice shelves and tidewater glaciers, *Journal of Physical Oceanography*, *41*(12), 2279–2294, doi:10.1175/JPO-D-11-03.1.

Jezek, K., E. Rodriguez, S. Gogineni, A. Freeman, J. Curlander, X. Wu, J. Paden, and C. Allen (2006), Glaciers and Ice Sheets Mapping Orbiter concept, *Journal of Geophysical Research: Planets*, *111*(E6), E06S20, doi:10.1029/2005JE002572.

Joughin, I., S. Tulaczyk, D. R. MacAyeal, and H. Engelhardt (2004a), Melting and freezing beneath the Ross ice streams, Antarctica, *Journal of Glaciology*, *50*(168), 96–108, doi:10.3189/172756504781830295.

Joughin, I., D. MacAyeal, and S. Tulaczyk (2004b), Basal shear stress of the Ross ice streams from control method inversions, *Journal of Geophysical Research: Solid Earth*, *109*(B9), doi:10.1029/2003JB002960.

Joughin, I., S. Tulaczyk, J. L. Bamber, D. Blankenship, J. W. Holt, T. Scambos, and D. G. Vaughan (2009), Basal conditions for Pine Island and Thwaites Glaciers, West Antarctica, determined using satellite and airborne data, *Journal of Glaciology*, *55*(190), 245–257, doi:10.3189/002214309788608705.

Joughin, I., B. E. Smith, I. M. Howat, T. Scambos, and T. Moon (2010), Greenland flow variability from ice-sheet-wide velocity mapping, *Journal of Glaciology*, *56*(197), 415–430, doi:10.3189/002214310792447734.

Jouzel, J., J. R. Petit, R. Souchez, N. I. Barkov, V. Y. Lipenkov, D. Raynaud, M. Stievenard, N. I. Vassiliev, V. Verbeke, and F. Vimeux (1999), More than 200 meters of lake ice above Subglacial Lake Vostok, Antarctica, *Science*, *286*(5447), 2138–2141, doi:10.1126/science.286.5447.2138.

Kamb, B. (1987), Glacier surge mechanism based on linked cavity configuration of the basal water conduit system, *Journal of Geophysical Research: Solid Earth and Planets*, *92*(B9), 9083–9100, doi:10.1029/JB092iB09p09083.

Kamb, B. (1991), Rheological nonlinearity and flow instability in the deforming bed mechanism of ice stream motion, *Journal of Geophysical Research: Solid Earth*, *96*(B10), 16,585–16,595, doi:10.1029/91JB00946.

Kamb, B., and K. Echelmeyer (1986), Stress-gradient coupling in glacier flow. 1. Longitudinal averaging of the influence of ice thickness and surface slope, *Journal of Glaciology*, *32*(111), 267–284.

Kapitsa, A. P., J. K. Ridley, G. de Q. Robin, M. J. Siegert, and I. A. Zotikov (1996), A large deep freshwater lake beneath the ice of central East Antarctica, *Nature*, *381*(6584), 684–686, doi:10.1038/381684a0.

Karlsson, N. B., J. W. Holt, and R. C. A. Hindmarsh (2011), Testing for flow in the north polar layered deposits of Mars using radar stratigraphy and a simple 3d ice-flow model, *Geophysical Research Letters*, *38*(24), L24,204, doi:10.1029/2011GL049630.

Karlsson, N. B., D. Dahl-Jensen, S. P. Gogineni, and J. D. Paden (2013), Tracing the depth of the Holocene ice in North Greenland from radio-echo sounding data, *Annals of Glaciology*, *54*(64), 44–50, doi:10.3189/2013AoG64A057.

Keisling, B. A., K. Christianson, R. B. Alley, L. E. Peters, J. E. Christian, S. Anandakrishnan, K. L. Riverman, A. Muto, and R. W. Jacobel (2014), Basal conditions and ice dynamics inferred from radar-derived internal stratigraphy of the northeast Greenland ice stream, *Annals of Glaciology*, *55*(67), 127–137, doi:10.3189/2014AoG67A090.

Kingslake, J., R. C. A. Hindmarsh, G. Adalgeirsdottir, H. Conway, H. F. J. Corr, F. Gillet-Chaulet, C. Martin, E. C. King, R. Mulvaney, and H. D. Pritchard (2014), Full-depth englacial vertical ice sheet velocities measured using phase-sensitive radar, *Journal of Geophysical Research: Earth Surface*, *119*(12), 2604–2618, doi:10.1002/2014JF003275.

Koutnik, M. R., E. D. Waddington, and D. P. Winebrenner (2009), A method to infer past surface mass balance and topography from internal layers in martian polar layered deposits, *Icarus*, *204*(2), 458 – 470, doi:10.1016/j.icarus.2009.06.019.

Langley, K., J. Kohler, K. Matsuoka, A. Sinisalo, T. Scambos, T. Neumann, A. Muto, J. G. Winther, and M. Albert (2011), Recovery Lakes, East Antarctica: Radar assessment of sub-glacial water extent, *Geophysical Research Letters*, *38*(5), L05,501, doi:10.1029/2010GL046094.

Lawson, D. E., J. C. Strasser, E. B. Evenson, R. B. Alley, G. J. Larson, and S. A. Arcone (1998), Glaciohydraulic supercooling: a freeze-on mechanism to create stratified, debris-rich basal ice: I. Field evidence, *Journal of Glaciology*, *44*(148), 547–562.

Le Brocq, A. M., A. J. Payne, M. J. Siegert, and R. B. Alley (2009), A subglacial water-flow model for West Antarctica, *Journal of Glaciology*, *55*(193), 879–888, doi: 10.3189/002214309790152564.

Le Brocq, A. M., A. J. Payne, and A. Vieli (2010), An improved Antarctic dataset for high resolution numerical ice sheet models (ALBMAP v1), *Earth System Science Data*, *2*(2), 247–260, doi:10.5194/essd-2-247-2010.

Legarsky, J., A. Wong, T. Akins, and S. Gogineni (1998), Detection of hills from radar data in central-northern Greenland, *Journal of Glaciology*, *44*(146), 182–184.

Letreguilly, A., P. Huybrechts, and N. Reeh (1991), Steady-state characteristics of the Greenland Ice Sheet under different climates, *Journal of Glaciology*, *37*(125), 149–157.

Lewis, A. R., D. R. Marchant, D. E. Kowalewski, S. L. Baldwin, and L. E. Webb (2006), The age and origin of the Labyrinth, western Dry Valleys, Antarctica: Evidence for extensive middle Miocene subglacial floods and freshwater discharge to the Southern Ocean, *Geology*, *34*(7), 513–516, doi:10.1130/G22145.1.

Leysinger Vieli, G., R. Hindmarsh, and M. Siegert (2007), Three-dimensional flow influences on radar layer stratigraphy, *Annals of Glaciology*, *46*(1), 22–28, doi: 10.3189/172756407782871729.

Leysinger Vieli, G. J. M. C., R. C. A. Hindmarsh, M. J. Siegert, and S. Bo (2011), Time-dependence of the spatial pattern of accumulation rate in East Antarctica deduced from isochronic radar layers using a 3-D numerical ice flow model, *Journal of Geophysical Research: Earth Surface*, *116*, doi:10.1029/2010JF001785.

Li, J., J. Paden, C. Leuschen, F. Rodriguez-Morales, R. D. Hale, E. J. Arnold, R. Crowe, D. Gomez-Garcia, and P. Gogineni (2013), High-altitude radar measurements of ice thickness over the Antarctic and Greenland Ice Sheets as a part of Operation IceBridge, *IEEE Transactions on Geoscience and Remote Sensing*, *51*(2), 742 –754, doi: 10.1109/TGRS.2012.2203822.

Lliboutry, L. (1968), General theory of subglacial cavitation and sliding of temperate glaciers, *Journal of Glaciology*, *7*(49), 21–58.

Lythe, M. B., and D. G. Vaughan (2001), BEDMAP: A new ice thickness and subglacial topographic model of Antarctica, *Journal of Geophysical Research: Solid Earth*, *106*(B6), 11,335–11,351, doi:10.1029/2000JB900449.

MacAyeal, D. (1993), A tutorial on the use of control methods in ice-sheet modeling, *Journal of Glaciology*, *39*(131), 91–98.

MacAyeal, D. R. (1989), Large-scale ice flow over a viscous basal sediment: Theory and application to ice stream B, Antarctica, *Journal of Geophysical Research: Solid Earth*, *94*(B4), 4071–4087, doi:10.1029/JB094iB04p04071.

MacGregor, J., D. Winebrenner, H. Conway, K. Matsuoka, P. Mayewski, and G. Clow (2007), Modeling englacial radar attenuation at Siple Dome, West Antarctica, using ice chemistry and temperature data, *Journal of Geophysical Research: Earth Surface*, *112*(F3), doi:10.1029/2006JF000717.

MacGregor, J. A., K. Matsuoka, and M. Studinger (2009a), Radar detection of accreted ice over Lake Vostok, Antarctica, *Earth and Planetary Science Letters*, *282*(1-4), 222–233, doi:10.1016/j.epsl.2009.03.018.

MacGregor, J. A., K. Matsuoka, M. R. Koutnik, E. D. Waddington, M. Studinger, and D. P. Winebrenner (2009b), Millennially averaged accumulation rates for the Vostok Subglacial Lake region inferred from deep internal layers, *Annals of Glaciology*, *50*(51), 25–34, doi:10.3189/172756409789097441.

MacGregor, J. A., K. Matsuoka, E. D. Waddington, D. P. Winebrenner, and F. Pattyn (2012), Spatial variation of englacial radar attenuation: Modeling approach and application to the Vostok flowline, *Journal of Geophysical Research: Earth Surface*, *117*(F3), F03,022, doi:10.1029/2011JF002327.

MacGregor, J. A., M. A. Fahnestock, G. A. Catania, J. D. Paden, S. Prasad Gogineni, S. K. Young, S. C. Rybarski, A. N. Mabrey, B. M. Wagman, and M. Morlighem (2015a), Radiostratigraphy and age structure of the Greenland Ice Sheet, *Journal of Geophysical Research: Earth Surface*, *120*(2), 212–241, doi:10.1002/2014JF003215.

MacGregor, J. A., J. Li, J. D. Paden, G. A. Catania, G. D. Clow, M. A. Fahnestock, S. P. Gogineni, R. E. Grimm, M. Morlighem, S. Nandi, H. Seroussi, and D. E. Stillman (2015b), Radar attenuation and temperature within the Greenland Ice Sheet, *Journal of Geophysical Research: Earth Surface*, *120*(6), 983–1008, doi:10.1002/2014JF003418.

Matsuoka, K. (2011), Pitfalls in radar diagnosis of ice-sheet bed conditions: Lessons from englacial attenuation models, *Geophysical Research Letters*, *38*(5), L05,505, doi:10.1029/2010GL046205.

Matsuoka, K., S. Uratsuka, S. Fujita, and F. Nishio (2004), Ice-flow-induced scattering zone within the Antarctic ice sheet revealed by high-frequency airborne radar, *Journal of Glaciology*, *50*(170), 382–388, doi:10.3189/172756504781829891.

Matsuoka, K., D. Morse, and C. F. Raymond (2010), Estimating englacial radar attenuation using depth profiles of the returned power, central West Antarctica, *Journal of Geophysical Research- Earth Surface*, *115*, doi:10.1029/2009JF001496.

Maule, C. F., M. E. Purucker, N. Olsen, and K. Mosegaard (2005), Heat flux anomalies in Antarctica revealed by satellite magnetic data, *Science*, *309*(5733), 464–467, doi:10.1126/science.1106888.

McGrath, D., W. Colgan, K. Steffen, P. Lauffenburger, and J. Balog (2011), Assessing the summer water budget of a moulin basin in the Sermeq Avannarleq ablation region, Greenland ice sheet, *Journal of Glaciology*, *57*(205), 954–964, doi:10.3189/002214311798043735.

Meierbachtol, T., J. Harper, and N. Humphrey (2013), Basal drainage system response to increasing surface melt on the Greenland Ice Sheet, *Science*, *341*(6147), 777–779, doi:10.1126/science.1235905.

Millar, D. H. M. (1981), Radio-echo layering in polar ice sheets and past volcanic activity, *Nature*, *292*(5822), 441–443, doi:10.1038/292441a0.

Montagnat, M., N. Azuma, D. Dahl-Jensen, J. Eichler, S. Fujita, F. Gillet-Chaulet, S. Kipfstuhl, D. Samyn, A. Svensson, and I. Weikusat (2014), Fabric along the NEEM ice core, Greenland, and its comparison with GRIP and NGRIP ice cores, *The Cryosphere*, *8*(4), 1129–1138, doi:10.5194/tc-8-1129-2014.

Morgan, V., C. Wookey, J. Li, T. van Ommen, W. Skinner, and M. Fitzpatrick (1997), Site information and initial results from deep ice drilling on Law Dome, Antarctica, *Journal of Glaciology*, *43*(143), 3–10.

Morlighem, M., E. Rignot, J. Mouginot, H. Seroussi, and E. Larour (2014), Deeply incised submarine glacial valleys beneath the Greenland ice sheet, *Nature Geoscience*, *7*(6), 418–422, doi:10.1038/ngeo2167.

Mulvaney, R., O. Alemany, and P. Possenti (2007), The Berkner Island (Antarctica) ice-core drilling project, *Annals of Glaciology*, *47*(1), 115–124, doi:doi:10.3189/172756407786857758.

NEEM Community Members, . (2013), Eemian interglacial reconstructed from a Greenland folded ice core., *Nature*, *493*(7433), 489–494, doi:10.1038/nature11789.

Neumann, T. A., H. Conway, S. F. Price, E. D. Waddington, G. A. Catania, and D. L. Morse (2008), Holocene accumulation and ice sheet dynamics in central West Antarctica, *Journal of Geophysical Research: Earth Surface*, *113*(F2), F02,018, doi:10.1029/2007JF000764.

Ng, F., and H. Conway (2004), Fast-flow signature in the stagnated Kamb Ice Stream, West Antarctica, *Geology*, *32*(6), 481–484, doi:10.1130/G20317.1.

Ng, F., and E. C. King (2011), Kinematic waves in polar firn stratigraphy, *Journal of Glaciology*, *57*(206), 1119–1134, doi:10.3189/002214311798843340.

Noel, B., W. J. van de Berg, E. van Meijgaard, P. Kuipers Munneke, R. S. W. van de Wal, and M. R. van den Broeke (2015), Evaluation of the updated regional climate model RACMO2.3: summer snowfall impact on the Greenland Ice Sheet, *The Cryosphere*, *9*(5), 1831–1844, doi:10.5194/tc-9-1831-2015.

Nye, J. (1959), The motion of ice sheets and glaciers, *Journal of Glaciology*, *3*(26), 493–507.

Nye, J. (1976), Water flow in glaciers: jokulhlaups, tunnels, and veins, *Journal of Glaciology*, *17*(76), 181–207.

Oswald, G., and S. Gogineni (2008), Recovery of subglacial water extent from Greenland radar survey data, *Journal of Glaciology*, *54*(184), 94–106, doi: 10.3189/002214308784409107.

Oswald, G., and G. Robin (1973), Lakes beneath Antarctic Ice Sheet, *Nature*, *245*(5423), 251–254, doi:10.1038/245251a0.

Parrenin, F., and R. Hindmarsh (2007), Influence of a non-uniform velocity field on isochrone geometry along a steady flowline of an ice sheet, *Journal of Glaciology*, *53*(183), 612–622, doi:10.3189/002214307784409298.

Parrenin, F., R. Hindmarsh, and F. Remy (2006), Analytical solutions for the effect of topography, accumulation rate and lateral flow divergence on isochrone layer geometry, *Journal of Glaciology*, *52*(177), 191–202, doi:10.3189/172756506781828728.

Pattyn, F. (2002), Transient glacier response with a higher-order numerical ice-flow model, *Journal of Glaciology*, *48*(162), 467–477, doi:10.3189/172756502781831278.

Pattyn, F. (2010), Antarctic subglacial conditions inferred from a hybrid ice sheet/ice stream model, *Earth and Planetary Science Letters*, *295*(3-4), 451–461, doi: 10.1016/j.epsl.2010.04.025.

Peltier, W. (2004), Global glacial isostasy and the surface of the ice-age Earth: the ICE-5g model and GRACE, *Annual Review of Earth and Planetary Sciences*, *32*(1), 111–149, doi:10.1146/annurev.earth.32.082503.144359.

Peters, M., D. Blankenship, and D. Morse (2005), Analysis techniques for coherent airborne radar sounding: Application to West Antarctic ice streams, *Journal of Geophysical Research: Solid Earth*, *110*(B6), B06,303, doi:10.1029/2004JB003222.

Phillips, R. J., B. J. Davis, K. L. Tanaka, S. Byrne, M. T. Mellon, N. E. Putzig, R. M. Haberle, M. A. Kahre, B. A. Campbell, L. M. Carter, I. B. Smith, J. W. Holt, S. E. Smrekar, D. C. Nunes, J. J. Plaut, A. F. Egan, T. N. Titus, and R. Seu (2011), Massive CO2 ice deposits sequestered in the South Polar Layered Deposits of Mars, *Science*, *332*(6031), 838–841, doi:10.1126/science.1203091.

Pollard, D., and R. M. DeConto (2009), Modelling West Antarctic ice sheet growth and collapse through the past five million years, *Nature*, *458*(7236), 329–332, doi: 10.1038/nature07809.

Popov, S., and V. Masolov (2007), Forty-seven new subglacial lakes in the 0-110 degrees E sector of East Antarctica, *Journal of Glaciology*, *53*(181), 289–297, doi: 10.3189/172756507782202856.

Quinn, P., K. Beven, P. Chevallier, and O. Planchon (1991), The prediction of hillslope flow paths for distributed hydrological modeling using digital terrain models, *Hydrological Processes*, *5*(1), 59–79, doi:10.1002/hyp.3360050106.

Raymond, C. (1983), Deformation in the vicinity of ice divides, *Journal of glaciology*, *29*(103), 357–373.

Reeh, N. (1988), A flow-line model for calculating the surface profile and the velocity, strain-rate, and stress fields in an ice sheet, *Journal of Glaciology*, *34*(116), 46–54.

Reeh, N. (1989), The age-depth profile in the upper part of a steady-state ice sheet, *Journal of Glaciology*, *35*(121), 406–417.

Rempel, A. W. (2008), A theory for ice-till interactions and sediment entrainment beneath glaciers, *Journal of Geophysical Research: Earth Surface*, *113*(F1), F01,013, doi:10.1029/2007JF000870.

Remy, F., and B. Legresy (2004), Subglacial hydrological networks in Antarctica and their impact on ice flow, *Annals of Glaciology*, *39*(1), 67–72, doi:10.3189/172756404781814401.

Retzlaff, R., and C. Bentley (1993), Timing of stagnation of Ice Stream C, West Antarctica from short-pulse-radar studies of buried crevasses, *Journal of Glaciology*, *39*, 553–561.

Richardson, C., E. Aarholt, S.-E. Hamran, P. Holmlund, and E. Isaksson (1997), Spatial distribution of snow in western Dronning Maud Land, East Antarctica, mapped by a ground-based snow radar, *Journal of Geophysical Research: Solid Earth*, *102*(B9), 20,343–20,353, doi:10.1029/97JB01441.

Rignot, E., J. Mouginot, and B. Scheuchl (2011), Ice flow of the Antarctic Ice Sheet, *Science*, *333*(6048), 1427–1430, doi:10.1126/science.1208336.

Roberts, M. J. (2005), Jokulhlaups: A reassessment of floodwater flow through glaciers, *Reviews of Geophysics*, *43*(1), doi:10.1029/2003RG000147, rG1002.

Robin, G. D. Q., S. Evans, and J. T. Bailey (1969), Interpretation of radio echo sounding in polar ice sheets, *Philosophical Transactions of the Royal Society of London A: Mathematical, Physical and Engineering Sciences*, *265*(1166), 437–505, doi:10.1098/rsta.1969.0063.

Rothlisberger, H. (1972), Water pressure in intra- and subglacial channels, *Journal of Glaciology*, *11*(62), 177–203.

Rothlisberger, H., and H. Lang (1987), Glacial hydrology, in *Glacio-fluvial sediment transfer: an alpine perspective*, edited by A. M. Gurnell and M. J. Clark, pp. 207–284, John Wiley and Sons, New York.

Schoof, C. (2005), The effect of cavitation on glacier sliding, *Proceedings of the Royal Society of London A: Mathematical, Physical and Engineering Sciences*, *461*(2055), 609–627, doi:10.1098/rspa.2004.1350.

Schoof, C. (2010), Ice-sheet acceleration driven by melt supply variability, *Nature*, *468*(7325), 803–806, doi:10.1038/nature09618.

Schroeder, D. M., D. D. Blankenship, and D. A. Young (2013), Evidence for a water system transition beneath Thwaites Glacier, West Antarctica, *Proceedings of the National Academy of Sciences*, *110*(30), 12,225–12,228, doi:10.1073/pnas.1302828110.

Sergienko, O. V., and R. C. A. Hindmarsh (2013), Regular patterns in frictional resistance of ice-stream beds seen by surface data inversion, *Science*, *342*(6162), 1086–1089, doi:10.1126/science.1243903.

Sergienko, O. V., and C. L. Hulbe (2011), 'Sticky spots' and subglacial lakes under ice streams of the Siple Coast, Antarctica, *Annals of Glaciology*, *52*(58), 18–22, doi:10.3189/172756411797252176.

Sergienko, O. V., D. R. MacAyeal, and R. A. Bindschadler (2007), Causes of sudden, short-term changes in ice-stream surface elevation, *Geophysical Research Letters*, *34*(22), L22,503, doi:10.1029/2007GL031775.

Sergienko, O. V., T. T. Creyts, and R. C. A. Hindmarsh (2014), Similarity of organized patterns in driving and basal stresses of Antarctic and Greenland ice sheets over extensive areas of basal sliding, *Geophysical Research Letters*, *41*(11), 3925–3932, doi:10.1002/2014GL059976.

Shabtaie, S., I. M. Whillans, and C. R. Bentley (1987), The morphology of ice streams A, B, and C, West Antarctica, and their environs, *Journal of Geophysical Research: Solid Earth*, *92*(B9), 8865–8883, doi:10.1029/JB092iB09p08865.

Shapiro, N. M., and M. H. Ritzwoller (2004), Inferring surface heat flux distributions guided by a global seismic model: particular application to Antarctica, *Earth and Planetary Science Letters*, *223*(1-2), 213–224, doi:10.1016/j.epsl.2004.04.011.

Shreve, R. (1972), Movement of water in glaciers, *Journal of Glaciology*, *11*(62), 205–214.

Siegert, M., J. Dowdeswell, M. Gorman, and N. McIntyre (1996), An inventory of Antarctic sub-glacial lakes, *Antarctic Science*, *8*(3), 281–286, doi:10.1017/S0954102096000405.

Siegert, M., S. Carter, I. Tabacco, S. Popov, and D. Blankenship (2005), A revised inventory of Antarctic subglacial lakes, *Antarctic Science*, *17*(3), 453–460, doi:10.1017/S0954102005002889.

Siegert, M. J., N. Ross, H. Corr, B. Smith, T. Jordan, R. G. Bingham, F. Ferraccioli, D. M. Rippin, and A. Le Brocq (2014), Boundary conditions of an active West Antarctic subglacial lake: implications for storage of water beneath the ice sheet, *The Cryosphere*, *8*(1), 15–24, doi:10.5194/tc-8-15-2014.

Smith, B., H. Fricker, I. Joughin, and S. Tulaczyk (2009), An inventory of active subglacial lakes in Antarctica detected by ICESat (2003-2008), *Journal of Glaciology*, *55*(192), 573–595, doi:10.3189/002214309789470879.

Smith, L. C., V. W. Chu, K. Yang, C. J. Gleason, L. H. Pitcher, A. K. Rennermalm, C. J. Legleiter, A. E. Behar, B. T. Overstreet, S. E. Moustafa, M. Tedesco, R. R. Forster, A. L. LeWinter, D. C. Finnegan, Y. Sheng, and J. Balog (2015), Efficient meltwater drainage through supraglacial streams and rivers on the southwest Greenland ice sheet, *Proceedings of the National Academy of Sciences*, *112*(4), 1001–1006, doi:10.1073/pnas.1413024112.

Souchez, R., P. Jean-Baptiste, J. R. Petit, V. Y. Lipenkov, and J. Jouzel (2003), What is the deepest part of the Vostok ice core telling us?, *Earth-Science Reviews*, *60*(1-2), 131 – 146, doi:10.1016/S0012-8252(02)00090-9.

Stokes, C. R., C. D. Clark, O. B. Lian, and S. Tulaczyk (2007), Ice stream sticky spots: A review of their identification and influence beneath contemporary and palaeo-ice streams, *Earth-Science Reviews*, *81*(3-4), 217 – 249, doi:10.1016/j.earscirev.2007.01.002.

Studinger, M., R. E. Bell, G. D. Karner, A. A. Tikku, J. W. Holt, D. L. Morse, T. G. Richter, S. D. Kempf, M. E. Peters, D. D. Blankenship, R. E. Sweeney, and V. L. Rystrom (2003), Ice cover, landscape setting, and geological framework of Lake Vostok, East Antarctica, *Earth and Planetary Science Letters*, *205*(3-4), 195 – 210, doi:10.1016/S0012-821X(02)01041-5.

Tikku, A. A., R. E. Bell, M. Studinger, and G. K. Clarke (2004), Ice flow field over Lake Vostok, East Antarctica inferred by structure tracking, *Earth and Planetary Science Letters*, *227*(3-4), 249–261, doi:10.1016/j.epsl.2004.09.021.

Tulaczyk, S., W. B. Kamb, and H. F. Engelhardt (2000a), Basal mechanics of Ice Stream B, West Antarctica: 1. Till mechanics, *Journal of Geophysical Research: Solid Earth*, *105*(B1), 463–481, doi:10.1029/1999JB900329.

Tulaczyk, S., W. B. Kamb, and H. F. Engelhardt (2000b), Basal mechanics of Ice Stream B, West Antarctica: 2. Undrained plastic bed model, *Journal of Geophysical Research: Solid Earth*, *105*(B1), 483–494, doi:10.1029/1999JB900328.

Van de Berg, W., M. Van den Broeke, C. Reijmer, and E. Van Meijgaard (2005), Characteristics of the Antarctic surface mass balance, 1958-2002, using a regional atmospheric climate model, *Annals of Glaciology*, *41*(1), 97–104, doi:10.3189/172756405781813302.

Vaughan, D. G., H. F. J. Corr, C. S. M. Doake, and E. D. Waddington (1999), Distortion of isochronous layers in ice revealed by ground-penetrating radar, *Nature*, *398*(6725), 323–326, doi:10.1038/18653.

Waddington, E. (1987), Geothermal heat flux beneath ice sheets, in *The Physical Basis of Ice Sheet Modelling*, vol. 170, pp. 217–226, IAHS, Vancouver, Canada.

Waddington, E., J. Bolzan, and R. Alley (2001), Potential for stratigraphic folding near ice-sheet centers, *Journal of Glaciology*, *47*(159), 639–648, doi:10.3189/172756501781831756.

Waddington, E. D., T. A. Neumann, M. R. Koutnik, H.-P. Marshall, and D. L. Morse (2007), Inference of accumulation-rate patterns from deep layers in glaciers and ice sheets, *Journal of Glaciology*, *53*(183), 694–712, doi:10.3189/002214307784409351.

Walder, J. (1986), Hydraulics of subglacial cavities, *Journal of Glaciology*, *32*, 439–445.

Weertman, J. (1957), On the sliding of glaciers, *Journal of Glaciology*, *3*(21), 33–38.

Weertman, J. (1969), Water lubrication mechanism of glacier surges, *Canadian Journal of Earth Sciences*, *6*(4), 929–942, doi:10.1139/e69-097.

Weertman, J. (1976), Sliding-no sliding zone effect and age determination of ice cores, *Quaternary Research*, *6*(2), 203–207, doi:10.1016/0033-5894(76)90050-8.

Weertman, J., and G. Birchfield (1983a), Basal water film, basal water-pressure, and velocity of traveling waves on glaciers, *Journal of Glaciology*, *29*(101), 20–27.

Weertman, J., and G. Birchfield (1983b), Stability of sheet water-flow under a glacier, *Journal of Glaciology*, *29*(103), 374–382.

Wingham, D., M. Siegert, A. Shepherd, and A. Muir (2006), Rapid discharge connects Antarctic subglacial lakes, *Nature*, *440*(7087), 1033–1036, doi:10.1038/nature04660.

Winkelmann, R., M. A. Martin, M. Haseloff, T. Albrecht, E. Bueler, C. Khroulev, and A. Levermann (2011), The Potsdam Parallel Ice Sheet Model (PISM-PIK) - Part 1: Model description., *The Cryosphere*, *5*(3), 715–726, doi:10.5194/tc-5-715-2011.

Wolovick, M., and T. T. Creyts (2015), Overturned folds in ice sheets: Insights from a kinematic model of travelling sticky patches and comparisons with observations, *Journal of Geophysical Research: Earth Surface*, in review.

Wolovick, M. J., R. E. Bell, T. T. Creyts, and N. Frearson (2013), Identification and control of subglacial water networks under Dome A, Antarctica, *Journal of Geophysical Research: Earth Surface*, *118*(1), 140–154, doi:10.1029/2012JF002555.

Wolovick, M. J., T. T. Creyts, W. R. Buck, and R. E. Bell (2014), Traveling slippery patches produce thickness-scale folds in ice sheets, *Geophysical Research Letters*, *41*(24), 8895–8901, doi:10.1002/2014GL062248.

Wright, A., and M. Siegert (2012), A fourth inventory of Antarctic subglacial lakes, *Antarctic Science*, *24*(06), 659–664, doi:10.1017/S095410201200048X.

Wright, A. P., M. J. Siegert, A. M. Le Brocq, and D. B. Gore (2008), High sensitivity of subglacial hydrological pathways in Antarctica to small ice-sheet changes, *Geophysical Research Letters*, *35*(17), L17,504, doi:10.1029/2008GL034937.